Pacific Northwest
NATIONAL LABORATORY

PNNL-36795

Materials Characterization: A Primer for Solid Phase Processing Applications

September 2024

SW Glass
Y Guo
DR Todd
MS Good
KA Ross
TA White

U.S. DEPARTMENT OF ENERGY

Prepared for the U.S. Department of Energy
under Contract DE-AC05-76RL01830

DISCLAIMER

PACIFIC NORTHWEST NATIONAL LABORATORY
operated by
BATTELLE
for the
UNITED STATES DEPARTMENT OF ENERGY
under Contract DE-AC05-76RL01830

Printed in the United States of America

Available to DOE and DOE contractors from
the Office of Scientific and Technical Information,
P.O. Box 62, Oak Ridge, TN 37831-0062
www.osti.gov
ph: (865) 576-8401
fox: (865) 576-5728
email: reports@osti.gov

Available to the public from the National Technical Information Service
5301 Shawnee Rd., Alexandria, VA 22312
ph: (800) 553-NTIS (6847)
or (703) 605-6000
email: info@ntis.gov
Online ordering: http://www.ntis.gov

PNNL-36795

Materials Characterization: A Primer for Solid Phase Processing Applications

September 2024

SW Glass
Y Guo
DR Todd
MS Good
KA Ross
TA White

Prepared for
the U.S. Department of Energy
under Contract DE-AC05-76RL01830

Pacific Northwest National Laboratory
Richland, Washington 99354

Executive Summary

The Pacific Northwest National Laboratory (PNNL) undertook the Materials Characterization, Prediction, and Control (MCPC) Laboratory Directed Research and Development (LDRD) Project to advance understanding of nuclear material processing and enable multifold acceleration in the development and qualification of new material systems produced via advanced manufacturing methods, such as solid phase processing, for use in national security and advanced energy applications (Smith 2021).

As a two-year LDRD investment requiring focused research, the MCPC project applied only a subset of the wide range of available destructive and nondestructive characterization methods to provide data to the predictive modeling and data analytics tasks. *The purpose of this report is to review a wide range of destructive and nondestructive characterization methods that are relevant in solid-phase processing (SPP) applications, but not necessarily applied in the MCPC Project as a guide to the planning of characterization activities in future research.* Particular attention is given to measured characteristics that can correlate to other material characteristics, with a particular interest in nondestructive evaluation (NDE) that can be applied to samples obtained in the MCPC Project. Destructive examinations include tensile tests, optical and electron microscopy, micro-hardness, and residual stress tests. NDE tests include surface visual inspection, eddy current examination for cacks, 4-point potential drop, ultrasound, x-ray, and computed tomography. Conclusions include the following observations:

- Optical and electron microscope images of FSP materials show grain structure that can generally be correlated with mechanical strength.
- Ultrasound techniques can characterize grain size and be correlated to Young's modulus.
- The temperature of SSP is important for the material's quality. Temperature is commonly measured within FSP and ShAPE mandrils and spindles. Ultrasound is also identified as a candidate method to measure the instantaneous sample average temperature along the ultrasound path, which could include the region just behind the SSP.
- Ultrasound methods generally require fluid coupling between the sample and the transducer. Certain less common ultrasound methods, like the Electro Magnetic Acoustic Transducer and laser ultrasonic testing, can relate to traditional ultrasound measurements without the fluid coupling burden.
- Acoustic emission methods have been used to monitor samples subjected to substantially different spindles for aluminum FSP. The acoustic emission signals were successfully correlated with tensile strength, although it is noted that different spindles constitute a significant change to the FSP process.
- Electromagnetic methods (conductivity or eddy current) measure conductivity and can be sensitive to cracks or flaws in the material. Electromagnetic methods, however, are substantially restricted to the near surface (<1 mm).

Acknowledgments

This research was supported by the Materials Characterization, Prediction, and Control (MCPC) investment under the Laboratory Directed Research and Development (LDRD) Program at Pacific Northwest National Laboratory (PNNL). PNNL is a multi-program national laboratory operated for the Department of Energy (DOE) by Battelle Memorial Institute under Contract No. DE-AC05-76RL01830.

Acronyms and Abbreviations

AE	acoustic emission
AR	abrasion resistant
ASTM	American Society for Testing and Materials
CPP	cyclic potentiodynamic polarization
Cr	chromium
CT	computed tomography
DPC	differential phase contrast (of a radiograph)
EBSD	Electron Backscatter Diffraction
EMAT	electro magnetic acoustic transducer
FSP	friction stir processing
FSW	friction stir weld (a subset of FSP)
FSW/P	friction stir welding and processing
GTAW	gas tungsten arc welding
HAZ	heat affected zone
HV	hardness value
KB	kissing bond
LPI	liquid penetration induced
L-wave	longitudinal wave
MPa	megapascal or one million pascals
NDE	nondestructive evaluation
PNNL	Pacific Northwest National Laboratory
rpm	rotations per minute
SEM	Scanning Electron Microscopy
ShAPE	Shear Assisted Processing and Extrusion
SPP	solid-phase process
SS	stainless steel
S-wave	shear wave (also referred to as T-wave or transverse wave)
TEM	transmission electron microscopy
TMAZ	thermomechanically affected zone
T-wave	transverse wave (also referred to as S-wave or shear wave)
UT	ultrasonic testing

Contents

Executive Summary ii
Acknowledgments iii
Acronyms and Abbreviations iv
1.0 Introduction and Background 1.1
2.0 Friction Stir Welding and Processing 2.1
2.1 FSP Tooling and Process 2.2
2.1.1 Mechanical Properties 2.6
2.1.2 Tool Geometry, Rotation Speed, and Traverse Speed 2.7
2.1.3 Mechanical and Material Properties 2.8
2.1.4 Fatigue 2.9
2.1.5 Residual Stress 2.9
2.1.6 Hardness 2.10
2.1.7 Weld Microstructure 2.10
2.1.8 Types of Defects 2.10
2.1.9 Interrelationships of Material Properties 2.12
3.0 Shear Assisted Processing and Extrusion 3.1
4.0 Materials Characterization Tests Overview 4.1
5.0 Destructive Tests 5.1
5.1 Mechanical Tests 5.1
5.2 Micro Hardness 5.2
5.3 Correlation Between UT and Hardness 5.4
5.4 Optical Microscopy 5.7
5.5 Electron Microscopes 5.8
5.5.1 Scanning Electron Microscopy 5.8
5.5.2 Transmission Electron Microscopy 5.9
5.5.3 Electron Backscatter Diffraction 5.9
5.6 Sample Materials Study of Aluminum FSP Including SEM, TEM, and Hardness 5.10
6.0 Nondestructive Tests 6.1
6.1 Temperature Using Tool-Mounted Thermocouples 6.1
6.2 Temperature and Surface Profile Using Infrared and Optical Camera Following the FSP 6.2
6.3 Subsurface Temperature Using Ultrasonic Velocity and Attenuation 6.3
6.4 Grain Size Estimate by Ultrasonic Backscatter 6.4
6.5 Ultrasonic Temperature Dependence 6.8
6.6 Laser UT 6.9
6.7 Acoustic Emission 6.10

6.8 Resistivity/Conductivity: 4-pt Potential Drop 6.12
6.9 Electromagnetic / Eddy Current 6.14
6.10 X-ray Imaging and Computed Tomography 6.17
6.11 Additional Radiography and CT Material Signatures 6.20
7.0 Observations and Conclusion 7.1
8.0 References 8.1

Figures

Figure 2.1. FSP repair of laboratory-created chloride-induced stress corrosion cracking in 1-inch-thick SS 304L coupons 2.1
Figure 2.2. The FSP tool rotates counterclockwise as it traverses along the joint lines between the two plates 2.2
Figure 2.3. Cross section of FSP in 304/304L with zones labeled. The FSP tool is rotating counterclockwise; the traverse direction is outside the page. The advancing side (AS) of the joint is where a point on the outer edge of the tool is rotating from the back of the tool to the front. The retreating side (RS) of the joint is where a point on the outer edge of the tool is moving from the front to the back. The stir zone is where material is plasticized and mixed. The TMAZ is where material is mechanically deformed but not mixed. The HAZ is where the microstructure is affected by heat generated during welding, but no mechanical deformation exists. Image provided by (Ross and Alabi 2019). 2.3
Figure 2.4. Electron Backscatter Diffraction images show differences in microstructures seen in low-temperature FSP relative to arc welding 2.4
Figure 2.5. CPP coupons show low-temperature FSP's superior corrosion performance relative to GTAW. 2.6
Figure 2.6 ASTM E-8 (ASTM E8/E8M-16a 2016) tensile test coupon showing overmatched strength of FSP relative to the base metal 2.6
Figure 2.7. Tool rotation versus traverse welding speed shows heat generation. Reproduced with permission from Kim et al. (2006) 2.8
Figure 2.8. Material properties of a 304L SS sample acquired from tensile tests 2.12
Figure 3.1. One of several ShAPE units at PNNL used for SPP extrusion studies. 3.1
Figure 4.1. Non-exhaustive examples of materials characterization testing methods and sensors. 4.2
Figure 4.2. Nondestructive inspection testing methods are mapped based on depth of penetration (vertical axis) versus spatial resolution (horizontal axis). 4.3
Figure 4.3. Spatial resolution mapping of material defects and nondestructive inspection testing methods. 4.4
Figure 5.1. Example plot for mechanical tensile test 5.1
Figure 5.2. Schematic of a general micro-hardness diamond indenter tool and indentation. 5.2

Figure 5.3. (left) Design of the Vickers hardness test indentation head; (right) good, fair, and poor cold spray 5.3
Figure 5.4. Brinell Hardness versus Algorithm Predicted Hardness for a matrix of ARXXX type steel at six tempering temperatures 5.5
Figure 5.5. Hardness in interstitial free steel versus distance from weld center line 5.6
Figure 5.6. Rockwell hardness versus ultrasonic wave velocity variation for 0.092 percent (left) and 0.478 percent (right) carbon content in steel. Source (Uzun and Bilge 2017) 5.6
Figure 5.7. Example optical image of ferritic-pearlitic steel with approximately 0.2 percent C, etched with Nital 5.7
Figure 5.8. 2-D montage of over 300 micrographic images of an FSP..... 5.8
Figure 5.9. (left) SEM with both x-ray and secondary electron detectors receiving reflected energy from sample surface 5.9
Figure 5.10. EBSD configuration: a crystalline sample, oriented @ 70° with respect to normal beam incidence, produces a diffraction signal from backscattered electrons that can be collected on a phosphorous screen camera. 5.10
Figure 5.11. Cross-section of the optical overall micrograph in the FSP area, perpendicular to the tool traverse direction, the specimen produced at the tool rotation speed of 1100-rpm and a traverse velocity of 104 mm/min. 5.11
Figure 5.12. Vickers microhardness traverses through the section in Figure 5.11 along horizontal top, middle, and bottom dotted reference lines. 5.11
Figure 5.13. EBSD grain map of an FSP produced at 104 mm/min, 1100-rpm (left) transition zone on the retreating side (right) transition zone on the advancing side. 5.12
Figure 6.1. TTC corner thermocouple response changes cyclically as a faction of spindle rotation. 6.1
Figure 6.2. Thermocouple locations on an FSP tool for 20-mm thick aluminum. 6.2
Figure 6.3. (left) Camera positioning following directly behind the FSP 6.3
Figure 6.4. (a) uneven weld edge (b) excessive edge burr (c) cracks from overheating. 6.3
Figure 6.5. Concept of using ultrasonic wave velocity to estimate the subsurface temperature of a material volume undergoing solid-phase processing. 6.4
Figure 6.6. Dependence of material properties on grain size for high manganese austenitic steel specimens 6.5
Figure 6.7. Anisotropy factor for cubic metals and alloys 6.6
Figure 6.8. Wave velocity surfaces for a single grain of SS 6.6
Figure 6.9. Typical amplitude versus time responses of backscatter in a pulse-echo configuration for shear waves and longitudinal waves 6.7
Figure 6.10. Comparison between grain-size determination by ultrasonics and by metallography 6.7
Figure 6.11. Ultrasonic noise amplitude versus micrograph-measured mean grain size. 6.8
Figure 6.12. PNNL study to estimate the internal temperature of Al 6.9
Figure 6.13. Setup for laser waveform generation and detection. 6.10

Figure 6.14. Test setup for AE monitoring of FSP. 6.11
Figure 6.15. Relationship between AE parameters with tensile strength of FSP specimens produced by different tool pin profiles 6.12
Figure 6.16. Decrease of electric conductivity of the AA1100 with temperature. 6.13
Figure 6.17. (left) 2-point and 4-point potential drop measurements are based on a correction factor related to S2 and t 6.14
Figure 6.18. Eddy current coil sensors induce currents within conductive materials, and the coil impedance changes as a result of those eddy current behaviors can be sensed to indicate anomalies within the test material. 6.15
Figure 6.19. There are a large number of possible coil configurations for eddy current testing 6.16
Figure 6.20. EddyFi representation of concavities and notches in FSP. 6.16
Figure 6.21. A graphic of an x-ray imaging system showing the principal components: the x-ray source on the left, imaging detector on the far right, and the object under interrogation between the source and detector 6.18
Figure 6.22. Tomography and destructive evaluation across length scales 6.19
Figure 6.23. Three orthogonal cross sections from a CT scan of three aluminum plates 6.20
Figure 6.24. Orthogonal slices form a 3-D CT reconstruction of phase-contrast data of an FSP of a cast-aluminum block (AlSi7Mg0,3 alloy)..... 6.21
Figure 6.25. Spectral-imaging example: The attenuation coefficient of uranium has a discontinuity at the k edge just below 120 keV. An imaging system with a spectral capability and a tunable x-ray source can be used to identify material composition, in this case to map the spatial distribution of uranium and oxygen in a radiograph. 6.22

Tables

Table 5.1. Overview of Vickers hardness test applicability, advantages, and limitations. 5.3
Table 6.1. Overview of eddy current technology applicability, advantages, and limitations. 6.17

1.0 Introduction and Background

The Pacific Northwest National Laboratory (PNNL) undertook the Materials Characterization, Prediction, and Control (MCPC) Laboratory Directed Research and Development Project to advance understanding of nuclear material processing and enable multifold acceleration in the development and qualification of new material systems in national security and advanced energy applications (Smith 2021). The MCPC Project executed research across three scientific vertices—material characterization, predictive modeling, and data analytics.

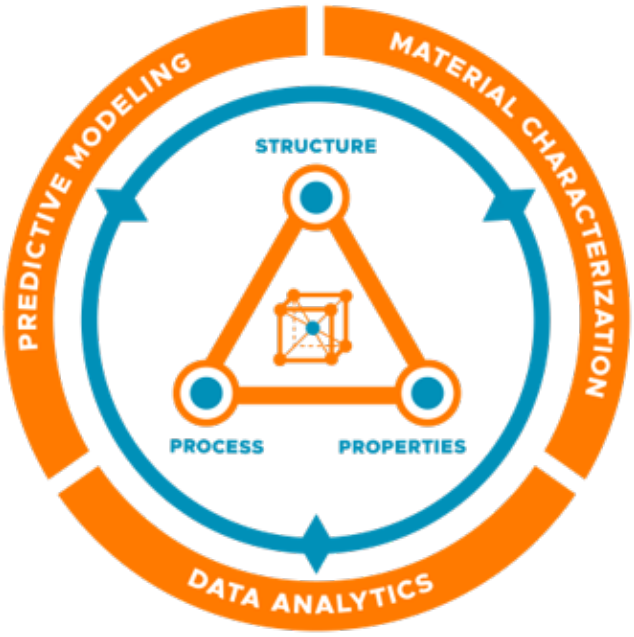

MCPC Project Logo

The central technical objective in the MCPC Project was to improve the prediction and characterization of the process-structure-property relationships within the microstructurally refined region of stainless steel (SS) samples prepared utilizing two solid phase processing (SPP) techniques. The two techniques, known as friction stir processing (FSP) and Shear Assisted Processing and Extrusion (ShAPE^{TM}), are well-established at PNNL within the Solid Phase Processing capability through many years of investment across a range of materials and applications (PNNL 2024).

As a two-year Laboratory Directed Research and Development investment requiring focused research, the MCPC project applied only a subset of the wide range of available destructive and nondestructive characterization methods to provide data to the predictive modeling and data analytics vertices. The purpose of this report is to review a wide range of destructive and nondestructive characterization methods that are relevant in SPP applications but not necessarily applied in the MCPC Project as a guide to the planning of characterization activities in future research.

Additional Background

Typically, verification of microstructure and performance-related properties is accomplished through statistical sampling and destructive laboratory analyses. Aside from being time-consuming, expensive, and requiring an on-site analytical laboratory, the sampling-based approach is also slow to reveal a problem in the process and can lead to significant material waste.

Nondestructive evaluation (NDE) techniques can reduce the need for product sampling and analysis, thereby shortening the experiment-to-measurement-to-analysis cycle from several weeks to real (or near-real) time. In-line NDE techniques that measure properties of interest either directly or indirectly enable real-time analysis. The signatures collected from indirect NDE methods can be correlated to the specific properties of interest (e.g., yield/ultimate strength, percent elongation at break, porosity or void fraction, hardness, grain size, texture, electrical or

thermal conductivity, residual stress, sound velocity, etc.) using benchmarking measurements from destructive analysis. For example, inline acoustic signals are a function of the material's microstructure and can be correlated with images of grain size and texture from electron microscopy methods.

Utilizing a variety of off-line measurements, including both destructive and nondestructive approaches, a motivation of the MCPC Project was to develop improved inline monitoring or immediately post-fabrication techniques that can support real-time or near-real-time characterization of material microstructure (grain size, yield, ultimate, and percent elongation tensile strength, hardness, conductivity, etc.), fabrication defects (cracks, porosity, voids, kissing bonds (KBs), etc.), and residual stress. Recognizing these material characteristics and states in real-time or near real-time may allow improved closed-loop control of SPP production parameters (force, speed, temperature, etc.) to produce higher-quality materials and particularly to identify poorer-quality materials before they progress on to become finished and installed parts in safety-critical systems.

2.0 Friction Stir Welding and Processing

Friction stir welding and processing (FSW/P) are solid-phase joining processes that are achieved by spinning a tool and plunging it into the workpiece. Frictional heating and material deformation enable the formation of a plasticized region below the tool shoulder called the stir zone. If the FSP tool and stir zone are traversed across a joint, effectuating a weld, then the joint is referred to as an FSW[1] and can be considered a subset of the FSP class of processes. If the tool is plunged into a single solid piece, the stir zone can change material properties but are not really forming a weld and therefore are referred to as an FSP. Temperatures generated during FSP are typically between 60 percent and 80 percent of the absolute melting temperature of the workpiece material. The use of FSP to repair chloride-induced stress corrosion cracks is shown in Figure 2.1, where the tool is passed over the crack to re-fuse the material, thereby eliminating the crack (Ross, Sutton, et al. 2017b).

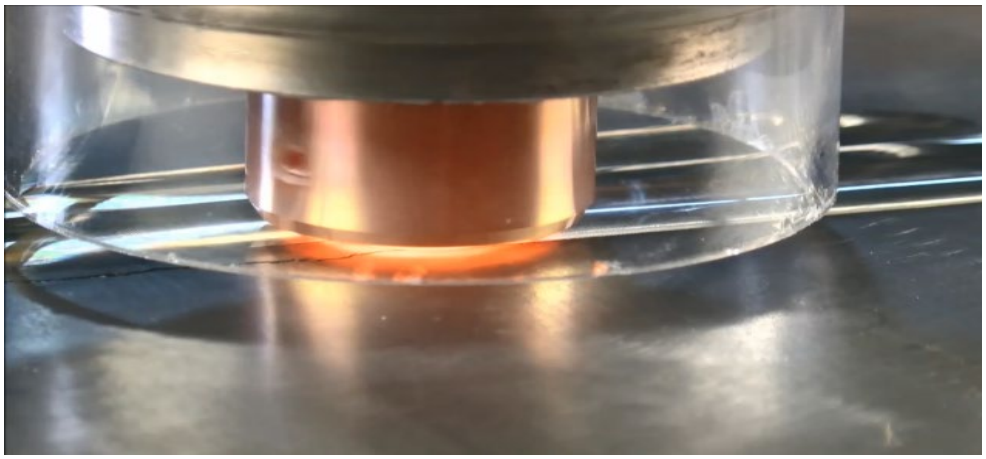

Figure 2.1. FSP repair of laboratory-created chloride-induced stress corrosion cracking in 1-inch-thick SS 304L coupons. FSP was performed at PNNL (Ross, Sutton, et al. 2017a).

Advantages

- Temperature-controlled FSP ensures heat input is sufficiently low to avoid or reduce corrosion susceptibility in and near the weld.
- The general corrosion resistance of the processed region is superior to that of arc welding, and there is no detrimental heat affected zone (HAZ).
- For austenitic SSs, mechanical properties are overmatched: tensile specimens fail in the base metal rather than the stir-processed zone.
- FSP fully repairs physical defects (cracks, pitting) and microstructural damage (sensitization).
- FSP is a green process (no harmful fumes generated, low energy consumption).
- Welding or repairs can be done in a single pass.
- FSP is fully automated.
- FSP provides a relatively smooth surface after joining.
- Dramatically reduced defect generation rate compared to arc welding.

[1] Reference to FSP and FSW is generally synonymous in this report.

Technical Challenges

For FSP of austenitic SSs, tool life is the primary technical challenge for volume production.

2.1 FSP Tooling and Process

The primary control axes for FSP are spindle, forge, and traverse (Figure 2.2). The spindle axis is the rotation of the FSP tool. Traditionally, the control variable for the spindle axis has been the rotation rate, defined by rotations per minute (rpm). PNNL controls the spindle axis by modulating the mechanical power input from the spindle into the weld to maintain a constant temperature as measured in the FSP tool. For this work, tool temperature is the control variable for the spindle axis. Power, rpm, and torque are output variables for the spindle axis.

The forge axis is movement in the tool's rotation axis direction. In Figure 2.2, the forge axis is shown in blue, and the tool axis is shown as a yellow line. The forge axis controls the movement and applied force of the FSP tool into the workpiece in the tool's axial direction. The forge axis typically runs under either force control or position control mode. When the forge axis is run in force control mode, a desired forge force is maintained, and position in the tool's axial direction (depth) is a process output. When the forge axis is run in position control mode, the position of the tool is maintained, and tool axial force, or forge force, is a process output. The traverse axis is defined as the axis that is in the weld direction. The cross seam, or transverse axis, is the axis perpendicular to the weld direction.

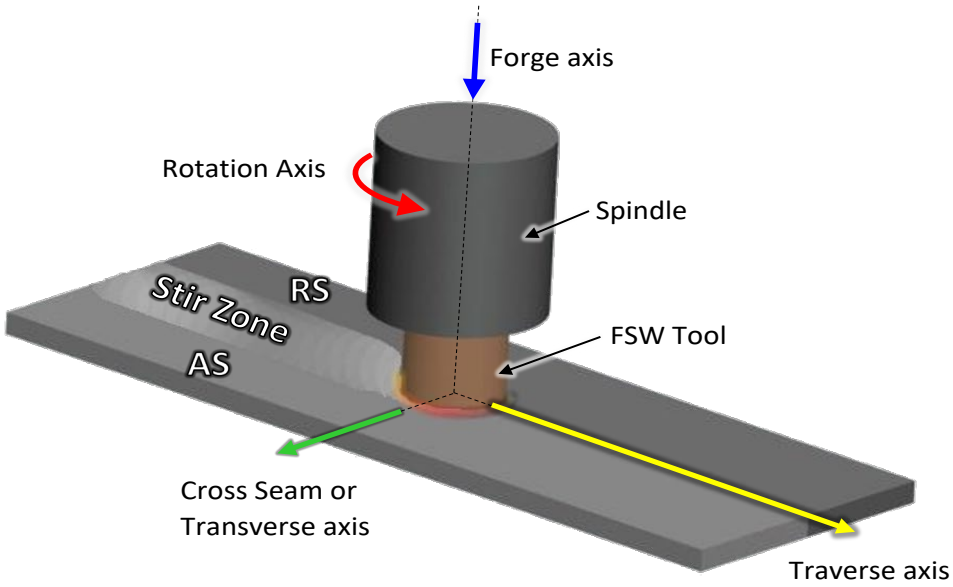

Figure 2.2. The FSP tool rotates counterclockwise as it traverses along the joint lines between the two plates. Plasticized material is mixed, forming a welded joint behind the tool. The stir zone is the material that has been mixed. The advancing side is the side of the joint where a point on the outer edge of the tool is rotating from the back of the tool to the front. The retreating side of the joint is where a point on the outer edge of the tool is moving from the front to the back. Image provided by (Ross and Alabi 2019).

A cross section of a FSP in SS 304/304L is shown in Figure 2.3, and weld zones are labeled and defined. The weld zones include the stir zone, the thermomechanically affected zone

(TMAZ), and the HAZ. The stir zone is where material is mixed or stirred, producing a highly refined grain structure. The TMAZ is where material is mechanically deformed and affected by weld heat input, but the material is not mixed. The HAZ is where the microstructure is affected by heat generated during welding, but no mechanical deformation exists.

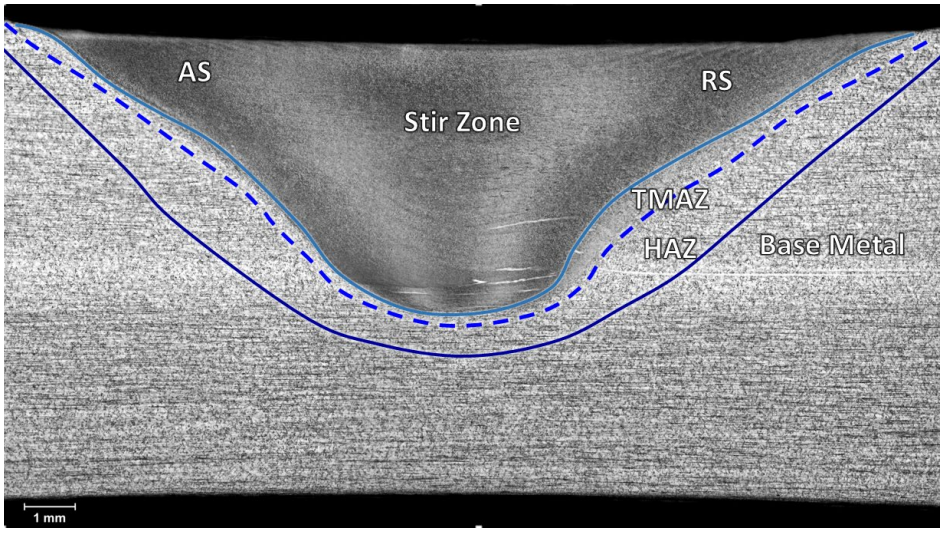

Figure 2.3. Cross section of FSP in 304/304L with zones labeled. The FSP tool is rotating counterclockwise; the traverse direction is outside the page. The advancing side (AS) of the joint is where a point on the outer edge of the tool is rotating from the back of the tool to the front. The retreating side (RS) of the joint is where a point on the outer edge of the tool is moving from the front to the back. The stir zone is where material is plasticized and mixed. The TMAZ is where material is mechanically deformed but not mixed. The HAZ is where the microstructure is affected by heat generated during welding, but no mechanical deformation exists. Image provided by (Ross and Alabi 2019).

It is important to note that low-temperature FSP can produce welds that appear to have no detrimental HAZ in austenitic SS. Electron Backscatter Diffraction (EBSD) images shown in Figure 2.4 compare the cross section of low-temperature FSP to an arc weld. There is no apparent grain growth in the HAZ in FSP. The stir zone shows an ultrafine grain microstructure.

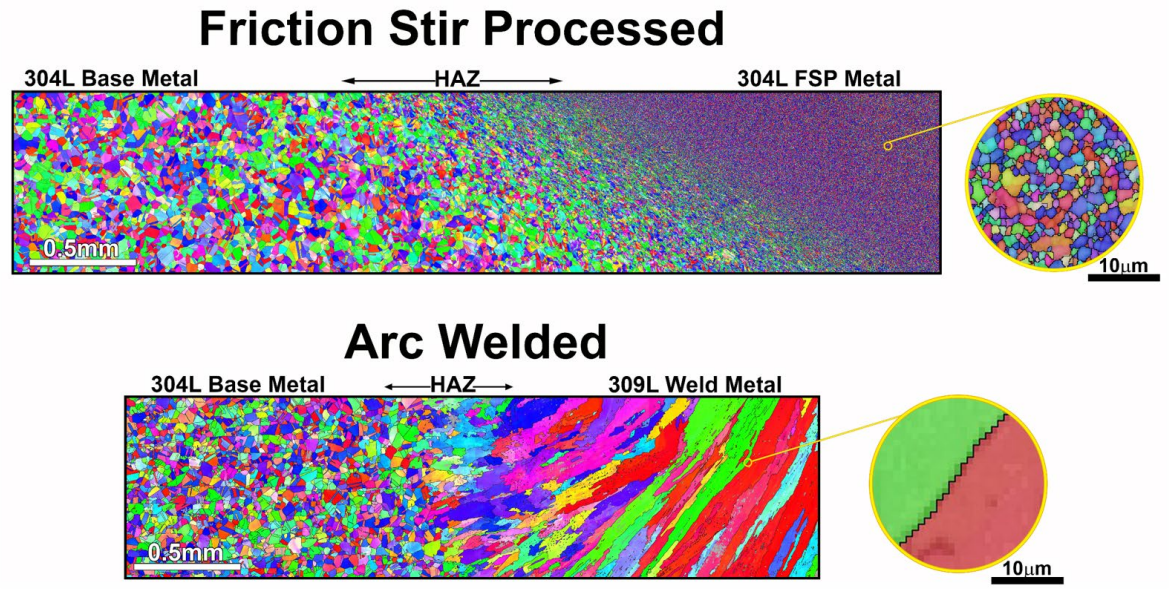

Figure 2.4. Electron Backscatter Diffraction images show differences in microstructures seen in low-temperature FSP relative to arc welding (Ross and Alabi 2019).

The ability to assess weld quality as a function of the welding process signature in real-time could significantly reduce the risk of rework. FSP technology and equipment lend themselves well to assessing weld quality in real-time. Such a “screening” tool would obviate the need for conventional information-only NDE and, due to the real-time nature of the process, would be more efficient in identifying when to stop the welding process to make in-process repairs. Previous work at PNNL has developed and demonstrated (Ross, Grant, et al. 2017) control technology to maintain constant temperature conditions throughout welds and from weld to weld. The combination of advanced controls and screening tools will enable detection of pre-defects and modification of process parameters to avoid defect formation. When applied in this manner, it will be extremely rare for defects to occur, and when defects do occur, they will be immediately detected.

FSP has can be performed more quickly and likely at lower cost than arc welding because thick sections can be done in a single pass.. Low-temperature FSP also produces superior mechanical properties and corrosion resistance relative to thermal joining techniques.

Recent developments in tool materials and process controls have improved tool life for FSPs of austenitic SS. Within the last decade, composite tools like Megastir Q70, which contain 70 percent polycrystalline boron nitride and approximately 30 percent tungsten-rhenium, were developed that have good tool life and can achieve FSP weld depths of greater than 1/2-inch thick.

Weld properties (Long, Tang, and Reynolds 2007; Richards et al. 2010; Sato, Urata, and Kokawa 2002), such as fracture toughness and corrosion resistance, vary with weld temperature. Traditional control methods for FSP result in large variations in temperature over the length of the weld and correspondingly produce inconsistent properties. If specified properties are desired throughout the weld, the weld temperature must be controlled.

The traditional control parameters for FSP are spindle speed, travel speed, and tool force/depth. These parameters are typically held constant after the initial plunge and traverse. The temperature is not constant at constant spindle speed. FSP of a flat plate in a laboratory environment showed a temperature change of 20°C in a 254 mm section, and similar temperature variances were seen throughout the weld (Ross and Sorensen 2013). This weld was run in a controlled lab environment. Full pipe welds run at constant spindle speed in a lab environment and show a temperature variation of more than 60°C (Mahoney et al. 2016). It is assumed that the temperature variation in the field is higher. These traditional controls for FSP have no means to actively reject thermal disturbances. Variation in the following causes thermal disturbances: ambient temperature, thickness within a part, thickness from part to part, material properties or chemistry, clamping, thermal mass of material surrounding the FSP tool, thermal contact resistance at the part-backing plate, and backing plate-anvil interfaces.

Because of the high cost of FSP research tools for steels, many researchers run welds too hot in fear of breaking tools. Until recently, many FSP researchers did not consider or even record weld temperatures. Because researchers did not monitor or control weld temperature, there are disagreements in reported values for weld properties for a given material. Furthermore, the majority of reported properties for FSP of high-temperature alloys are lower than optimized values because they are run too hot.

PNNL has developed robust temperature control technology for FSP that allows measured temperatures to be held within 1°C despite the presence of process disturbances. This allows for weld properties to be repeatable within a weld and from weld to weld. Robust temperature control allows for stable welds at very low temperatures, producing improved performance.

General and localized corrosion behavior can strongly influence the propensity for stress corrosion cracking to occur in dry cask storage systems (for spent nuclear fuel) canister weldments. Previous work (Cannell, Grant, and Adams 2015) shows that low-temperature FSP performs significantly better compared to gas tungsten arc welding (GTAW), which is the current process used in fabrication welds of dry cask storage spent nuclear fuel canisters, including localized corrosion. Corrosion evaluation consisted of electrochemical measurements, including: (1) open circuit potential monitoring, (2) linear polarization resistance scans, and (3) cyclic potentiodynamic polarization (CPP) scans. Corrosion rates for low heat input welds where the measured temperature was below 780°C, as reported in (Cannell, Grant, and Adams 2015), were below 1 mil per year, and some were lower than 0.05 mil per year. FSP with high heat input and GTAW coupons varied between 32 and 48 mil per year. The dramatic improvement in corrosion resistance of the low-temperature FSPs can be seen optically in the CPP coupons shown in Figure 2.5.

This work showed that when the temperature is kept sufficiently low during FSP, the corrosion rate of the weld and surrounding material can be less than 1/640 that of GTAW. Studies presenting mechanisms for improved corrosion resistance of low-temperature FSP of austenitic SS were not found in the literature. The mechanisms for these improvements are likely reduced heat input and grain refinement. Reduced heat input reduces the risk of sensitization and other forms of microstructural degradation.

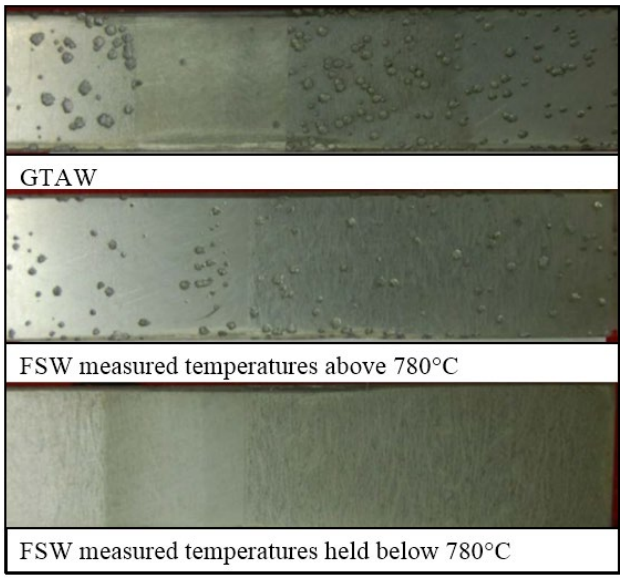

Figure 2.5. CPP coupons show low-temperature FSP's superior corrosion performance relative to GTAW.

Low-temperature FSP produces ultrafine-grained material. A literature review (Gupta and Birbilis 2015) reported that the passive film developed on nanostructured SS is more stable, more compact, contains lower defect density, and has a higher chromium (Cr) content (for an equivalent bulk Cr content) compared to passive films formed over coarse-grained SS. This literature review included 266 references. In this wide study of the literature, the broad consensus was that nanocrystalline structures improve corrosion resistance. A recent study (Tiamiyu et al. 2019) evaluated the corrosion resistance of coarse-, fine-, and ultrafine-grained SS. This study showed that corrosion resistance improves with decreasing grain size and that ultrafine-grained material had a more stable passivation film similar to that reported in nanostructured SS.

2.1.1 Mechanical Properties

Low-temperature FSP produced improved mechanical properties relative to the base metal for austenitic SS. This is shown in Figure 2.6, where failure occurs in the base metal, far away from the weld and HAZ.

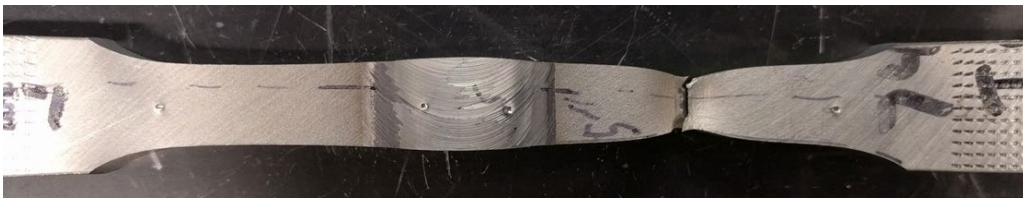

Figure 2.6 ASTM E-8 (ASTM E8/E8M-16a 2016) tensile test coupon showing overmatched strength of FSP relative to the base metal.

Since FSP is typically implemented in an automated process, when using correctly designed tools and parameters, defects should not occur. However, if the process is incorrectly controlled, the resulting quality of the weld can be degraded. For any material joining technique, no process is perfect, and defects can potentially occur. For FSP, wormholes, KBs, and defects caused by

a lack of penetration are the typical defects of current concern in industry (Podržaj, Jerman, and Klobčar 2015), (Kah et al. 2015). These defects are typically quite different from those found in a conventional thermal fusion weld process.

A further constraint is that the FSP method is typically a high-end fabrication method. In most cases, destructive evaluation of such welds is not recommended for evaluating quality since it is costly in terms of lost items and time-consuming to conduct (Sagar et al. 2012). When used, destructive examination techniques generally involve bending tests and metallography/macrographs. In these techniques, the welded samples are removed from the original welding surface, but such samples only provide data for the region where measurements, such as micrographs, are taken. In general, evaluation of weld quality is most commonly performed post-weld using conventional nondestructive testing methods, such as x-rays, ultrasonic testing (UT), eddy current, and dye penetrant, although the latter are limited to detecting surface defects.

2.1.2 Tool Geometry, Rotation Speed, and Traverse Speed

FSP behavior in SS and various aluminum (Al) alloys differs, and one should not directly relate observations from one material to another, but the number of studies in aluminum has produced a significant wealth of knowledge that should not be ignored. As described by Threadgill et al. (2009), for a given aluminum alloy and plate thickness with a particular tool, the primary operating process variables that affect the heat generation phenomena are the pin geometry and then the downward force, tool plunge depth, rotation speed, and traverse speed. The downward force is a preset variable (if welding is not accomplished under position control), while the tool plunge depth needed is defined by sample thickness. This leaves rotation speed and traverse speed as undefined process variables. Increased rotation speed leads to higher levels of heating and, hence, higher temperatures in the material (Figure 2.7). Kim et al. (2006) performed a test in which the tool rotation speed was varied and the resulting temperature of the weld in a 6061-T6 aluminum plate was measured for various speeds; all other parameters were kept constant. At a tool rotation speed of 300 rpm, a temperature of 425°C was recorded. An increase to 650 rpm resulted in a 40°C increase to 465°C, and a further increase in speed to 1000 rpm resulted in a further increase of 20°C to 485°C. Variations in the second key parameter, transverse speed, are found to directly impact weld quality. There is an optimal set of speed conditions, with degraded welds occurring when the speed is either too slow or too fast. When the transverse speed is too fast, defects are common because the pin moves too fast to give the time needed to properly mix the material and generate the needed level of heat input. A slow traverse speed will create too much heat within the weld and lead to different forms of defects such as flash, voids, or nugget collapse.

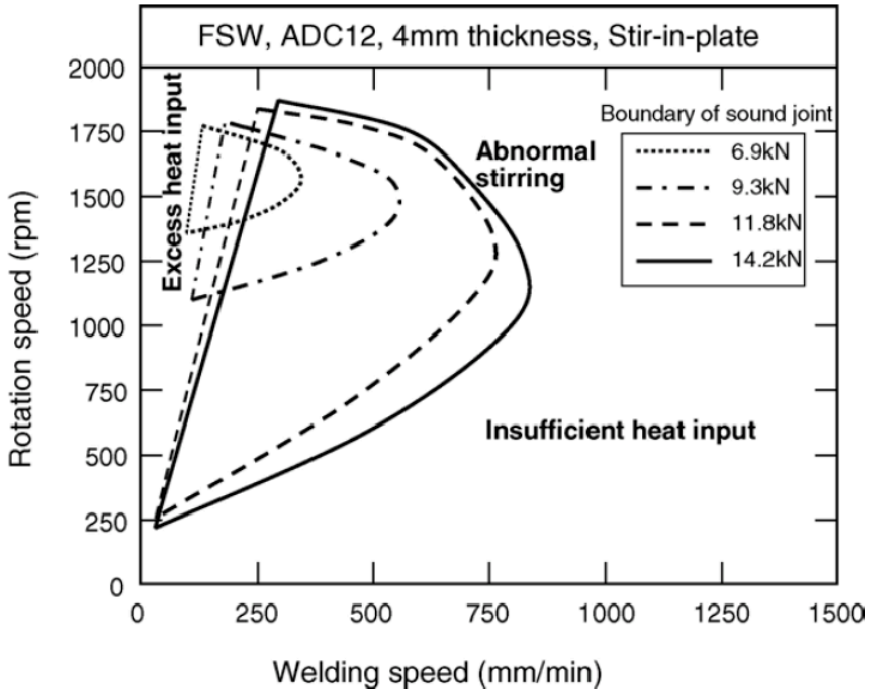

Figure 2.7. Tool rotation versus traverse welding speed shows heat generation. Reproduced with permission from Kim et al. (2006).

2.1.3 Mechanical and Material Properties

There are a large number of studies that evaluate and relate mechanical and material properties in FSP welds. These have included using experimental, modeling, and optimization methods (Elatharasan and Kumar Senthil 2012). Many studies have been performed testing the ductility, tensile strength, yield, and ultimate strength of material in FSP welds, and the results are found to vary based on the FSP parameters, post-weld heat treatments, and the materials involved. Mahoney et al. (1998) tested the mechanical properties of 7075-T651 aluminum using tensile specimens prepared in both transverse (across weld) and longitudinal (along weld nugget) orientations. The longitudinal orientation samples retained 85 percent tensile strength, 65 percent yield strength, and an equivalent elongation when compared to the base material. A post-weld aging treatment was reported to further decrease elongation and tensile strength, but it restored yield strength. The transverse orientation samples maintained 75 percent tensile strength and 55 percent yield strength, but only half the elongation. It is expected for the transverse orientation to have lower values for mechanical properties as it encompasses material from all the weld zones. These results have been verified in other studies, and they are consistent with other reports that FSP materials typically maintain 80 percent tensile strength and approximately 60 percent yield strength when compared to the base metal properties. However, these data do not take into account the effects of various potential cooling processes, different process parameters, and the use of different combinations of materials (Kahl and Osikowicz 2013). When performing destructive tests and breaking the weld apart for the weld areas as defined above, the strength metrics were almost constant in the weld nugget; the yield strength was approximately 80 percent of the value for base materials, and the ultimate strength was close to 100 percent with an addition of improved ductility. These properties are directly related to the grain size and structure of the weld nugget material. When moving into TMAZ, the structure retains strength but loses ductility. Finally, the HAZ, as commonly found for many processes, is the weakest zone for the weld. In HAZ material, the tensile strength can vary

significantly, with resulting values as low as approximately 60 percent of the base material, and consistently low ductility has also been reported (Kadlec, Růžek, and Nováková 2015). It has further been reported that the strength and ductility for the advancing and retreating sides of the weld are different, with the retreating side exhibiting lower strength (Mishra and Ma 2005), and this is consistent with fractures always being found to occur on the retreating side in transverse cut samples.

2.1.4 Fatigue

With the increasing use of FSP in industries where fatigue life is of high importance, there has been research to investigate fatigue properties and factors affecting fatigue life. FSP has been used to arrest fatigue cracks; however, most of the literature shows FSP to have lower fatigue strength than base material but higher than thermal joining techniques. Thus, the weld may be susceptible to being the site for fatigue crack initiation (Sillapasa et al. 2017) (Sillapasa et al. 2014). FSP butt welds have a higher fatigue performance that generally exceeds that of comparable fusion welds for many alloy grades, and this is due to the refined microstructure characteristics that are found in FSP material. In another study, removal of 0.5–1 mm from the top and bottom of FSP welds resulted in strength increases and improved fatigue life (Bussu and Irving 2003b). It is noted that other factors also affect sample fatigue life, especially any residual stress, the microstructure, and the presence of defects that must also be accounted for when making fatigue life comparisons.

Moreira et al. (2008) found in aluminum alloys that friction stir material generally exhibited lower strength and ductility properties than the base material. However, enhanced crack propagation resistance is observed in the welded material. The 6082-T6 and 6061-T6 base materials exhibit similar crack propagation behaviors.

Similarly, Costa, Ferreira, and Borrego (2011) found FSP specimens to present higher fatigue resistance than specimens welded by metal inert gas and tungsten inert gas processes. However, they still have lower fatigue lives than base metal.

In (Toumpis et al. 2016), typical fatigue performance of friction stir-welded DH36 steel plates has been established, exhibiting considerably extended fatigue lives, well above 105 cycles at a stress range of 90 percent of yield strength, irrespective of minor instances of small surface-breaking flaws that were identified. It was also noted that FSP samples exhibit better fatigue performance than submerged arc welded samples of equivalent thickness and that tensile samples broke away from the weld zone, indicating the FSP's strength was greater than the base metal.

2.1.5 Residual Stress

Residual stresses are self-equilibrating forces in materials that occur even in the absence of external loads. Residual stresses can have either detrimental or beneficial effects on the structural integrity and performance of the parts, depending on the location and exact nature of the stresses. Since the magnitude of residual stresses can be as high as the yield strength of the materials, the evaluation of residual stresses found in FSP joints is crucial (Lemmen et al. 2010). One beneficial effect is inducing compressive stress at a surface to increase the service life of a metal component, as performed by laser shock peening for cold-pilger steel die (Lavender et al. 2008).

2.1.6 Hardness

The mechanical properties of joints can be evaluated by measuring their hardness distribution. In the case of FSP joints, measurements of the Vickers hardness are an appropriate method since values can vary significantly over the region investigated (Suenger et al. 2014). It has been shown that dissolution and growth of the precipitates during the thermal process of FSP can affect the hardness and, consequently, joint efficiency (Khodir, Shibayanagi, and Naka 2006). Most of the hardness evaluations have involved first monitoring temperature during FSP and then evaluating subsequent data in terms of its relationship to the microstructure and hardness distributions. At higher temperatures (573 K in the case of AA2024-T3), precipitates started to dissolve, and consequently, the HAZ lost its hardness, resulting in a reduction in joint efficiency. Precipitate growth time can be decreased by increasing the heating rate, which then causes hardening in the HAZ.

2.1.7 Weld Microstructure

The degree of heat generation that occurs during the joining process greatly alters the resulting microstructure. Four separate areas are identified when the material is examined, and these are defined by the American Welding Society as:

1. Base metal or unaffected metal: parent metal in which the microstructure and mechanical properties are the same as before the welding process.
2. HAZ: volume close enough to the weld for thermal effects to modify the microstructure and/or mechanical properties but with no plastic deformation.
3. TMAZ: this zone is identical to the HAZ but has plastic deformation. Recrystallization does occur in general, but not for aluminum alloys.
4. Stir zone: the area along the weld nugget in which the process passes through, recrystallization occurs for all materials in this zone (Podržaj, Jerman, and Klobčar 2015).

The weld nugget material is typically recrystallized, and it has a fine and equiaxed grain microstructure. Notably, in aluminum materials subject to FSP, crystallization occurs within the weld nugget, and it is usual to finish with equiaxed grain sizes on the order of a few micrometers. It is also possible to control grain size by using external cooling or altering various process parameters. In metallographic examinations, it is common to see larger grains at the top of the weld due to the effects of heat dissipation through the backing plate and as a result of the lower peak temperatures at the bottom of the weld (Mishra and Ma 2005) (Ghorbanzade et al. 2014).

2.1.8 Types of Defects

With adequate process control, the FSP is often capable of effectively eliminating, or at least significantly reducing, the occurrence of many of the defects associated with fusion welding techniques, such as shrinkage, solidification cracking, and porosity. However, as in any weld, some defects can occur that are dependent on the joint geometry (butt or lap), but each type of defect does not affect the material in the same way and therefore must be understood if it is to be identified and then prevented by process modifications (Wulff 2013). There are still various types of defects that can occur during the FSP, irrespective of the welding orientation.

Wormhole

Wormhole defects are in the form of voids or trailing voids left in the material after the welding process. Such defects are caused by abnormal material flow conditions during welding resulting from suboptimal combinations of numerous factors, including stirring rotational speed, traverse speed, resulting heat generation, and shoulder pressure. This type of defect can be prevented by using pins with a design optimized to match the weld material and thickness or by adjusting the welding process parameters. Kahl and Osikowicz (2013) evaluated the occurrence of wormhole voids along the weld nugget in 6061-T6 aluminum and observed a decrease of 10 percent in tensile strength and a large reduction in elongation when wormholes occur. For the same material fatigue testing between 42.5 and 57.5 MPa stress amplitudes, the samples exhibited a decrease of approximately 20 percent in lifetime for those welds that contained small voids.

Lack of Penetration

Lack of penetration defects are found in butt welds, where the lower portion of the joined interface is only partially disrupted. This is caused by the FSP pin not being long enough to penetrate both materials effectively, and it can be prevented by using a pin design that is optimized for the specific weld application and by keeping the shoulder of the tool flush with the material surface (Mandache et al. 2012).

Kissing Bonds

Partial bonds or Kissing Bonds (KBs) typically occur at the root of the weld. This type of defect arises when two adjacent surfaces are in close contact but never form a full metallurgical bond (Oosterkamp, Oosterkamp, and Nordeide 2004), giving reduced strength. The KB can have surfaces in contact and no metallurgical joining. This is due to insufficient deformation of the joining surface interface due to incorrect tool design, lack of penetration, poor surface preparation, residual stress, contamination, or some combinations of these factors (Delrue et al. 2016). The effect of KB on the static strength of the weld can be negligible and depends on the application. However, KB defects can significantly reduce fatigue life depending on the size of the KB defect area (Ruzek and Kadlec 2014). For example, Kadlec, Růžek, and Nováková (2015) performed mechanical testing to investigate the effects of the KB defects on the tensile and fatigue properties of 7475-T7351 friction stir welds against welds without any flaws. Various KB defects were investigated by Kadlec with the aim of evaluating which defect geometry has no influence on the fatigue life of joined 6.35 mm-thick plates. A critical value for KB geometry seemed to be 0.3 mm in depth, considering its influence on fatigue life for the investigated configurations. It was reported that samples with shorter KBs had higher elongation values and higher tensile strengths. It was also reported that when a KB ‘opens up’, it causes a fracture before necking can start. This study showed the detrimental effects of having KBs in welds in structural materials. When using conventional nondestructive testing techniques, the detection and determination of an accurate size for the KB defect is a difficult task.

Cracks

There are various factors that can cause cracks in the processed zone of FSP. Among the causes of cracking are excessive local load and stress concentrations that can generate cracks in the processed area due to high thermal stresses (Bussu and Irving 2003a). Resulting residual stresses and HAZ properties can also influence crack formation and propagation in FSP joints. Furthermore, the development of the microstructures that occur in the weldment during the FSP

process affects crack growth due to both corrosion and fatigue (Pao et al. 2001). Another mechanism involved with crack generation in FSP is liquid penetration induced (LPI) cracking. The LPI cracking mechanism has been studied for a variety of alloys and situations. For example, Yamamoto et al. (2007) explained that LPI cracking in magnesium alloy AZ91 results from the following sequence of events: melted eutectic film formation in the periphery of the stir zone region, subsequent engulfing of melted eutectic films when the stir zone grows in width during the dwell period, and then penetration of α-Mg grain boundaries in the stir zone extremity and crack propagation when torque is applied by the rotating tool.

2.1.9 Interrelationships of Material Properties

Many material properties are interrelated in complex relationships. For example, Choi et al. (2019) examined the effect of grain size on the elastic modulus, yield strength, and hardness of 304L SS. An obvious observation is the linear dependence on grain size evident for these three material properties for 304L SS and heat treatments (Figure 2.8).

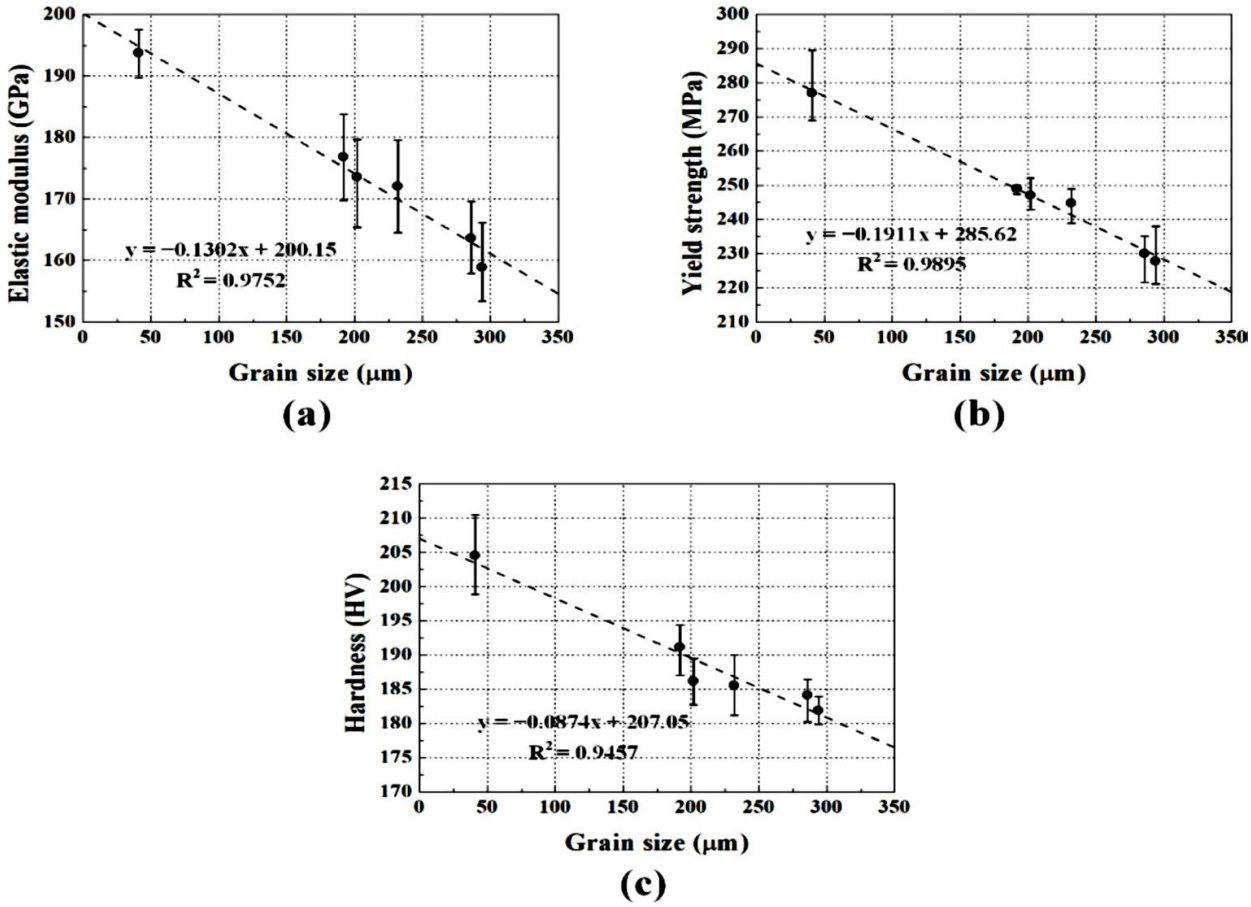

Figure 2.8. Material properties of a 304L SS sample acquired from tensile tests (a) elastic modulus; (b) yield strength; and (c) hardness as a function of grain size. Specimens were heat-treated at a constant temperature of 1250°C for different heat-treatment holding times of 0, 1, 5, 10, 25, and 34 hours, followed by water quenching. Source: (Choi et al. 2019)

3.0 Shear Assisted Processing and Extrusion

ShAPE is a solid-phase manufacturing process that also incorporates rotating mandril tools to stir the material, just like FSP welds stir the material during the extrusion process. This allows rods, tubes, and even some more complex shapes to be extruded. Material characteristics and potential process intrinsic defects are analogous to FSP weld material (Whalen et al. 2021). The ShAPE process and tooling were adopted for extruding thin-walled AA7075 aluminum tube from as-cast, non-homogenized billet material in a single run (Nazaeri Tiji et al. 2021). The mechanical and microstructural characterizations were performed on the extrudate in the as-extruded condition without subsequent heat treatment. It was shown that the ShAPE process developed a significantly refined microstructure with uniform and almost equiaxed grain structure on both the hoop and axial cross-sections of the extrudate as well as through the thickness of the material. The pole figures and inverse pole figures of the EBSD data showed a strong shear texture development, and it was found out that axial shear is the dominant deformation mechanism in the regions near the inner surface of the tube, while combined axial and torsional shears are the two dominant modes of deformation near the outer surface of the extrudate. As for the mechanical properties, there was an increase of 150 percent and 73 percent in the yield and ultimate strengths of the tube produced using the ShAPE process, respectively, and an 18 percent decrease in maximum uniform plastic elongation compared to the conventionally extruded AA7075-O tube. The capability of the ShAPE system is being adapted to harder, tougher materials like various SS alloys. Material characteristics are expected to track with the aluminum alloy material property improvement.

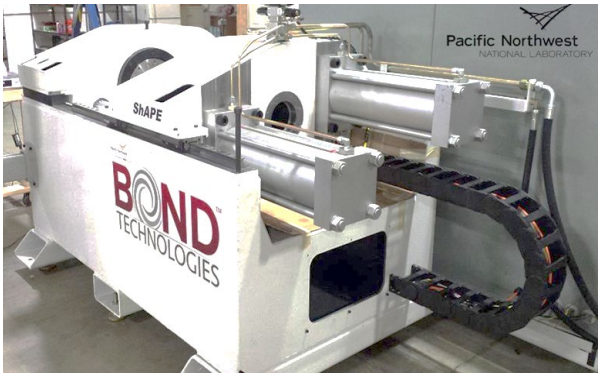

A. PNNL ShAPE unit.

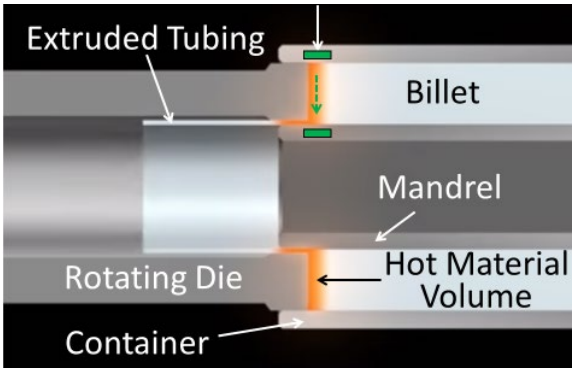

B. Concept of extruding a tube using billet material placed within a ShAPE manifold.

Figure 3.1. One of several ShAPE units at PNNL used for SPP extrusion studies.

4.0 Materials Characterization Tests Overview

There are many techniques that may be used to detect and characterize degradation and changes in material properties (Figure 4.1)((McCloy et al. 2013): acoustic (linear and harmonic/nonlinear, with measurements of velocity/attenuation/scattering/nonlinear parameters), magnetic (Barkhausen, DC hysteresis, leakage flux), electrical (eddy current, alternating current/direct current potential drop, impedance tomography, impedance spectroscopy, etc.), macromaterials tests (Young's modulus, yield/ultimate strength, hardness/micro-hardness), radiological imaging (x-ray imaging and tomography, electron beam imaging), micro-tomography (optical, florescent die), and atomic-force microscopy (including very small-scale characterization of mechanical and electrical properties). Each detection method can be realized by multiple sensor types (e.g., magnetic: coils, Hall sensors, magneto-optic, giant magnetoresistance (GMR), anisotropic magnetoresistance (AMR), superconducting quantum interference device (SQUID); acoustic: piezoelectric, magnetostrictive, EMAT = electromagnetic/acoustic).

Frequently, direct measurements of parameters of interest are only attainable using destructive testing methods or are applicable only to a small volumetric or surface region or area. But destructively measured parameters can often be related to results from nondestructive inspection testing methods that can be applied without damaging the component. Each of these nondestructive tests has applicability to a range of material assessments that span limited stages in the life of a material. These include on-line condition monitoring during manufacturing, post-manufacturing quality check characterization, post-manufacturing detailed material characterization, final component fabrication, pre-service inspection, and in-service material degradation inspection. Finally, the various nondestructive inspection testing methods are subject to practical limitations in terms of depth of penetration and scale of inspection (Figure 4.2 (Harrison 2007) (Figure 4.3) (McCloy et al. 2013)). These interrelations are not explored exhaustively but are addressed by select examples in the following sections.

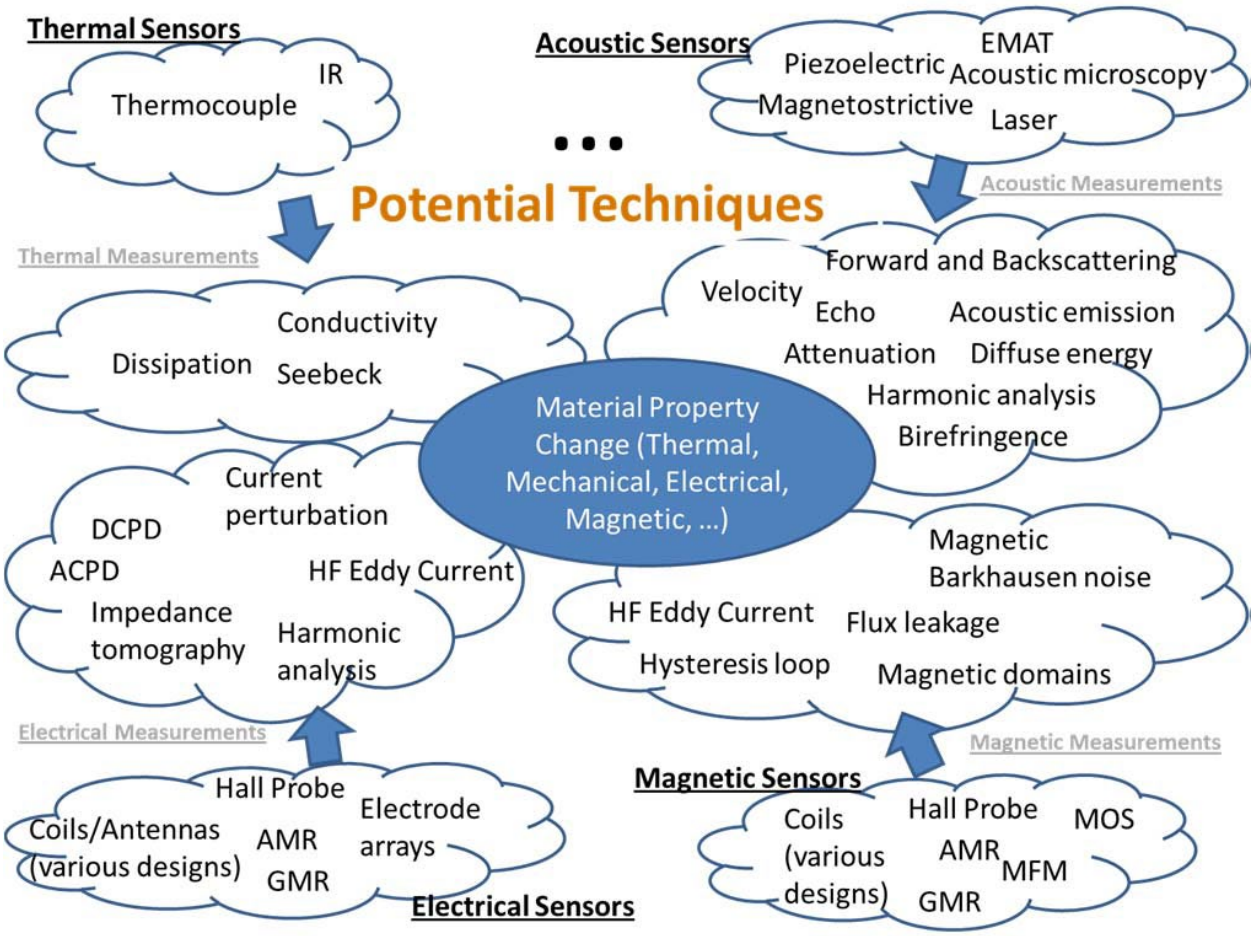

Figure 4.1. Non-exhaustive examples of materials characterization testing methods and sensors.

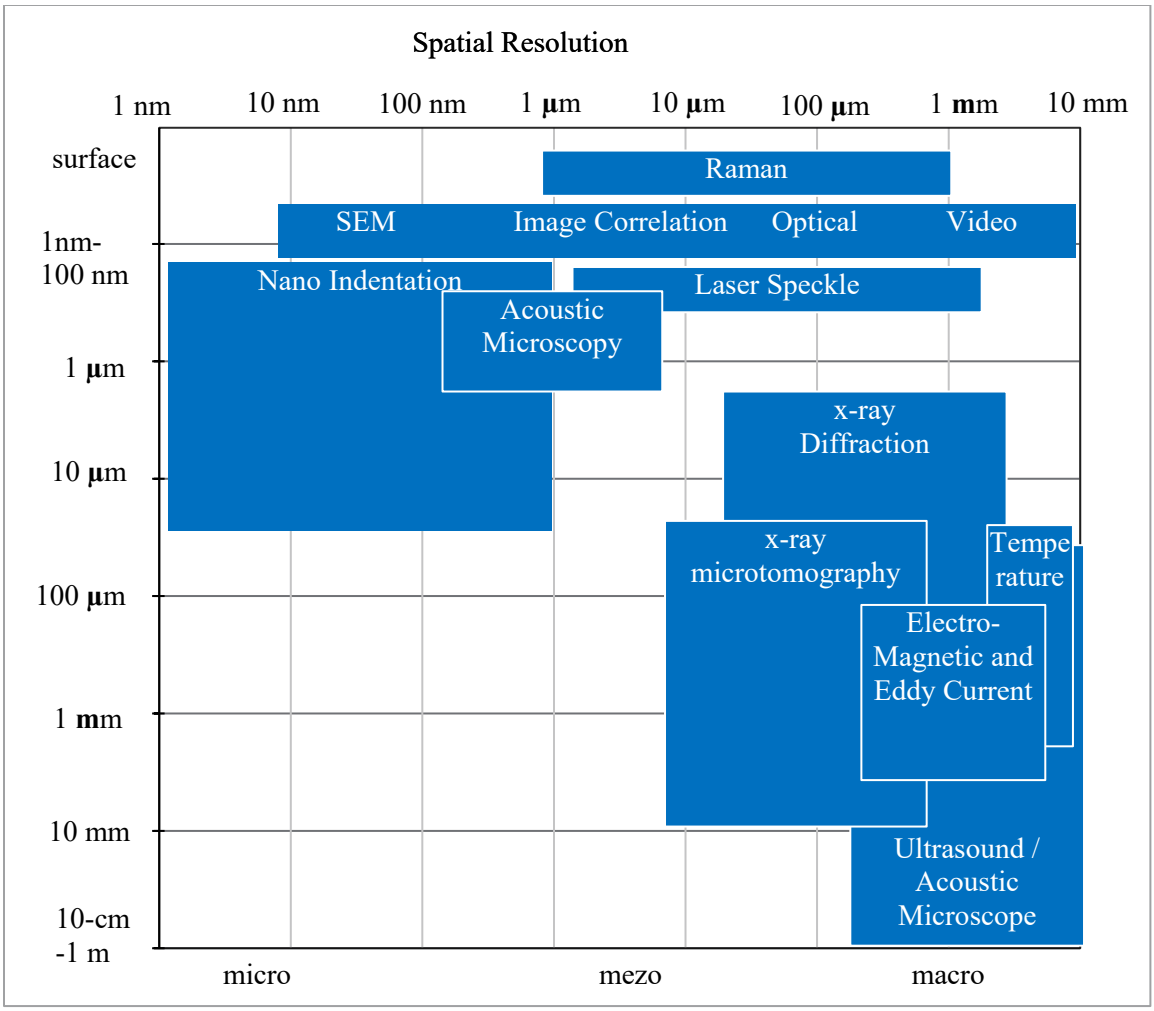

Figure 4.2. Nondestructive inspection testing methods are mapped based on depth of penetration (vertical axis) versus spatial resolution (horizontal axis).

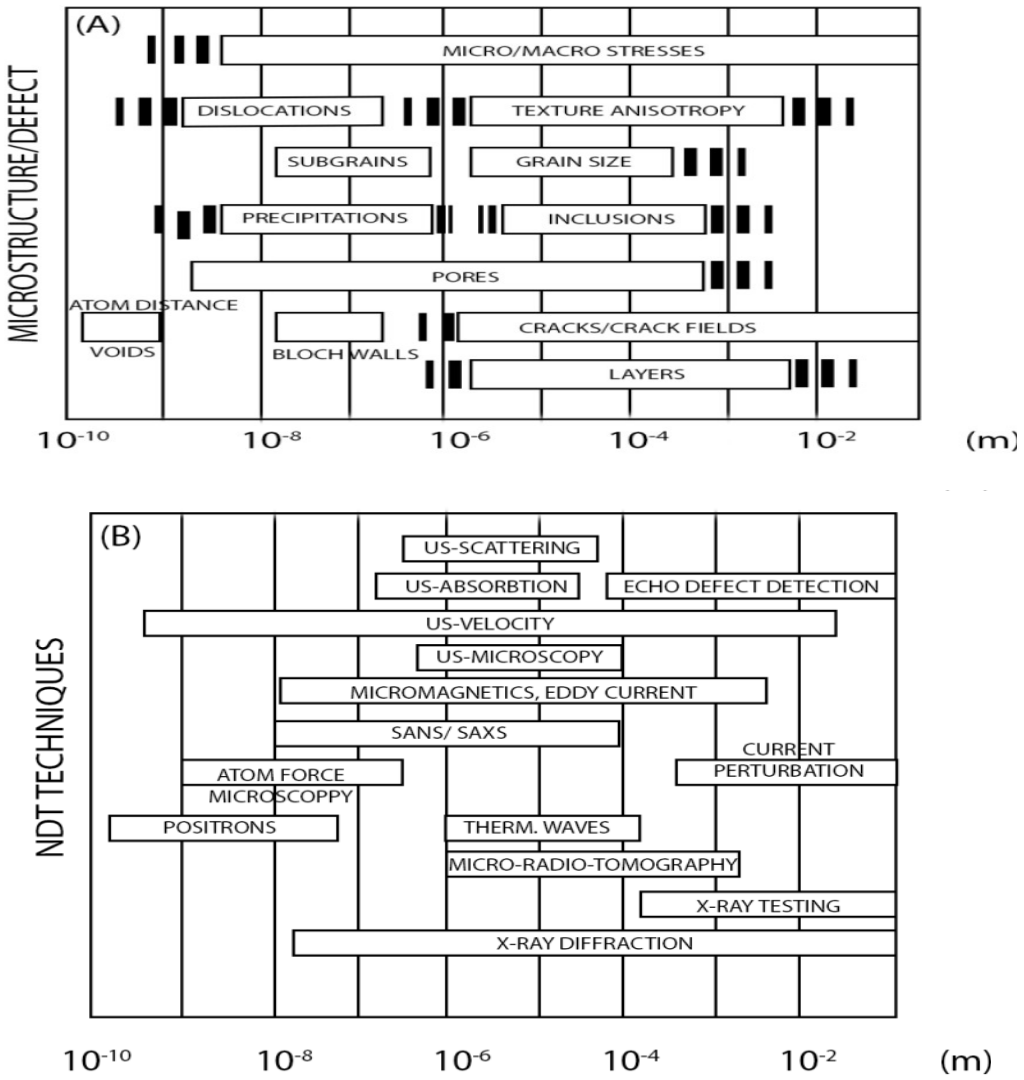

Figure 4.3. Spatial resolution mapping of material defects and nondestructive inspection testing methods.

5.0 Destructive Tests

5.1 Mechanical Tests

The cladding material utilized to encapsulate fissile material contained within nuclear fuel rods is among the most well-characterized and best-understood material types because of the safety-critical nature of its function in containing fission products. In one report commissioned by the U.S. Nuclear Regulatory Commission, PNNL was tasked with incorporating cladding mechanical property data into the U.S. Nuclear Regulatory Commission fuel codes that are used to justify safety assessments for plant operating licenses. The primary test data were uniaxial tensile tests (or biaxial tests normalized to a uniaxial stress state) that measure yield strength, ultimate tensile strength, and uniform percent elongation at break, as well as engineering and true stress/strain curves (Geelhood, Beyer, and Luscher 2008). A tensile testing machine applies tensile (pulling) force to a material and measures the specimen's response to the stress. The most commonly reported parameters are Young's modulus, yield stress, ultimate stress, and percent elongation at break. A typical tensile test plot is shown in Figure 5.1. These kinds of tensile tests directly measure material parameters of primary interest, but they are destructive tests and therefore cannot be performed on material or actual parts to be used in service.

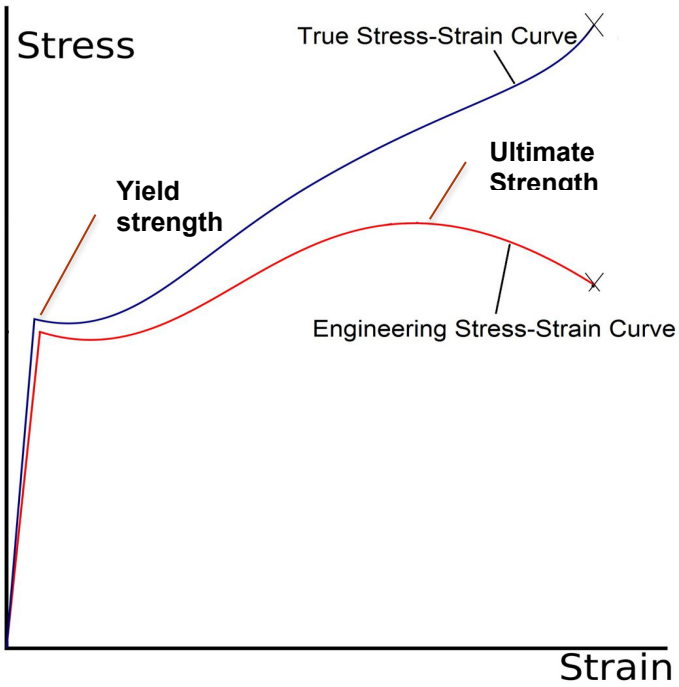

Figure 5.1. Example plot for mechanical tensile test. The difference between engineering and true stress-strain curves is that true-stress curves take into account the necking-down of the sample cross-section.

When material volumes are small, resonant ultrasound spectroscopy can accurately measure elastic modulus (Migliori and Sauuro 1997). The technique is destructive since a small material volume (approximately 2 mm-sided cuboid) is fabricated from available material. The specimen is typically suspended between two piezoelectric transducers at point contacts and frequency swept to obtain a series of resonances from which elastic moduli are estimated. A resonant ultrasound spectroscopy claim is the ability to provide high-accuracy moduli measurements of

the elastic moduli of anisotropic material. The ability to acquire measurements as a function of temperature allows transitions to be observed, such as microstructure phase, superconduction, and magnetic transitions at a Curie temperature. One example study evaluated thermal cycling effects upon thermoelectric materials (Biswas et al. 2011), (Biswas et al. 2012).

Austenitic steel tensile strength can vary significantly as a function of material grain size (Yuan et al. 2014). A high manganese austenitic steel, Fe-25Mn-3Cr-3Al-0.3C-0.01N (in wt. pct) with grain sizes of approximately 2.2 to 28.7 μm was obtained by annealing cold-rolled sheet at temperatures ranging from 700°C to 1000°C. The dependence of grain size on the mechanical properties and microstructures of this high manganese steel was studied by using scanning electron microscopy (SEM), transmission electron microscopy (TEM), and a room temperature tensile test. The results showed that, with the increase of grain size from 2.2 Pm to 28.7 μm, the yield and ultimate tensile strengths of this steel decreased from 410.0 MPa to 232.5 MPa (57 percent), and 725.0 MPa to 517.0 MPa (71 percent), respectively.

5.2 Micro Hardness

In microhardness testing, an indentation is made on the specimen by a diamond indenter through the application of a load *P* (Figure 5.2). The size *d* of the resultant indentation is measured with the help of a calibrated optical microscope, and the hardness is evaluated as the mean stress applied underneath the indenter. The measurement of hardness with a microscope attachment, comprising the indenter and means for applying small loads, dates back more than 50 years. Initially used for small components (watch gears, thin wire, and foils), microhardness testing was extended to research studies of individual phases, orientation effects in single crystals, diffusion gradients, aging phenomena, etc. in metallic and ceramic materials. Nowadays, testing at temperatures up to 1000°C is possible. In Europe, the pyramidal Vickers-type (interfacial angle 136°) indenter, which produces a square impression, is generally favored. Its counterpart in general engineering employs test loads of 5–100 kgf; in microhardness testing, typical test loads are in the range 1–100 gf (1 gf=1 pound=1 p=9.81 mN). A rhombic-based Knoop indenter of American origin has been recommended for brittle and/or anisotropic materials (e.g., carbides, oxides, and glass) and for thin foils and coatings where a shallow depth of impression is desired. The kite-shaped Knoop impression is elongated with a 7:1 axial ratio.

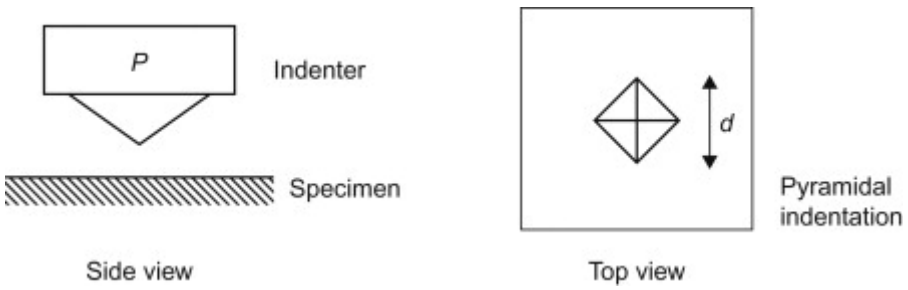

Figure 5.2. Schematic of a general micro-hardness diamond indenter tool and indentation.

Hardness testing introduces local plastic stresses and corresponding strains into the material and is generally considered a destructive test for coatings unless made in a non-working area. For many applications, finding or providing a non-working test area of a material may not be a problem, so from a practical perspective, hardness tests may be nondestructive. There is a concern, however, that the stress-risers associated with the hardness test may initiate cracks, pitting, or other more concerning damage mechanisms, and testing in high-stress segments of

the part is not recommended, so normally hardness testing is considered a destructive test. The most common hardness tests are Rockwell, Brinell, and Vickers. The measurement is typically made on a machined or ground surface to improve the dimensional characterization of the indentation. For the Vickers test (which is becoming more common due to low indentation forces and the standard diamond indenter head for all materials), the calculated Vickers hardness value (HV) is equal to the applied force (typically < 1000 Newtons) divided by the area of a diamond-shaped indentation device (ASTM 2017). In some applications, HVs provide a meaningful indication of other material parameters of interest like wear resistance, corrosion resistance, and Young's modulus. In one study examining cold spray samples (Glass et al. 2018), mean hardness was also indicative of porosity and cold-spray quality (Figure 5.3). An overview of hardness test advantages and limitations is shown in Table 5.1.

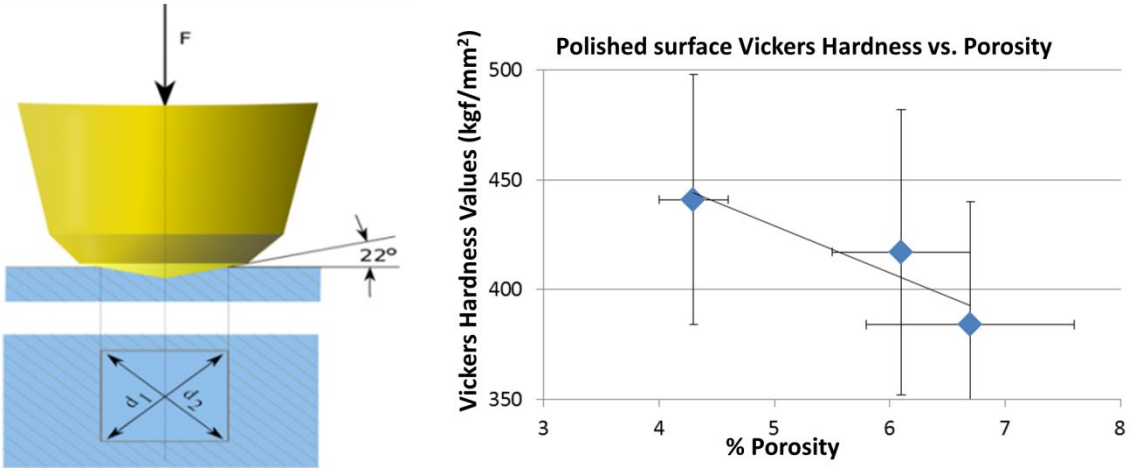

Figure 5.3. (left) Design of the Vickers hardness test indentation head; (right) good, fair, and poor cold spray (as indicated by their porosities versus Vickers hardness test values).

Table 5.1. Overview of Vickers hardness test applicability, advantages, and limitations.

	Applicability	Advantages	Limitations
Vickers Hardness	Primarily applicable to metals. Hardness may be a strong indication of wear and corrosion resistance. Can indirectly indicate yield strength.	No need for fluid coupling. Simple point test. Normally, a number of samples are taken for overall coating or base material representation. Lower force than Rockwell or Brinell. Relatively low cost.	Accuracy is improved if measurements are taken on a machined or ground surface. The method is not truly non-destructive in that indentation does create a stress riser that may develop into a crack or defect.

5.3 Correlation Between UT and Hardness

Ultrasonic wave propagation or behavior in solid materials is a function of material and microstructural properties as well as the material stress state; therefore, many studies have been performed relating ultrasonic parameters to these. Obviously, one interest is a path leading to nondestructive and potentially inline measurements for feedback control to assure the fabrication process remains stable to produce high-valued and consistent-quality material and parts. Common structural or state features include chemical composition, phase composition, grain size and shape, distributed inclusions, segregations and inhomogeneities, anisotropy, texture, and residual stress. Common ultrasonic parameters that can be measured include wave velocities of different wave modes, scattering, attenuation, or reduction of amplitude from absorption and scattering. More recently, nonlinear ultrasonic parameters have been investigated for embrittlement and KB characterization (Delrue et al. 2016).

Specific studies examining material hardness for specific alloys were examined. Many use ultrasonic wave velocity, which requires two accurate measurements: arrival time and distance. Selected studies are listed below in chronological order to show the progression of data acquisition and analysis:

- (Rosen et al. (1985) Aluminum alloy 2024 with different heat treatments produced 140 specimens that were examined with a 10 MHz tone-burst longitudinal (L) wave. L-wave velocity, attenuation, and electrical conductivity were measured. Plots of hardness versus L-wave attenuation showed monotonic decreasing functions or a one-to-one correspondence; however, different heat treatments produced different curves. Plots of hardness versus L-wave velocity showed that a HV mapped into several L-wave velocity values, meaning there was not a one-to-one correspondence.
- (Badidi Bouda, Benchaala, and Alem (2000) and (Badidi Bouda, Lebaili, and Benchaala (2003) examined the phase progression of martensitic, bainitic, bainito-perlitic, and ferrite-perlitic. L-wave velocity and attenuation coefficient, and shear (S) wave (also referred to as transverse waves) velocity and attenuation coefficient in XC38 steel for a range of grain sizes. A high scatter existed with wave velocity data. A better correlation existed with attenuation data.
- (Lukomski and Stepinski 2010) Specimens were rolled martensitic steel (AR400–AR600 abrasion resistant (AR), Brinell hardness value). Ultrasonic transducers were a 3.5 MHz L-wave (piezoelectric transducer) used in pulse-echo immersion and a polarized S-wave (shear wave) EMAT from Sonemat Ltd., UK, used in pulse-echo. A one-to-one relationship existed for all hardness versus L-wave and S-wave plots. Regression analysis was performed with 16 parameters, that is, 14 chemical element concentrations, tempering temperature, and velocity data. Nickel was the most significant for the S-wave velocity, and Cr was the most significant for L-wave velocity. The use of ultrasonic wave velocity with a single element concentration enabled hardness estimates regardless of the ARXXX steel type (Figure 5.4).

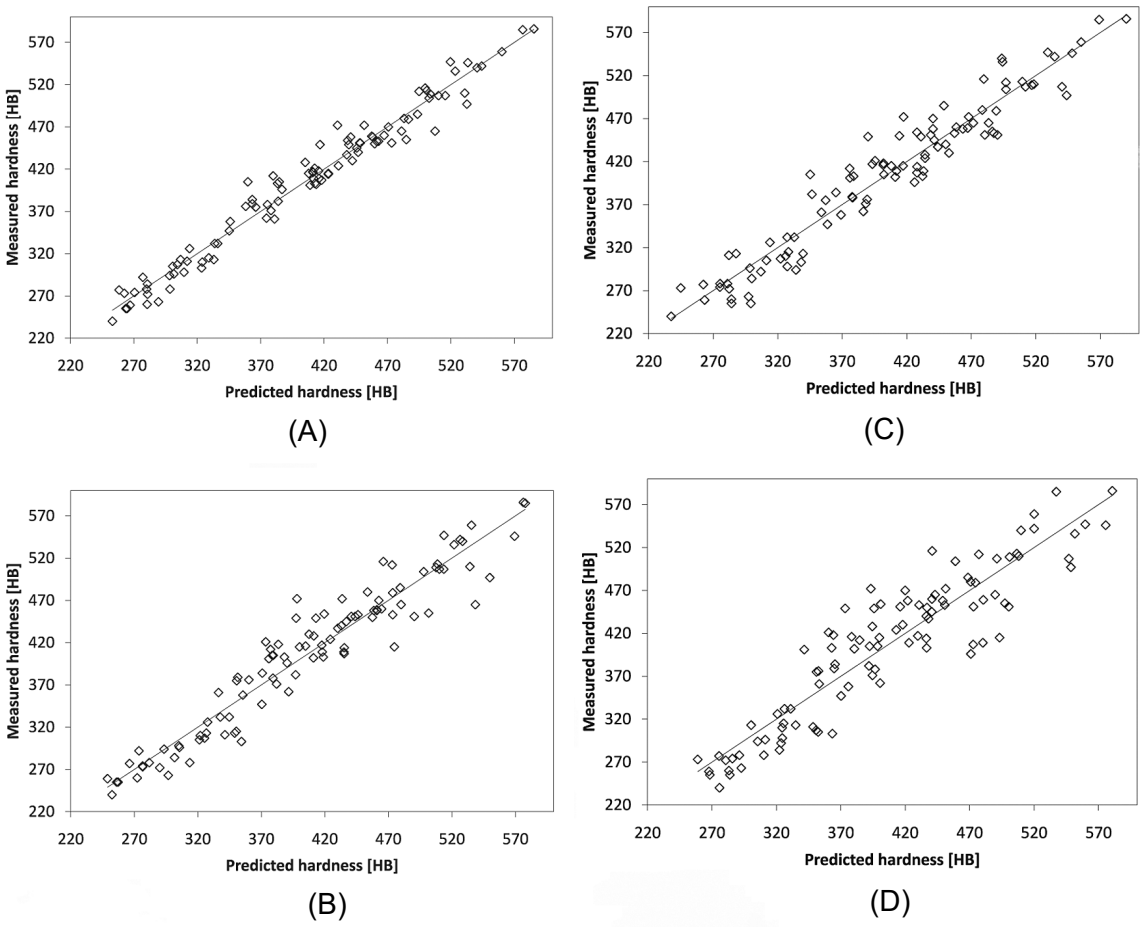

Figure 5.4. Brinell Hardness versus Algorithm Predicted Hardness for a matrix of ARXXX type steel at six tempering temperatures. (A) chemical element concentrations and S-wave velocity. (B) chemical element concentrations and L-wave velocity. (C) nickel and S-wave velocity. (D) Cr and L-wave velocity. Source: (Lukomski and Stepinski 2010)

- (Korde and Kundu 2013) – Six aluminum 2024 plates, each with a selected heat treatment, were examined. A Lamb wave was used in a pitch-catch configuration with two identical transducers of either 1 MHz or 3.5 MHz. A parameter defined as the normalized magnitude showed some separation of the respective plates.
- (Carreon et al. 2015) – Specimens were weld material from API X60 and X65 steels with hardness profiles across the weld cross-section. L-wave velocity at 5 MHz was measured across the weld cross-section. Plots of hardness versus L-wave velocity showed an increasing relation between the two for the two steel alloys, where hardness increases with L-wave velocity.
- (Uzen and Bilge 2017 and 2015) – Numerous specimens included three steel types with a submerged arc weld performed over a prepared groove centered in a continuous plate. Specimens were annealed at varying temperatures (Uzun and Bilge 2015). The analysis steps were as follows:

  1. L-wave velocity and hardness measurements were acquired over the range of 10 mm to 100 mm from the weld center.

2. Determine hardness change relative to the initial plate hardness and L-wave velocity change relative to the initial plate measurement and plot versus annealing temperature.
3. Determine hardness change versus the L-wave velocity change. A large variation exists, but a monotonic decreasing trend curve exists for each of the three different steel alloys. Coefficients for a quadratic function for hardness in terms of changes in L-wave velocity were estimated.
4. Residual stresses caused by the weld were stated as the primary source of changes in material hardness and L-wave velocity.
5. Plots were made of hardness estimated by L-wave velocity versus distance for the weld center line and compared to metallographic hardness versus distance for the weld center line. Both showed an increased hardness at 10 mm that continued to decrease to about 40 mm.
6. The 2015 work was updated in 2017 to address carbon content variations in low alloy steel to correlate hardness with ultrasound velocity (Uzun and Bilge 2017). Still, the correlation between changes in ultrasound velocity versus changes in hardness was strong (Figure 5.5 and Figure 5.6).

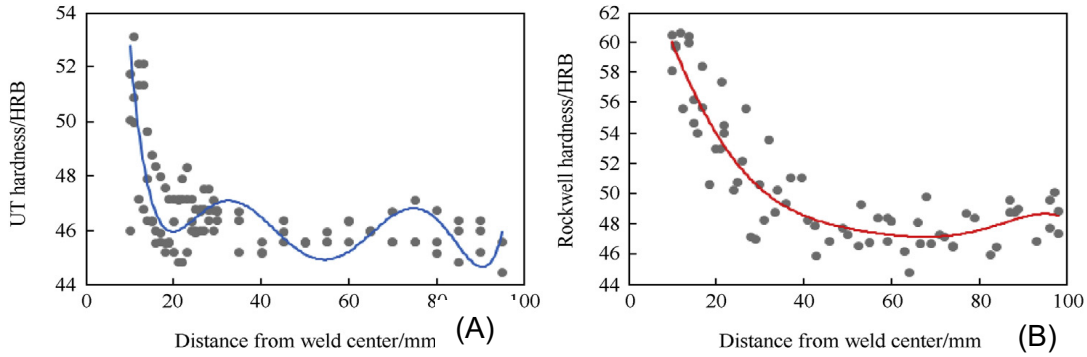

Figure 5.5. Hardness in interstitial free steel versus distance from weld center line. (A) Hardness estimated by L-wave velocity measurements. (B) Metallurgical measurements of hardness. Source (Uzun and Bilge 2015)

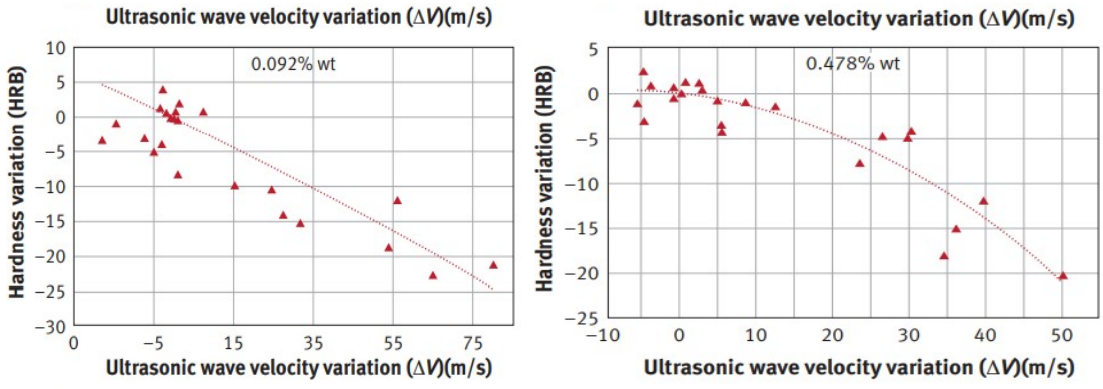

Figure 5.6. Rockwell hardness versus ultrasonic wave velocity variation for 0.092 percent (left) and 0.478 percent (right) carbon content in steel. Source (Uzun and Bilge 2017)

5.4 Optical Microscopy

Optical micrographs can be used to see and characterize many metal samples. This is typically a destructive technique whereby a sample is cut to reveal a cross-sectional exposed surface (Struers 2021). Frequently, the sample is embedded in an acrylic or epoxy block to facilitate handling, and then the surface to be examined is polished to a mirror finish with decreasing grit (typically using diamond, aluminum oxide, or colloidal silicon dioxide) on appropriate polishing cloths and disks. Low-concentrated etchants containing 1-3 percent nitric acid in ethanol (Nital) are often used for low-alloyed and medium-alloyed carbon steels or cast iron to clarify grain structures (Figure 5.7). Other color-reactive etchants are used for SSs. The selection of optical dies is material-specific. Optical methods can be sensitive to the detection and characterization of features as small as a few μm with magnifications from 50 to 500x. These images can be captured with conventional cameras optically adapted to the microscopes, and a wide range of image processing software can be incorporated to analyze the images for things like grain size averages, distributions, inclusion and flaw detection, 2-D montages of multiple images (Figure 5.8), and even tomographic build-up of 3-D maps by sequentially sectioning, polishing, and imaging the samples.

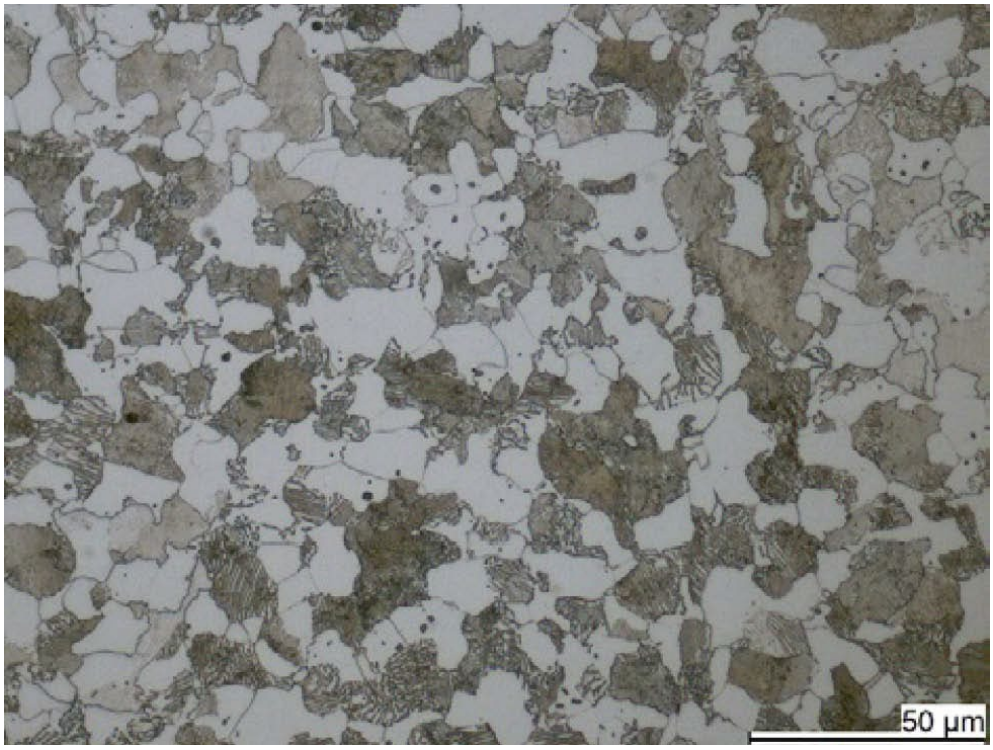

Figure 5.7. Example optical image of ferritic-pearlitic steel with approximately 0.2 percent C, etched with Nital. The carbon is primarily present as a cementite lamellar in a harder proportion of pearlite adjacent to the ferritic grains. This causes the cementite to appear streaky. The pearlitic grains reflect less light than the ferritic grains and thus appear darker. A matrix of this type has higher hardness but lower ductility. Image taken with ZEISS Axiolab, 50x objective, brightfield illumination. Source: (Struers 2021)

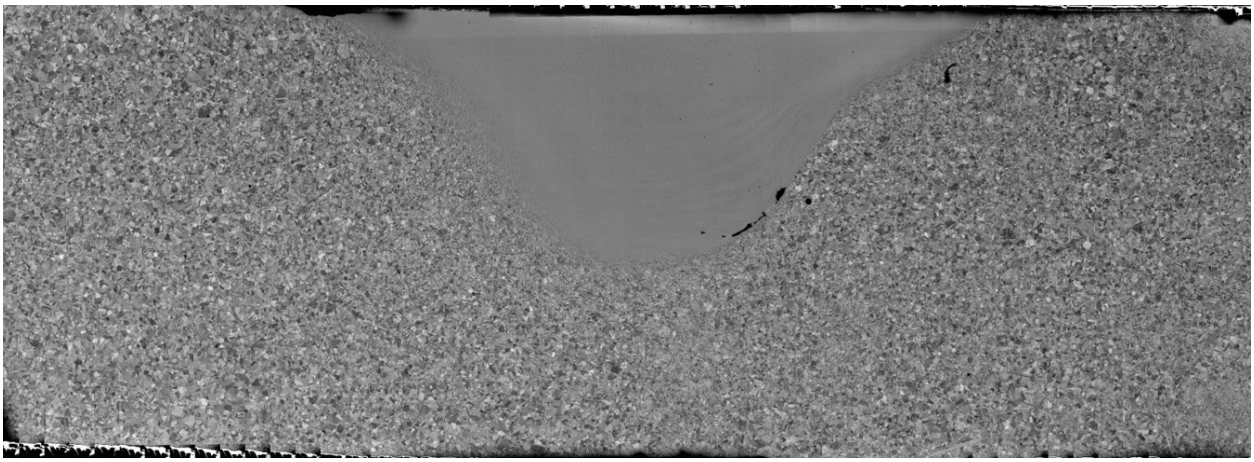

Figure 5.8. 2-D montage of over 300 micrographic images of an FSP.

5.5 Electron Microscopes

Electron microscopy is a valuable tool used to obtain high-resolution images in a variety of applications, including materials characterization and metallurgy. Electron microscopes can capture much higher-resolution images than light microscopes and can contribute information that is otherwise unattainable by conventional optical methods (Bruker 2022). Every electron microscope works by accelerating a focused stream of electrons in a vacuum toward a sample. Interactions between the electron beam and the sample create an image similar to optical microscopes that use light to capture images. The electron microscope image created reveals details of a sample's surface or internal composition, depending on the type of electron microscope that is used. SEM and TEM are the two most common types of electron microscopy. TEM and SEM differ in how they work and what types of images they capture, as outlined below.

5.5.1 Scanning Electron Microscopy

SEM is analogous to an optical microscope except that the image is produced by an electron beam reflection from a polished sample surface, but the image can be magnified significantly more, and there is additional elemental information not available from the optical image. SEM uses a fine beam of focused electrons to scan a sample's surface. The microscope records information about the interaction between the electrons and the sample surface, creating a magnified image with information about topography and elemental composition. SEM has the potential to magnify an image up to 2 million times. SEM can capture 3-D black-and-white images of thin or thick sample surfaces. The sample's size is limited only by the size of the electron microscope chamber, which is typically less than 100-mm dia. × 40-mm high. To generate an SEM image, an electron source (also known as an electron gun) emits a stream of high-energy electrons toward the sample (Figure 5.9). The electron beam is focused using electromagnetic lenses. Once the focused stream reaches the sample, the beam and detectors are steered to perform the raster scan. Interaction between the electron beam and the sample creates secondary electrons, backscattered electrons, and x-rays. These interactions are captured to create a magnified image.

5.5.2 Transmission Electron Microscopy

A TEM images the sample's influence on the electron beam as it passes through a thin sample en route toward the imaging detector. Samples must be quite thin, usually less than 150 nm thick, to allow electrons to pass through them. After the transmission of the electrons through the sample, they arrive at a detector below, and a 2-D image is created. TEMs have a magnification potential of 10–50 million times. The details provided are at the atomic level, the highest resolution of any electron microscope. TEMs are often used to examine molecular and cellular structures.

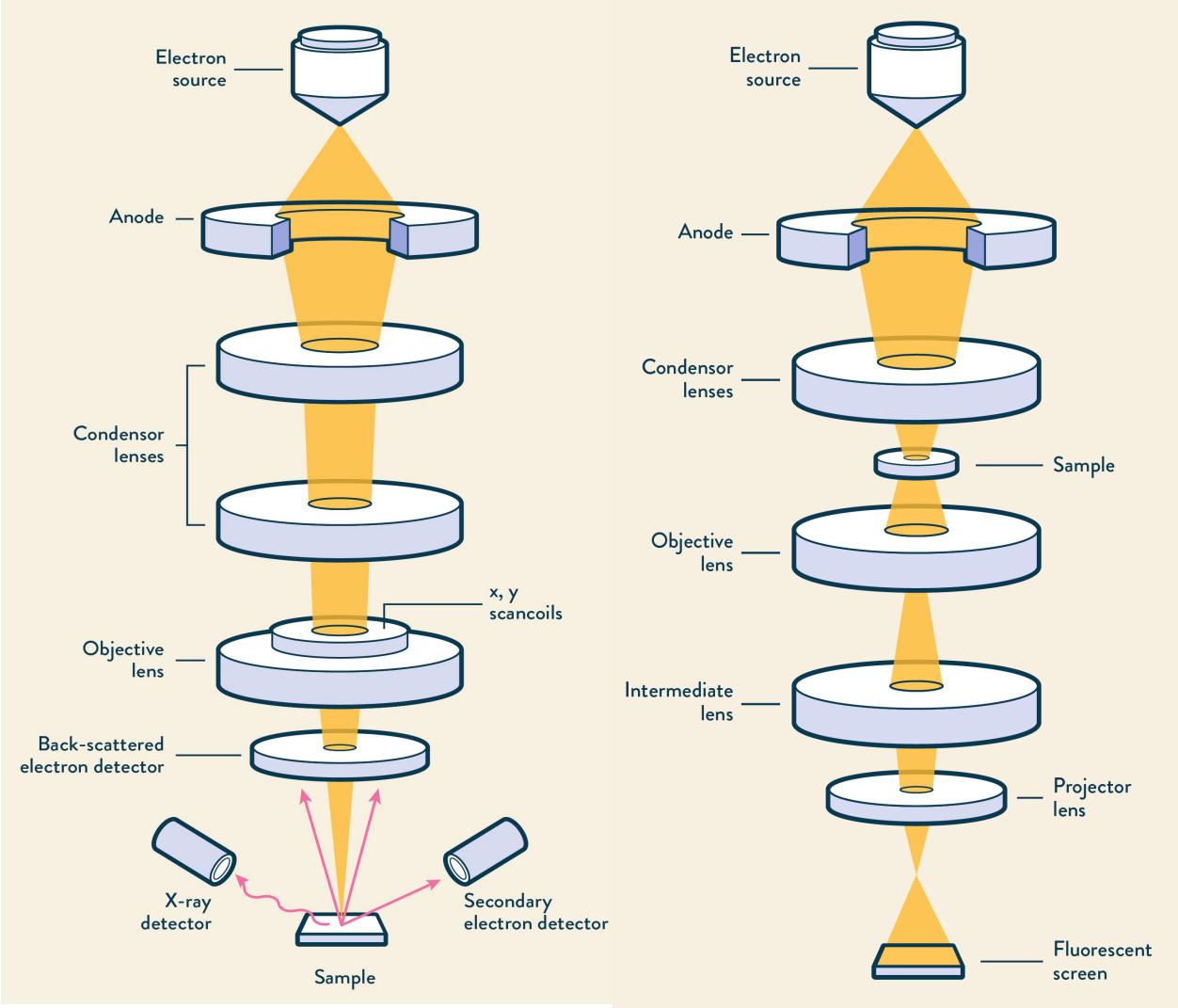

Figure 5.9. (left) SEM with both x-ray and secondary electron detectors receiving reflected energy from sample surface. (right) TEM images of thin sample influence on electron beam passing through sample.

5.5.3 Electron Backscatter Diffraction

EBSD microscopes offer a special case of an SEM technique for metallurgical examinations, particularly for grain size, orientation, and strain. EBSD uses the interaction of the beam with a localized, periodic arrangement of atoms to generate diffraction patterns that can be captured

with a unique camera-beam-detector geometry (Hefferan 2020) (Figure 5.10). This is particularly useful for grain mapping, and if the sample can be strained, the relative EBSD measurements can characterize changes in grain orientation and grain dislocations.

EBSD serves as either a complement or alternative to other crystallographic analysis techniques such as TEM and x-ray diffraction, with the added benefit of high-resolution, spatially resolved, phase/orientation mapping.

Unlike TEM analysis, where diffracted electrons pass through the analyzed region, EBSD imaging uses reflected electrons that have diffracted from atoms on the surface of the specimen. By operating as a surface analysis technique, EBSD is well suited for evaluating large, polished surface areas, which is often infeasible with TEM, where extremely thin (nanometer) samples and consequently small areas are necessary to limit attenuation of the diffracted signal.

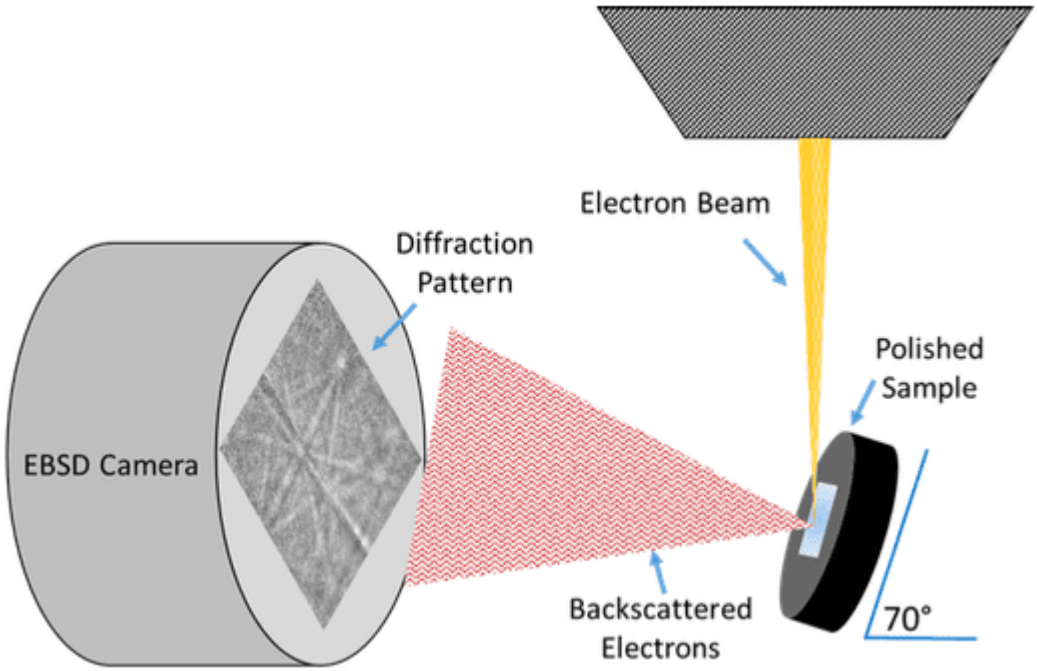

Figure 5.10. EBSD configuration: a crystalline sample, oriented @ 70° with respect to normal beam incidence, produces a diffraction signal from backscattered electrons that can be collected on a phosphorous screen camera.

5.6 Sample Materials Study of Aluminum FSP Including SEM, TEM, and Hardness

In one example study, optical, SEM, TEM, and hardness tests were applied to the FSP of a 6061 aluminum alloy (Liu et al. 2004). The material was 6 mm thick 6061 aluminum alloy plates treated in the T6 condition with a chemical composition of Si 0.71, Fe 0.18, Cu 0.30, Mn 0.07, Mg 1.14, Cr 0.14, Zn 0.03, Ti 0.02, and balance aluminum (all in mass%). The plates were held in compression and rigidly clamped to a milling machine for welding. The FSP tool diameters of the larger shoulder and small pin were 20 mm and 6 mm, respectively. The rotating tool was aligned flush along the contact line and parallel with the surface of the clamped metal plates.

This created an integral joint through severe plastic deformation of the material affected by the passage of the stirring tool. After the FSP, specimens were cut and mechanically polished first with 1000 grit and 1500 grit silicon carbide paper and then with 3 μm and 1 μm diamond paste. The final polishing of these specimens was accomplished using colloidal silica. After polishing, specimens were etched in a nitric acid/methanol solution at 273 K. After these treatments and preparation for optical microscopic observation and EBSD imaging, significant images and observations are as follows:

- Figure 5.11 shows the optical overview of the FSP with the principal regions labeled.
- Figure 5.12 shows Vickers micro-hardness readings across the weld top, middle, and bottom.
- Figure 5.13 shows that EBSD images of leading and trailing FSP regions are not homogeneous, but the strong dynamic plastic flow in TMAZ was exhibited in both the advancing and retreating sides of the FSP.

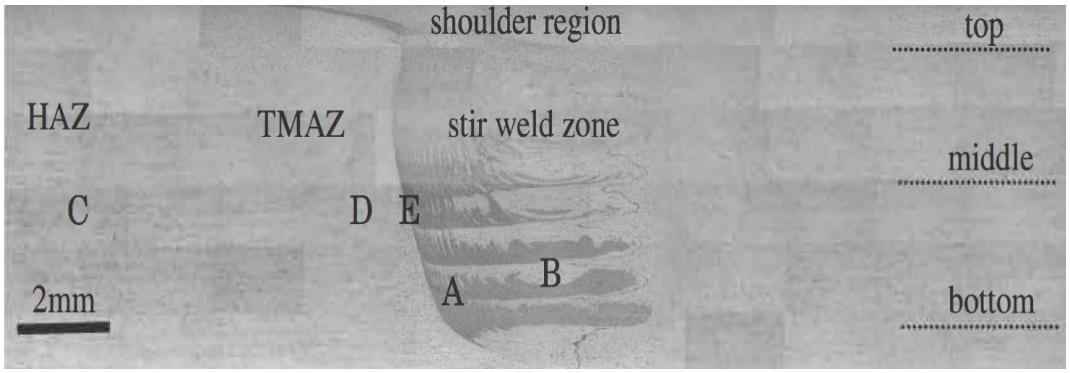

Figure 5.11. Cross-section of the optical overall micrograph in the FSP area, perpendicular to the tool traverse direction, the specimen produced at the tool rotation speed of 1100-rpm and a traverse velocity of 104 mm/min.

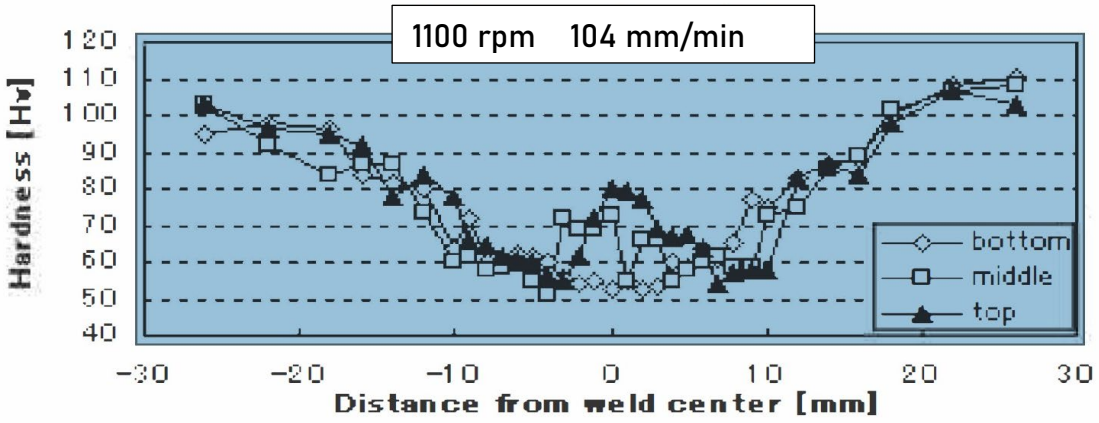

Figure 5.12. Vickers microhardness traverses through the section in Figure 5.11 along horizontal top, middle, and bottom dotted reference lines.

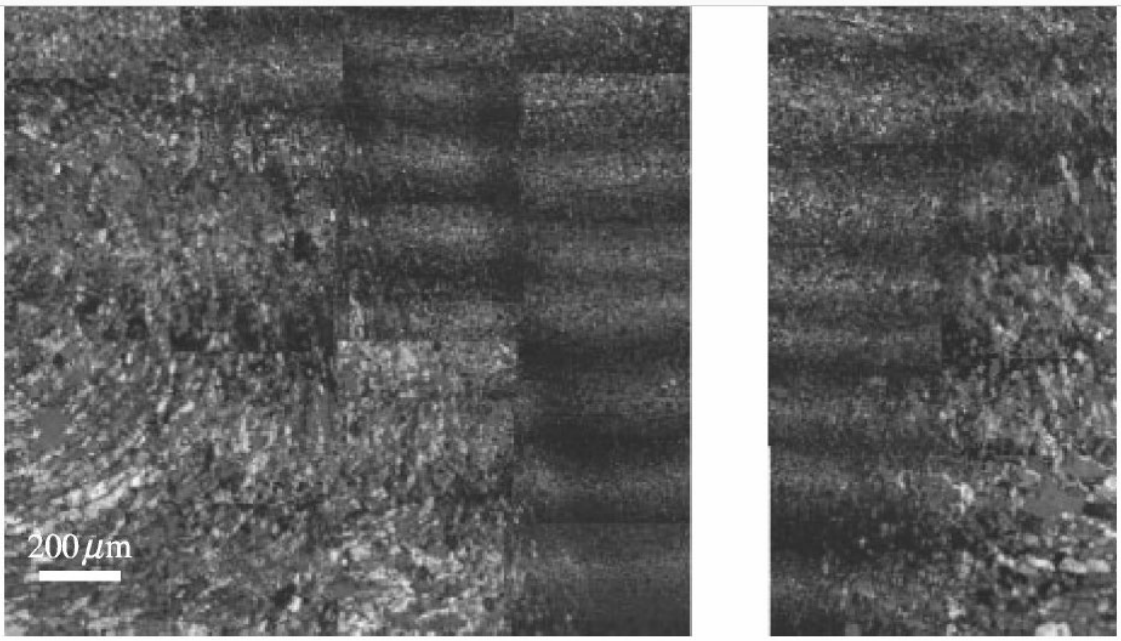

Figure 5.13. EBSD grain map of an FSP produced at 104 mm/min, 1100-rpm (left) transition zone on the retreating side (right) transition zone on the advancing side.

6.0 Nondestructive Tests

6.1 Temperature Using Tool-Mounted Thermocouples

Temperature is an important process parameter that can be indicative of an FSP or ShAPE material's quality. The temperature of the tool and the weld will change as a function of tool pressure, rotation speed, tool advance speed, and position on the tool. The weld temperature can also correlate to the presence or absence of porosity variations, incomplete weld bonds, cracks, and other anomalies. Although it is challenging to mount thermocouples to rotating components of the FSP or ShAPE process, it is possible to imbed thermocouples in the tools and use wireless telemetry to transition from the moving piece to on-line data recording instruments. Thermocouple measurements strongly depend on their relative position in the tool. Through numerical modeling, Ross (Ross 2012) showed the temperature response at various thermocouple locations on the tool and stated that distance from the thermocouple to the tool-workpiece interface increases the time delay and time constants during online temperature measurements. Due to the asymmetrical characteristics presented during the FSP, this method is questionable for representing the exact welding temperature at the weld joint but can provide a relative indication. For FSP of thick aluminum, researchers added thermocouples to the tip, corner, and shoulder of the stir spindle (Silva-Magalhães et al. 2019) (Figure 6.1). When these single-point measurements are synchronized with the spindle rotation, several measurements can be achieved for each rotation, thereby providing a thermal profile of the FSP. Bead-on-plate welds in 20-mm thickness (AA6082-T6) were produced while the temperatures were measured in three locations on the FSP tool. It was found that the hottest point in the stirred zone was 607°C and was located at the transition between the shoulder and probe, on the retreating-trailing side of the tool. The lowest temperature was found at the probe tip on the retreating-leading side of the tool, and the temperature varied by approximately 15°C between the leading and trailing orientations of the spindle (Figure 6-2).

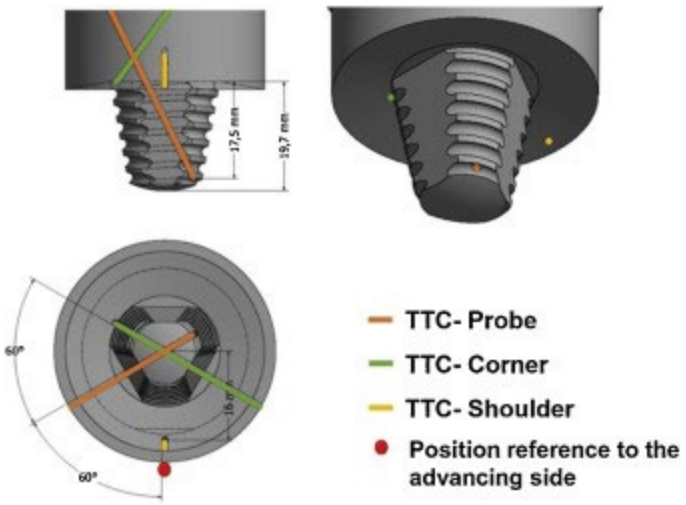

Figure 6.1. TTC corner thermocouple response changes cyclically as a faction of spindle rotation.

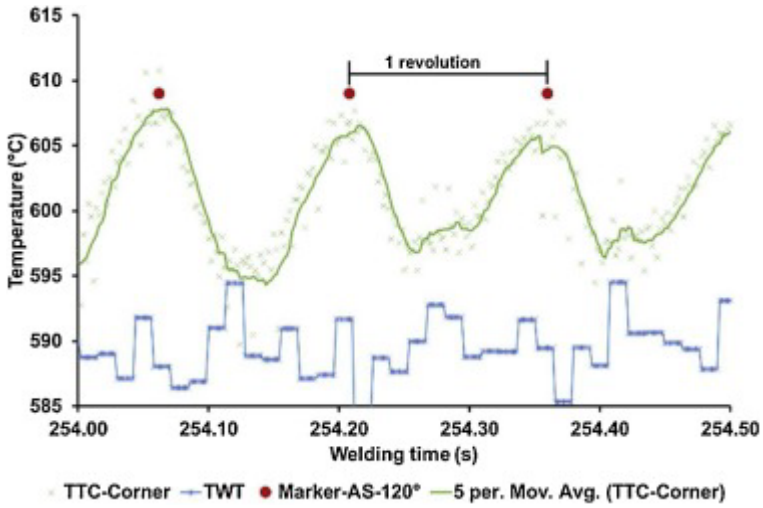

Figure 6.2. Thermocouple locations on an FSP tool for 20-mm thick aluminum.

6.2 Temperature and Surface Profile Using Infrared and Optical Camera Following the FSP

Traditional optical and infrared thermal cameras following immediately behind the weld can capture optical images for analysis of surface profiles and weld-cooling surface images that can indicate subsurface anomalies (Mężyk and Kowieski 2013). The test configuration is shown in Figure 6.3. Recordings were made of the welding process for different values of the rotary and linear velocities of the tool. With variable parameters of velocity, one can obtain welds of different quality: both normal welds and non-compliant welds. The defects included excessive burrs, discontinuities, an uneven edge of the weld, and others. The recorded thermal images allow identification of weld defects and non-compliances during the process. The use of a thermal imaging camera also allows the detection of subsurface defects. The obtained results indicate its potential practical application.

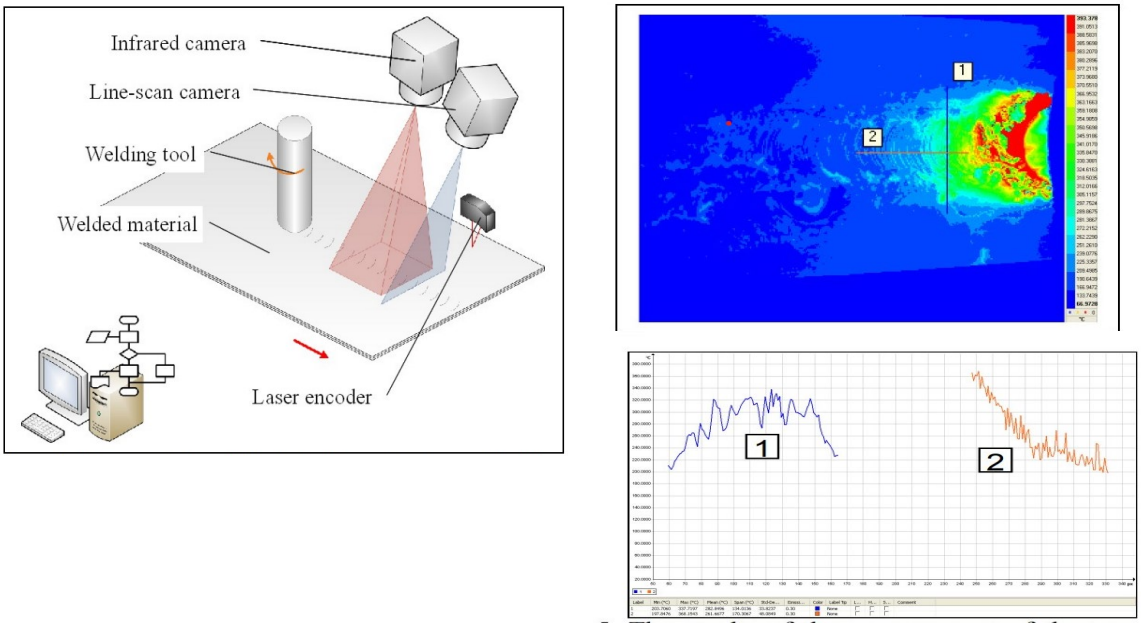

Figure 6.3. (left) Camera positioning following directly behind the FSP. (upper right) Thermal image following behind the FSP. (lower right) (1) vertical cross-section across the weld (2) horizontal cross-section along the weld centerline.

Typical optical non-conformances indicated by uneven weld edges, excessive burr on the edges, and cracks as an effect of overheating are shown in Figure 6-4.

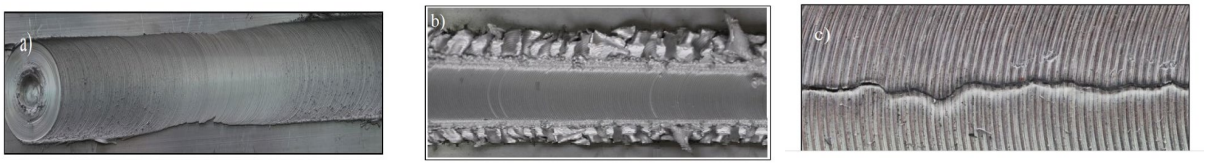

Figure 6.4. (a) uneven weld edge (b) excessive edge burr (c) cracks from overheating.

6.3 Subsurface Temperature Using Ultrasonic Velocity and Attenuation

Simple thermal models based on temperatures measured at the boundary of the deforming body cannot capture the dynamic nature of temperature generation within the deforming solid. One possible way of understanding internal temperature is by measuring sound velocity, which is a function of temperature for materials, and directing ultrasonic wave propagation through selected material volumes of interest. EMAT and laser-based ultrasound offer a means to implement such measurements (Good, Forsi, and Grant 2020). EMATs tend to have a large footprint, and laser-based ultrasound can be accomplished with a standoff and fiber optics that may facilitate such a measurement in regions close to the FSP tool. One-wave velocity as a function of temperature ((Lynnworth 1989), 41, 240-241, 370, 394-398). Figure 6.5 shows a measure concept, supporting data that metals and ceramic materials have an ultrasonic wave velocity that is a function of temperature, and a few specific examples of shear (S) and longitudinal (L) wave velocity for several different steel alloys.

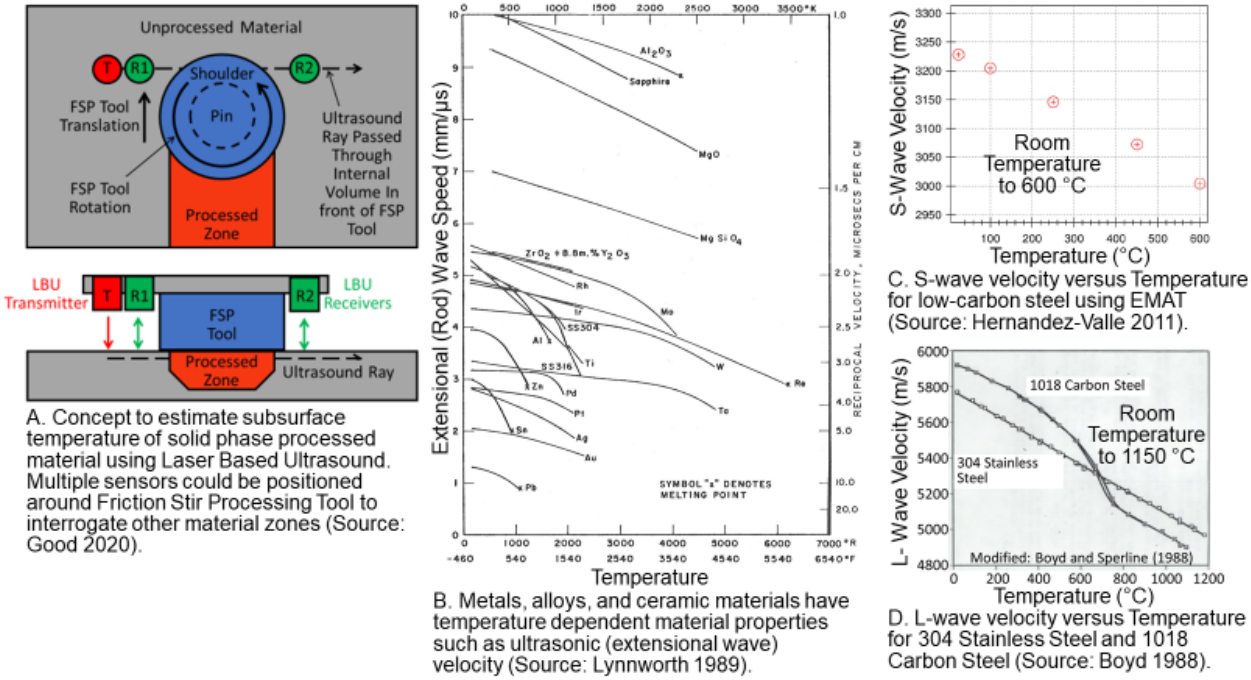

A. Concept to estimate subsurface temperature of solid phase processed material using Laser Based Ultrasound. Multiple sensors could be positioned around Friction Stir Processing Tool to interrogate other material zones (Source: Good 2020).

B. Metals, alloys, and ceramic materials have temperature dependent material properties such as ultrasonic (extensional wave) velocity (Source: Lynnworth 1989).

C. S-wave velocity versus Temperature for low-carbon steel using EMAT (Source: Hernandez-Valle 2011).

D. L-wave velocity versus Temperature for 304 Stainless Steel and 1018 Carbon Steel (Source: Boyd 1988).

Figure 6.5. Concept of using ultrasonic wave velocity to estimate the subsurface temperature of a material volume undergoing solid-phase processing.

6.4 Grain Size Estimate by Ultrasonic Backscatter

Ultrasonic backscatter can image localized changes in material microstructure (depth of hardening steel parts—axles, cam lobes, bearing races), gradients between hardened and core microstructure, run-out of hardened steel parts, stamping pattern, and metal-matrix composites (aluminum with SiO_2 particle reinforcement) (Good and Rose 1984). Metallic materials are generally made up of a continuum of singular crystalline volumes known as grains, which form during solidification as atoms align in a highly ordered manner. Grain structure, size (average diameter), and orientation are dependent on alloy composition and fabrication processes. Grains may exceed several centimeters, as in the case of large cast SS components; however, attention here is directed toward grains on the order of 25 µm and as small as 1 µm. Grain size is a key parameter since many material properties are affected by grain size (Figure 6.6) (Yuan et al. 2014). Each grain is anisotropic, meaning that material properties such as ultrasonic wave velocity are dependent on orientation relative to lattice parameters. A quasi-isotropic material condition exists if a material volume is large relative to grain size and grain orientation is random. As an ultrasonic wave passes the boundary between successive grains, transmission and scattering are dependent on the changes in acoustic impedance (the product of density and wave velocity). For a pulse-echo ultrasonic configuration, some scatter returns back to the transmitter, hence the term backscatter. Many metals and alloys of interest have a cubic anisotropic structure, and thus ultrasonic scattering and related phenomena provide a basis for material characterization (Figure 6.7). Goebbels provides a detailed discussion concerning microstructure analysis by scattered ultrasound and the data acquisition instrumentation of that period (Goebbels 1980).

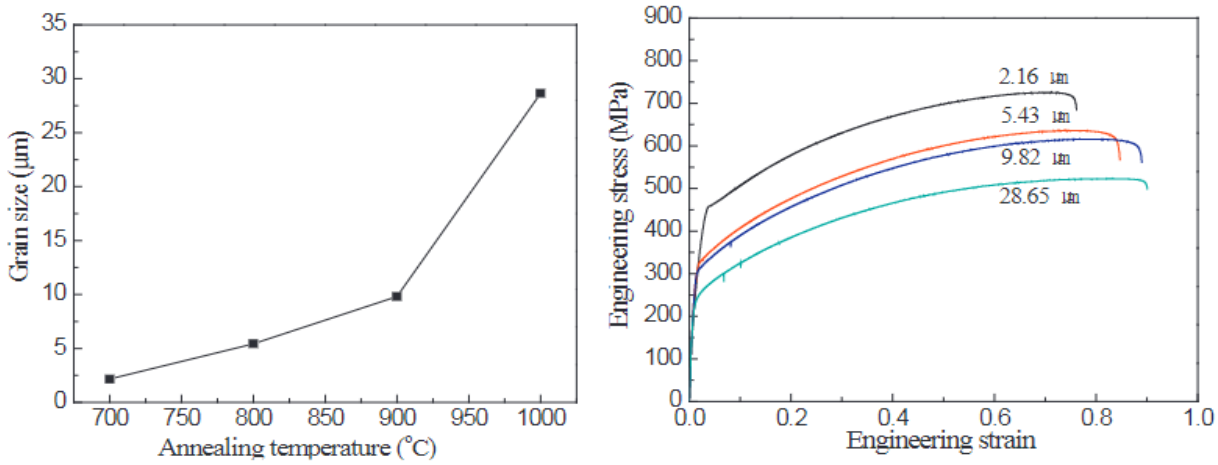

A. Dependence of grain size with annealing temperature.

B. Dependence of proportionality limit, elastic limit, yield point, ultimate strength, and failure with gain size.

Figure 6.6. Dependence of material properties on grain size for high manganese austenitic steel specimens. Source: (Yuan et al. 2014)

The backscatter of shear waves is much greater than longitudinal waves for materials such as steel. In a simplistic way, the reflection factor between two materials is $R = (Z_2 – Z_1)/(Z_2 + Z_1)$, where

- Z_1 is the acoustic impedance (product of wave velocity x density) of the material of the wave on the near side of a grain boundary.
- Z_2 is the acoustic impedance of the material on the far side of the grain boundary.

If the density of one grain to another is the same, the reflection factor is roughly proportional to the difference of the wave velocities of the regions that is dependent on the orientation of the grain. Examining the velocity curves for a grain of iron or more specifically 304 SS (Figure 6.8), an approximately 10 percent change in the L-wave velocity occurs with different orientation angles and similarly an approximately 50 percent change occurs for the S-wave velocity (Kupperman and Reimann 1980). Thus, the reflection factor or scattering is many times higher for S-waves relative to L-waves.

Goebbels also does a direct comparison of backscatter for Rayleigh scattering (where grain size is much smaller than the ultrasonic wavelength) and estimated that the Rayleigh Scattering Coefficient for S-waves is a factor approximately 48 times higher relative to L-waves (Goebbels 1980). Making various assumptions, the scattering coefficient as a function of grain size and ultrasonic frequency is estimated as follows:

$a_S \propto S d^3 f^4$, where a_S is the Scattering Coefficient, *d* is the grain diameter, and *f* is the wave frequency, and *S* is a coefficient (Goebbels 1980)

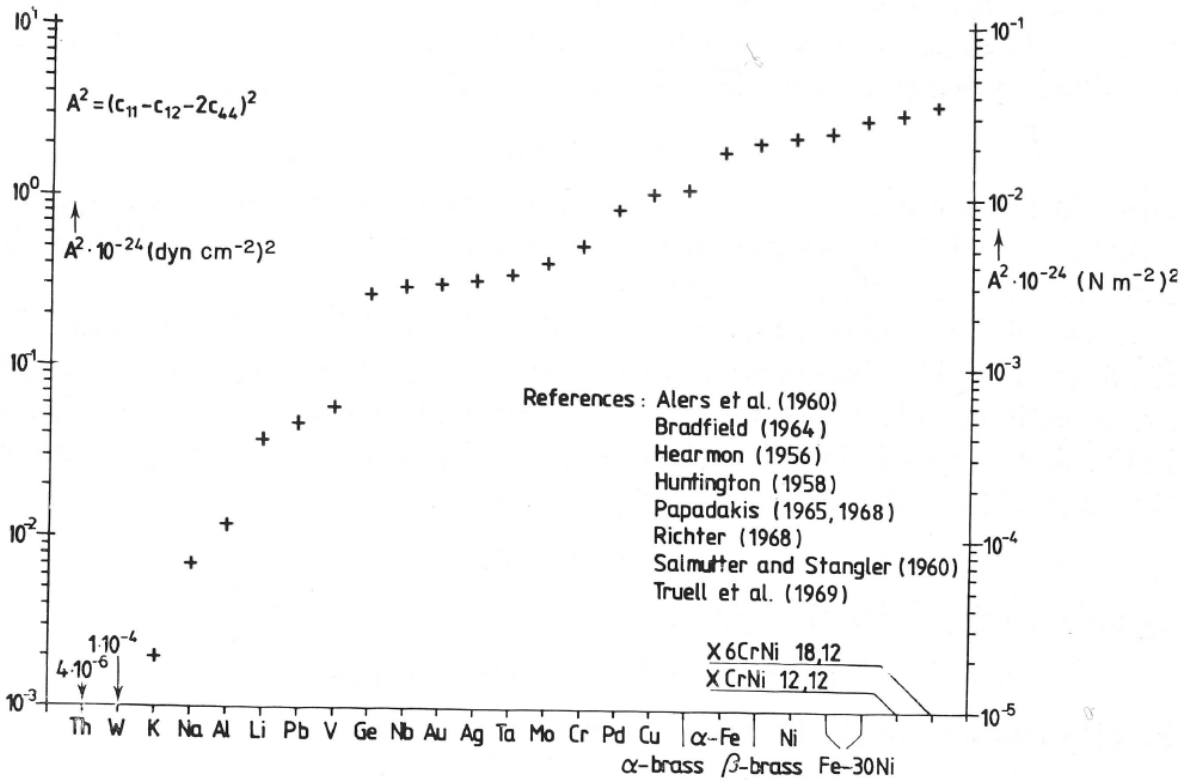

Figure 6.7. Anisotropy factor for cubic metals and alloys (Goebbels 1980).

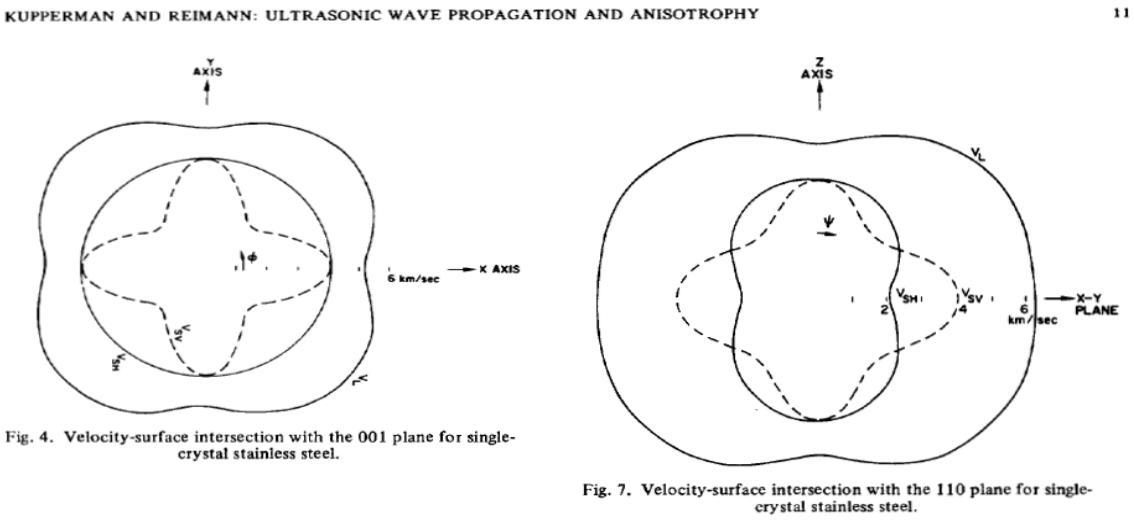

Fig. 4. Velocity-surface intersection with the 001 plane for single-crystal stainless steel.

Fig. 7. Velocity-surface intersection with the 110 plane for single-crystal stainless steel.

Figure 6.8. Wave velocity surfaces for a single grain of SS. Source: (Kupperman and Reimann 1980)

The backscatter coefficient is a function of grain size to a cubic power and frequency to a fourth power. Observations show that backscatter is biased toward the larger grains of a grain size distribution and scatter is biased toward higher ultrasonic frequencies (smaller wave lengths) that create an apparent decrease in amplitude as a function of penetration (Figure 6.9). Ultrasonic estimates of grain size using these techniques are shown in Figure 6.10 over the range of about 10–200 μm.

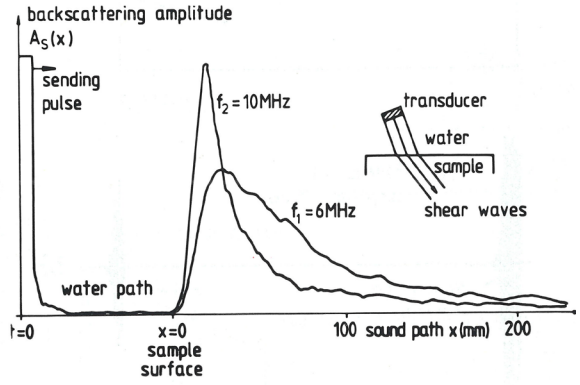

A. Shear wave backscatter.

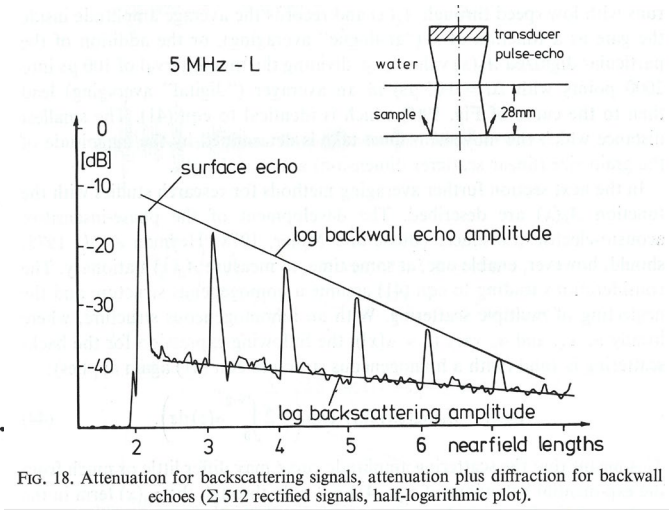

FIG. 18. Attenuation for backscattering signals, attenuation plus diffraction for backwall echoes (Σ 512 rectified signals, half-logarithmic plot).

B. Longitudinal wave backscatter and reverberation of front and back surface responses.

Figure 6.9. Typical amplitude versus time responses of backscatter in a pulse-echo configuration for shear waves and longitudinal waves. Source: (Goebbels 1980)

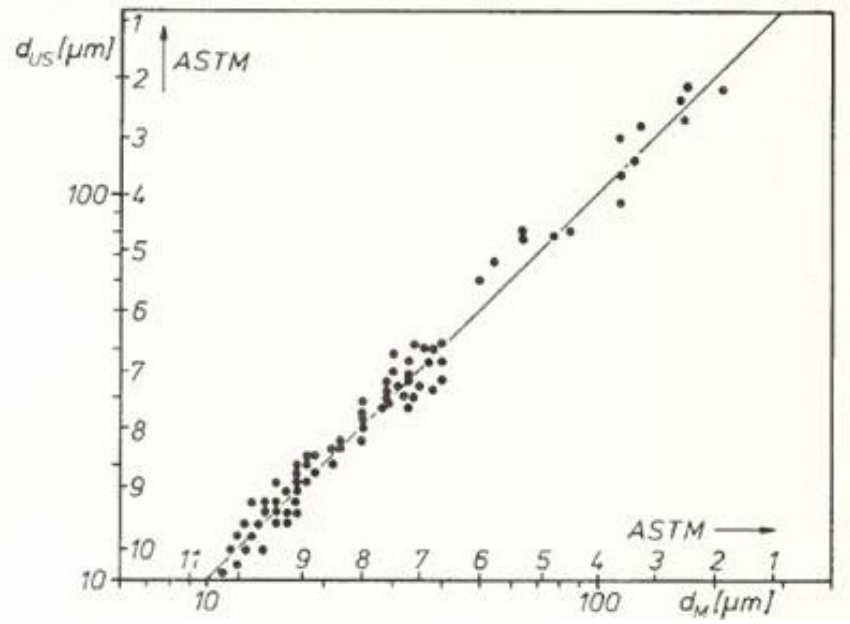

Figure 6.10. Comparison between grain-size determination by ultrasonics and by metallography. Source: (Goebbels 1980)

More recently, shear wave backscatter was used to estimate the grain size of friction stir processed volumes of a 316 SS plate with grain sizes ranging from about 2 to 18 µm (Figure 6.11) (Guo and Todd 2022). The RMS estimate of grain noise at 20 MHz is plotted against the average metallurgical grain size.

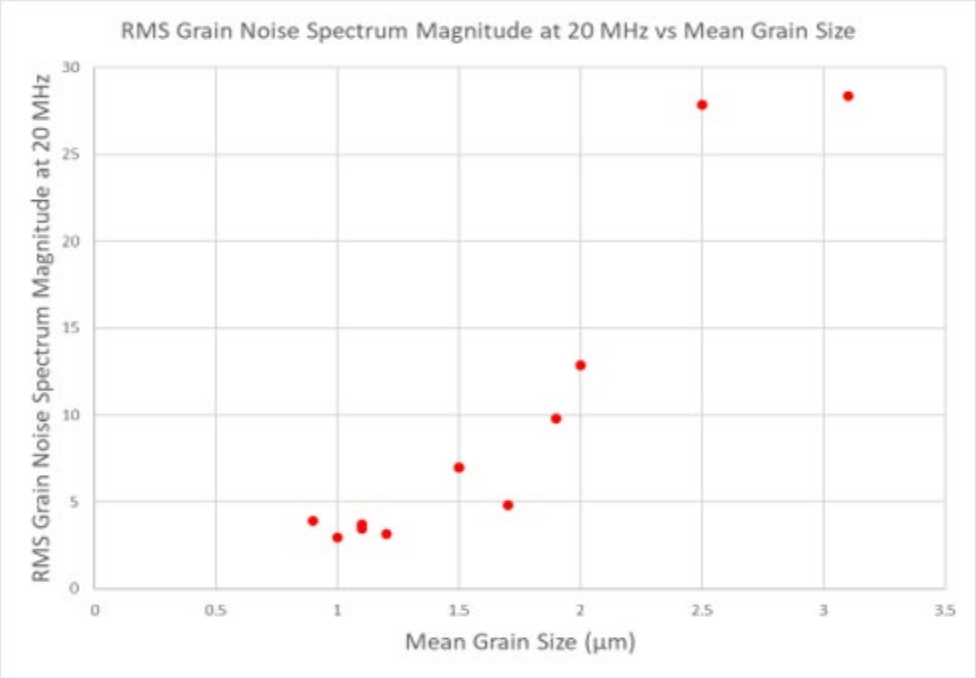

Figure 6.11. Ultrasonic noise amplitude versus micrograph-measured mean grain size.

6.5 Ultrasonic Temperature Dependence

Ultrasound in metals can have a strong temperature dependence. This can complicate some types of ultrasound analysis, but it can also be used to monitor temperature remotely and instantaneously in samples, including solid-phase process materials. In one study related to ShAPE-processed aluminum materials, longitudinal wave speed was estimated from ultrasonic measurements acquired from a 2.5 cm thick aluminum 6061 specimen over the temperature range of 23°C–400°C (Good, Forsi, and Grant 2020). A decreasing linear relation was observed in the data with a slope of -0.0011 mm/(µs °C) and a linear regression R2 value of 0.992 (Figure 6.12). The good fit to a linear function inferred an inverse relation that might be used to estimate temperature by a measurement of longitudinal wave speed.

Ultrasonic data was acquired with lead metaniobate elements attached to the aluminum specimen. Each of the two elements had a 3.1-mm diameter and a 15-MHz resonance frequency. Pulse-echo and through-transmission techniques were used to acquire data. The piezoelectric sensors became dysfunctional above 400°C as they approached the Curie temperature of 460°C for lead metaniobate (K-81) (Piezoelectric_Technologies 2022). The specimen configuration was selected to replicate a typical displacement between the ShAPE container and mandrel (Whalen et al. 2017) and interrogation of a material region adjacent to the extrusion die where heat is generated by SPP. Future work should examine the following:

- Higher temperature piezoelectric material such as a modified bismuth titanate that has a Curie temperature of 770°C (Meggitt plc n.d.)
- Other wave modes, such as shear waves and surface waves, to examine acoustic parameters that may have potential for feedback control
- Techniques to interrogate selected material regions of interest

- Repeat measurements since only one data acquisition pass with increasing temperature was acquired
- ShAPE implementation will naturally require ultrasonic techniques that couple ultrasound with high-temperature, rotating billet material. One candidate is EMATs that can be configured for high temperatures. The advantages of EMATs are the passage of ultrasound directly into and out of the high-temperature billet material and the elimination of additional couplant material typically used by piezoelectric sensors.

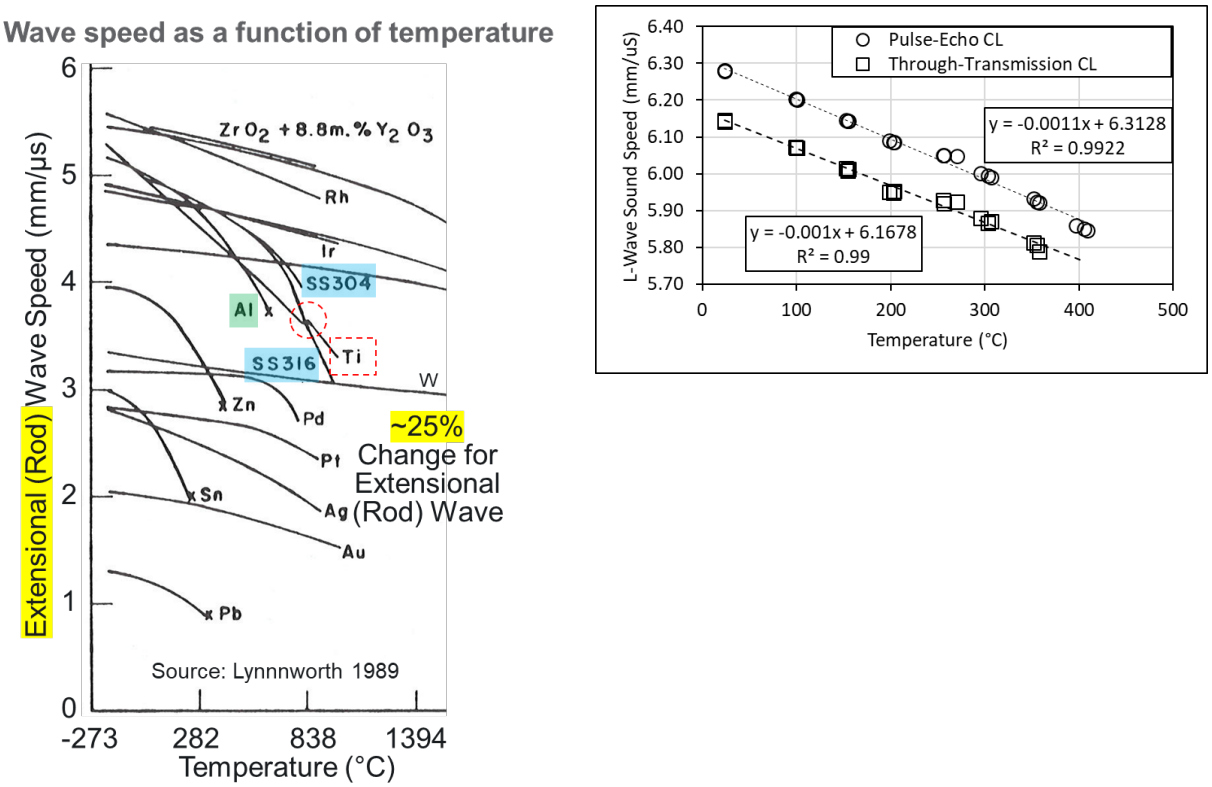

Figure 6.12. PNNL study to estimate the internal temperature of Al. Source: (Good, Forsi, and Grant 2020)

6.6 Laser UT

One implementation of non-contact UT can use lasers to generate and detect ultrasonic waves (Taheri et al. 2019). This inspection method can be used for a wide bandwidth of frequencies, up to 15 MHz. There are multiple setups for these systems, and a typical layout of a laser ultrasound inspection configuration can be seen in Figure 6.13. The laser UT system employs a pulsed laser for generating ultrasonic waves and a continuous laser or a long-pulsed laser coupled to an interferometer for detection, measuring surface displacements on the target surface. Two intensity levels exist for generating the pulse. At low power, the illuminated spot undergoes rapid thermal expansion to generate the pulse. At high power, a few angstroms of material are ablated from the material surface, and the resulting rebound from the plasma generates the pulse.

Laser UT has the advantages of high sensitivity without using fluid couplant (dry couplant) and compatibility with complex shapes, moving surfaces, and high-temperature surfaces that are favorable for in-line inspection. For FSP applications, the laser excitation and sensing can be aimed just behind the weld or on either side of the weld for almost real-time sensing of weld anomalies and weld quality. Laser-generated ultrasonic waves can induce various wave types, including surface waves that may be primarily sensitive to surface anomalies plus shear and longitudinal waves that can penetrate the weld volume, and if any anomalies reflect the ultrasound back to the surface, which can be indicative of the anomalies.

One alternate laser ultrasound configuration is a hybrid that uses a piezoelectric or EMAT to excite the ultrasonic wave and the Class 2 laser to sense the surface wave motion. This is a laser-safe implementation approach since Class 2 lasers are relatively weak and normally would not harm an eye unless a person deliberately stared into the beam. The advantages of having all the instrumentation remote from the heat and mechanical FSP mechanism are still present for the detection laser but are problematic for the excitation source unless the optics can be kept clean.

A special case of laser ultrasound is implemented with a solid-state fiber-coupled laser at visible and near-infrared operating wavelengths (532–1064 nm) that allow for much smaller probe heads and eliminate the need for complex optics (Brauns et al. 2021). This essentially forms an air-coupled ultrasound sensor that can have similar performance to fluid-coupled ultrasound sensors. The system can be configured as a sensor array or with separation between the transmit and receive systems, allowing a wide range of wave modes and detection configurations.

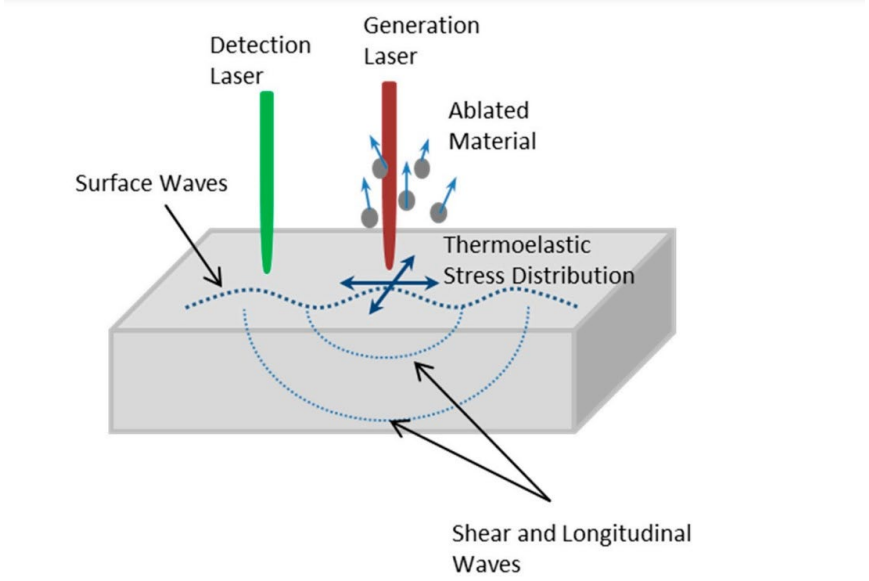

Figure 6.13. Setup for laser waveform generation and detection.

6.7 Acoustic Emission

Acoustic emission (AE) testing works by sensing a stress wave produced in a sample. Wave initiation is normally due to inter-granular bonds breaking as a result of stress, which may occur when a component is mechanically or thermally loaded and cracks grow. The stress wave can also be caused during an FSP. Sensing can use piezoelectric sensors acoustically coupled to

the weld sample either with ultrasound fluid couplant or with mechanical pressure to allow the wave to pass through the sensor, or a non-contact sensor like an EMAT or a laser sensor to monitor and detect the presence, absence, or acoustic intensity of the stress waves. For most metals, these stress waves travel tens of centimeters or further, so relatively few sensors can be used to monitor AE events. In one study, (Senthilkumar et al. 2013) used an AE sensor mounted on samples as shown in Figure 6.14 to correlate tensile strength with AE amplitudes. Test conditions included a round spindle, a square spindle, and a triangular spindle. Although there was some spread in the data and these three FSP conditions were significantly different, there was a general grouping of the three test conditions, indicating a correlation between AE and tensile strength for the three test conditions (Figure 6.15).

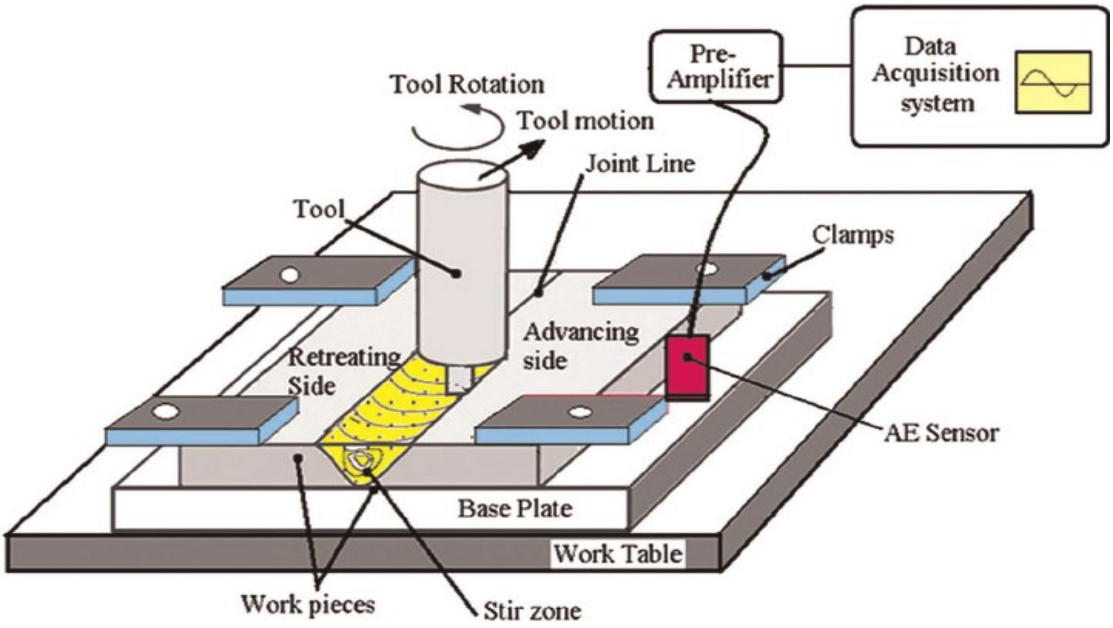

Figure 6.14. Test setup for AE monitoring of FSP.

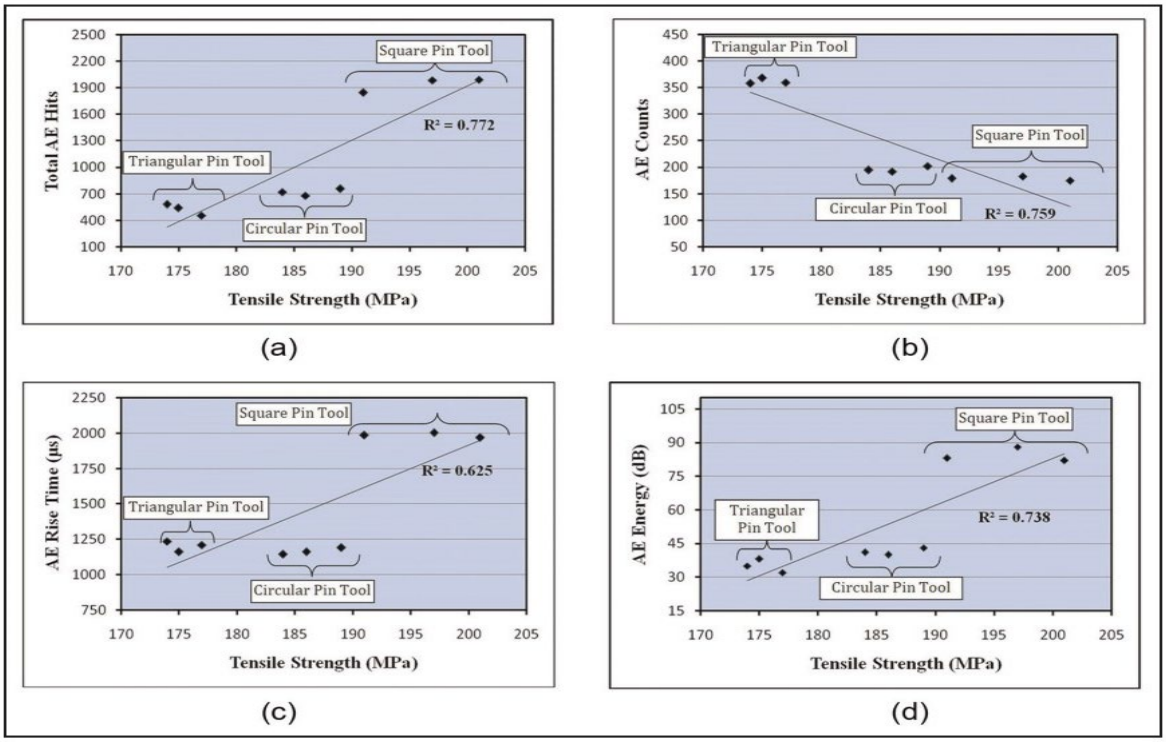

Figure 6.15. Relationship between AE parameters with tensile strength of FSP specimens produced by different tool pin profiles: (a) AE hits versus tensile strength, (b) AE average counts versus tensile strength, (c) AE rise time versus tensile strength, and (d) AE energy versus tensile strength.

6.8 Resistivity/Conductivity: 4-pt Potential Drop

The electrical resistivity or conductivity of materials depends on the electron mobility, which is influenced by: crystalline structure, crystal defects (i.e., point defects such as voids and interstitials); linear dislocations; surface defects (as twins and grain boundaries); plus grain size, and therefore can be useful as an indicator of material properties, including those of solid-state materials like FSPs. Moreover, electrical conductivity can be measured directly and nondestructively.

The electrical conductivity (σ) [Siemens/meter or S/m] measures the material's ability to conduct an electric current, since at a microscopic level, the electric current is related to the movement of electrons through a material (Santos 2014). It is the reciprocal of electrical resistivity, (ρ) [Ω·m], according to the equation $\sigma = 1/\rho$ and is commonly expressed as %IACS, which is the acronym for International Annealed Copper Standard, corresponding to the electrical conductivity measurement as a percentage of the conductivity of pure copper at 25°C. So, an electrical conductivity of 100 percent IACS is equivalent to 5.8 × 107 S/m.

The resistivity or conductivity of a material can vary greatly with temperature. The resistivity of metals usually increases as temperature (T) increases, in an approximately linear relationship. The temperature dependence of the resistivity, ρ(T), can, therefore, be expressed as:

$$\rho T = \rho 0 + \rho 0 \alpha T - T0 \qquad \text{Equation 6.1}$$

where T0 is the reference temperature, $\rho 0$ is the intrinsic resistivity at T0, depending on the electron scattering in the crystal structure of the material, and α is the temperature coefficient of resistivity, which depends only on the material being considered. The temperature-dependent term is the contribution of resistivity caused by the scattering of electrons by phonons in the material. So, the conductivity decreases with temperature, according to Equation 6.2, where $\sigma 0$ is the intrinsic or temperature-independent term inherent to the material itself. Figure 6.16 illustrates the decrease in conductivity of the aluminum alloy AA1100 with temperature.

$$\sigma = \sigma 01 + \alpha T - T0 \qquad \text{Equation 6.2}$$

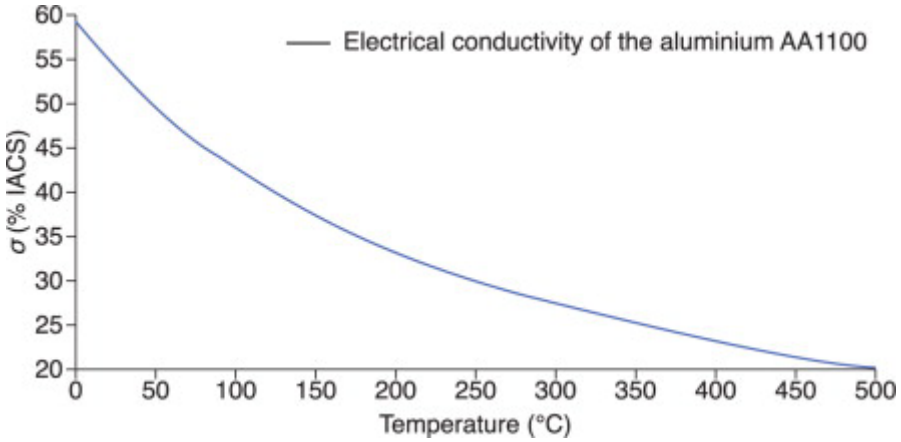

Figure 6.16. Decrease of electric conductivity of the AA1100 with temperature.

Electrical resistivity or conductivity can also be simply measured with a two-point probe or a 4-point probe. With a 2-point probe, there is a degree of uncertainty associated with the resistance of the cables and cable contact resistance. This is substantially mitigated by the 4-point measurement approach. The calculation of the resistivity of a material is substantially governed by Ohm's law, but the distribution of the current in a sheet or plate is a function of the probe spacing and the material thickness. Correction factors and calculators for this can be found in (Honsberg and Bowden 2022). For a wire or rod, the calculation is more straightforward, as shown in Figure 6.17.

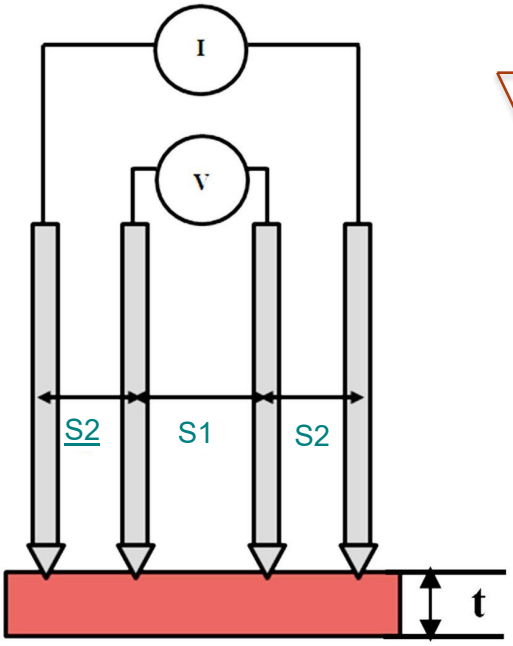

4-pt plate measurement:

V = I * R where

ρ = resistivity (Ωcm)
R = ρ * k = sample resistance (Ω)
k = correction factor which is a function of t and S (see reference)
S1 & S2 = spacing of probes,
t = sample thickness

2-Point plate measurement:
S2 = 0 (injection and measurement are on same electrode

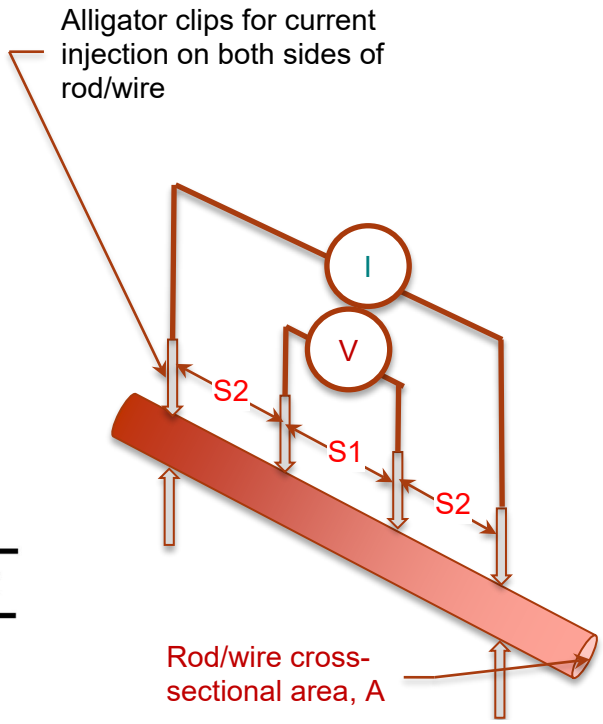

4-pt rod/wire measurement:

R = V/I = ρ*S1/A

where:
P = Resistivity of the material, in Ω.m
S1 = Measurement pin separation, meter
A = Cross sectional rod area in

Figure 6.17. (left) 2-point and 4-point potential drop measurements are based on a correction factor related to S2 and t. (right) wire/rod resistivity is measured directly and relies on S2 being large enough so that current (I) distributes uniformly through rod area (A).

6.9 Electromagnetic / Eddy Current

Eddy current inspections measure the electromagnetic and conductive material properties of metals by sensing changes in the eddy current coil's complex impedance as induced eddy currents in the part interact with changes in the conductivity and magnetic permittivity of material in close proximity to the coil (Figure 6.18)(Glass et al. 2018). A number of coil configurations are possible, including single coil, differential pairs, reflectance coil pairs, dual D pairs, and multi-coil arrays (Figure 6.19). The surface area and volume of material examined are proportional to the size of the coils and are also related to the excitation frequency, but the eddy current sensor depth of sensitivity is limited to several mm below the coil contact surface. The degree of resolution can be adjusted with conductive or high-permeability shields, cups, and cores, and influences from permeability variations may be mitigated with saturation magnetic-bias fields.

Reflectance or differential pair configurations are more suitable for scanning to detect small anomalies in the material that may be different from the surrounding material. These paired sensors are also less sensitive to the liftoff distance between the coil and the material to be examined. Liftoff sensitivity is important and must be precisely controlled between the calibration and the measurement because liftoff has such a large influence on the measured impedance. Absolute coils are typically more suitable for measuring the absolute electromagnetic nature of material, such as absolute material conductivity, which can be indicative of porosity, work hardening, thermal treatment, and other material characteristics.

The basic steps of eddy current testing are quite similar, regardless of the specific coil configuration. The sensor is “zeroed” and calibrated on a standard representative of the types of defects or anomalies that are targeted with the inspection. For thermal applications or FSP-material, this could include acceptable and unacceptable quality coatings or welds. The coil or array of coils is then placed on the spot to be examined or scanned over the area to be examined, and the signal is recorded. Absolute measurements are possible relative to the “zeroed” calibration reference, but more commonly, the scan is evaluated for anomalies in the data to locate a flaw, crack, inclusion, or other anomaly for further inspection and disposition to decide if the part is acceptable or rejectable.

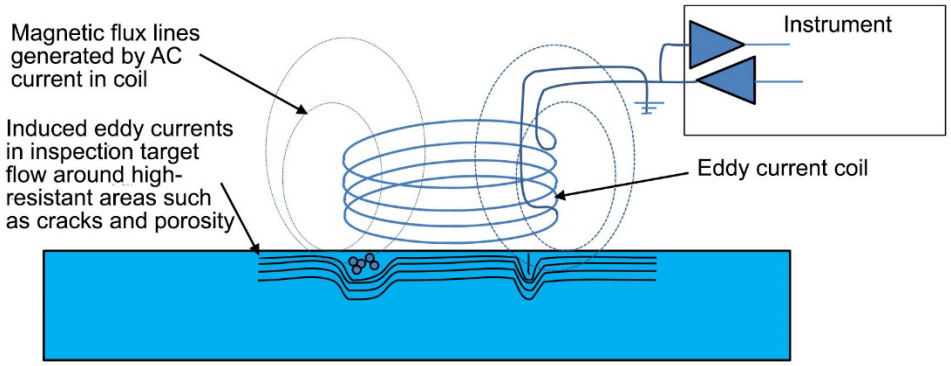

Figure 6.18. Eddy current coil sensors induce currents within conductive materials, and the coil impedance changes as a result of those eddy current behaviors can be sensed to indicate anomalies within the test material.

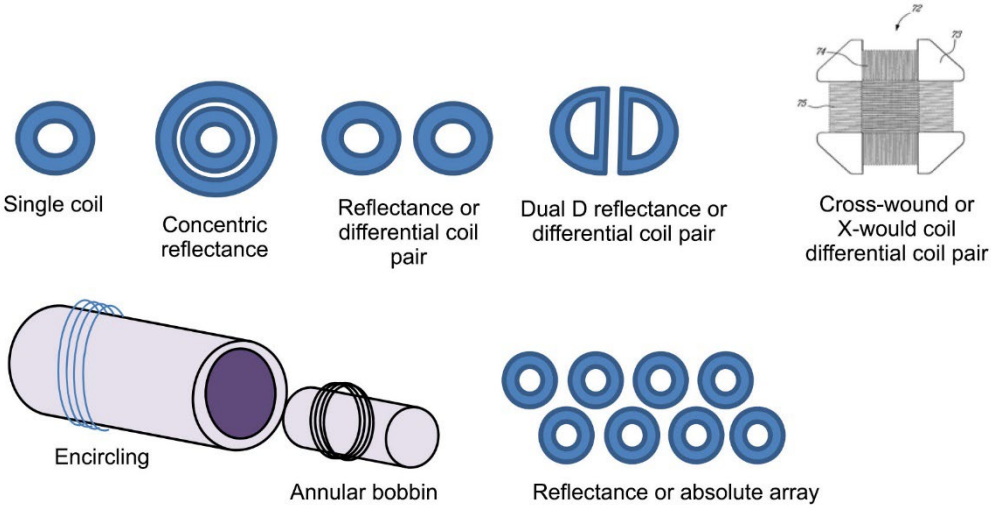

Figure 6.19. There are a large number of possible coil configurations for eddy current testing. Generally, the eddy currents flow in the same orientation as the currents within the coils, and configuration selection depends on the application and test object geometry.

Commercial eddy current companies' market-specific eddy current products for inspection of FSPs for various flaws. One example is shown in Figure 6.20, showing a 126-coil eddy current array probe designed to inspect FSPs looking for axial and transverse cracks plus grinding divots or concavities from post-welding finish grinding. The examination performance of an FSP calibration sample containing both cracks and grinding concavities is shown in Figure 6.20. The probe is passed over the FSP either manually or robotically to produce an inspection file that can be examined for the flaws of interest.

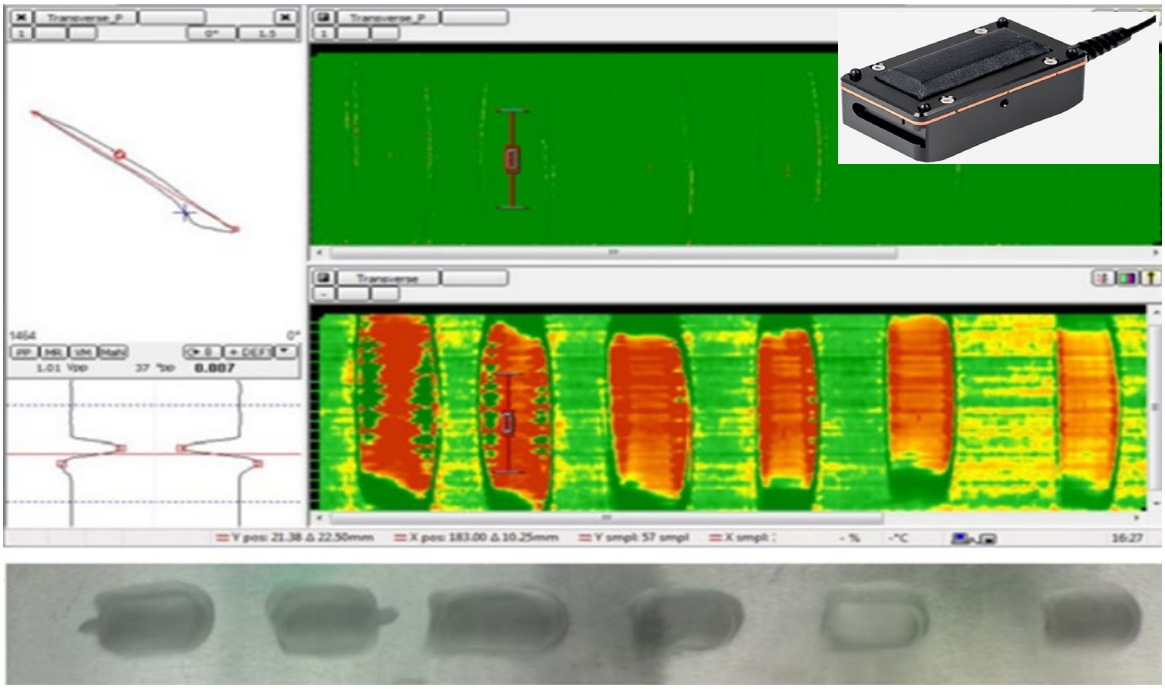

Figure 6.20. EddyFi representation of concavities and notches in FSP.

Eddy current testing responds to three fundamental parameters: material conductivity, material permeability, and probe coupling. Material conductivity is the property of interest to assess FSP quality related to variations in porosity, the presence or absence of cracks, and liftoff associated with surface geometry irregularities. Secondary effects that contribute to eddy current responses include surface roughness, cold working, changes in permeability, and other nuisance effects that have to be either suppressed or handled with signal processing.

Eddy current testing offers a range of measurements that can be applied to FSPs. Advantages and limitations are summarized in Table 6.1.

Table 6.1. Overview of eddy current technology applicability, advantages, and limitations.

	Applicability	Advantages	Limitations
Eddy Current Technology	Only sensitive to conductive media (not ceramics). Sensitive to cracks, inclusions, and porosity.	No need for fluid coupling. Manual spot readings or automated scans. Relative ease of application and cost.	Limited to near-surface measurements. Requires specific calibration standards. Sensor response varies according to flaw orientation with respect to coil orientation. This effect can be mitigated with large coil arrays.

6.10 X-ray Imaging and Computed Tomography

The principle of x-ray imaging (radiography) is that the intensity of an x-ray beam incidentally passing through an object is attenuated differently depending on the density and atomic number of the material(s) in the object. A typical radiography measurement consists of an x-ray source (an isotopic source or other radiation-generating device) and a detector (x-ray-sensitive film or a 1-D or 2-D digital detector) on either side of the object to be interrogated. X-rays from the source are attenuated by the object, and the magnitude of this attenuation is dependent upon the path length through the materials between the source and detector. A graphic representation of a radiography measurement is shown on the left side of Figure 6.21. Radiography can be considered a shadow-casting process; higher density materials and higher atomic number (Z) materials will attenuate (absorb or scatter) more x-rays, and thus the region on the detector behind these materials will appear darker than regions behind lower density or lower Z materials. X-ray radiography is a well-established NDE technique used, for instance, to verify the integrity of welds or for quality assurance of machined parts.

An ambiguity in radiography is that the image is a 2-D projection of an inherently 3-D object. Information about depth—whether a feature is behind or in front of another feature—is often inaccessible in a radiograph. This may not be a constraint; testing the integrity of a weld may depend upon the detection of a void in the weld, but the precise location of that void may not be as important. In other applications, such as metrology or the characterization of the void space in a porous sample, 3-D information is required. Transmission computed tomography (CT) is the process of acquiring multiple radiographs of an object from different perspectives and mathematically inverting these data to produce a 3-D volume describing the 3-D distribution of material in the object. A CT system includes the components of a radiography capability with the addition of manipulation hardware to either rotate the detector and source around the object or,

more often, rotate (and sometimes translate) the object between the source and detector. A tomography capability includes a radiography capability by definition.

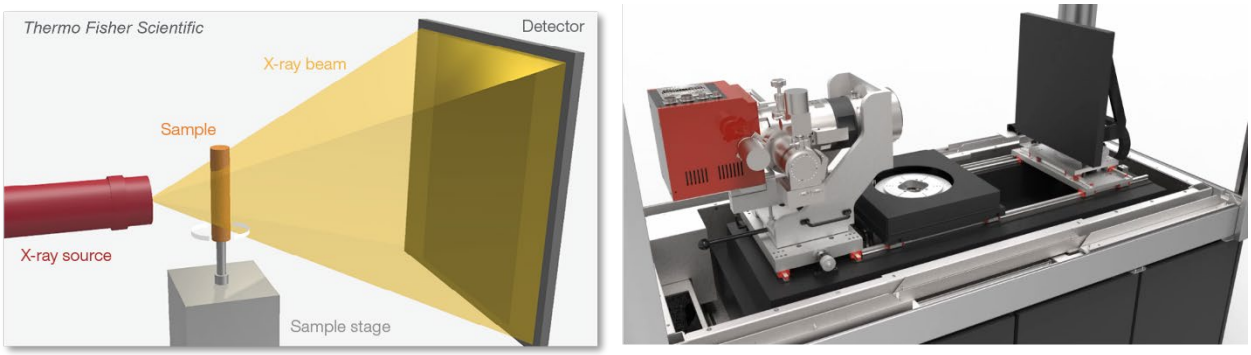

Figure 6.21. A graphic of an x-ray imaging system showing the principal components: the x-ray source on the left, imaging detector on the far right, and the object under interrogation between the source and detector. The shadow on the detector is representative of a single radiograph. A set of radiographs collected as the object is rotated are the tomographic data that can be reconstructed to obtain a 3-D representation of the material inside the object. On the right is an example of laboratory equipment used to collect tomographic data.

Tomographic systems are often referred to by the length scale describing the highest resolution achievable on the system—micro-CT or nano-CT, for example. The majority of laboratory-scale CT systems use geometrical magnification: the object is placed near the vertex of a cone (or fan) of radiation, and object features are magnified onto the detector. Thus, a constraint on the projection resolution is the size of the focal spot, much as the diameter of the pinhole in a pinhole camera defines the sharpness of the image[2]. This also introduces a trade-off between the lateral extent of the object and the amount of magnification, leading to a general rule of thumb regarding spatial resolution: the diameter of the object is about 10^3 times the desired spatial resolution. So, while it may be desirable to resolve micron-sized defects in meter-sized parts, achieving μm spatial resolution requires parts that are only a few mm in diameter.

Often, there is a need to correlate features across length scales or identify additional features at lower length scales. An illustration of this type of analysis is shown in Figure 6.22, where the left side shows a volume rendering of CT data from an approximately 10 cm object—a geological specimen with uraninite deposits. The spatial resolution of these data is a few millimeters. The uraninite has a higher Z than the rock matrix and can be easily segmented for visualization or to determine a region from which to extract a sample section for examination at a higher spatial resolution. An example is shown in the second image from the left. This is a rendered region of a different object (gold particles in an epoxy matrix), but it exemplifies the process of interrogating a smaller version of a large sample with a resolution of a few microns. And this process can be repeated using a correlative sample holder to transfer the mm-sized object to a focused ion beam for extraction of a smaller region to be interrogated at the nm scale or examined with an SEM. This workflow moves pretty quickly out of the NDE realm when small sections are cored out of larger parts, and one objective for materials characterization is to be able to confidently correlate signatures that are accessible at a longer length scale to features of the object at a shorter length scale.

[2] There are additional constraints, such as the pixel dimension on the detector and the number of angular samples. But a high-resolution CT system is often built around the size of the focal spot.

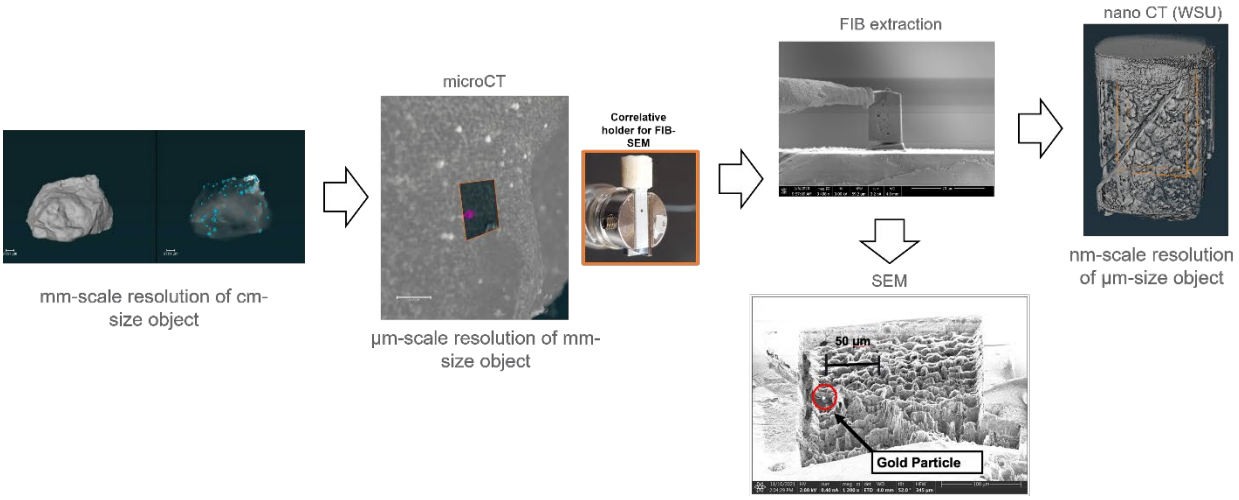

Figure 6.22. Tomography and destructive evaluation across length scales. Progressing from left to right, CT data are displayed at mm, µm, and nm length scales (albeit for different objects). Additional tools, such as a focused ion beam for extraction of small regions and SEM, provide additional material-characterization information.

There are myriad additional examples of tomography applications in material characterization. Kar et al. (Kar, Suwas, and Kailas 2018) demonstrated spatial variation in particle size distributions (10 µm and larger) in FSP joining of aluminum and titanium alloys and how the distribution homogenized after a second pass with the tool. These results were correlated with microstructure characterization with SEM. At a longer length scale (approximately 100 µm), Pandya, Mishra, and Arora (2019) studied material flow and channel formation in friction stir channeling of aluminum alloys and could clearly identify five material regions, including differences between the advancing and retreating sides of the tool. FSP of aluminum alloy to steel has been studied with nano-CT by Liu et al. (2018), in which they have studied welding conditions (e.g., tool size, tool offset, rotation speed, weld speed) and material distribution. A PNNL example of the tomography of an FSP in aluminum is shown in Figure 6.23. These images show cross sections in three orthogonal directions of three aluminum slabs welded together. Large void regions are clearly visible. In the z-y plane (middle image), voids in the trailing side of the weld and in the arcs show the direction of the tool. Note that the voids are not visible on the surface of the plates (except at the tool removal location).

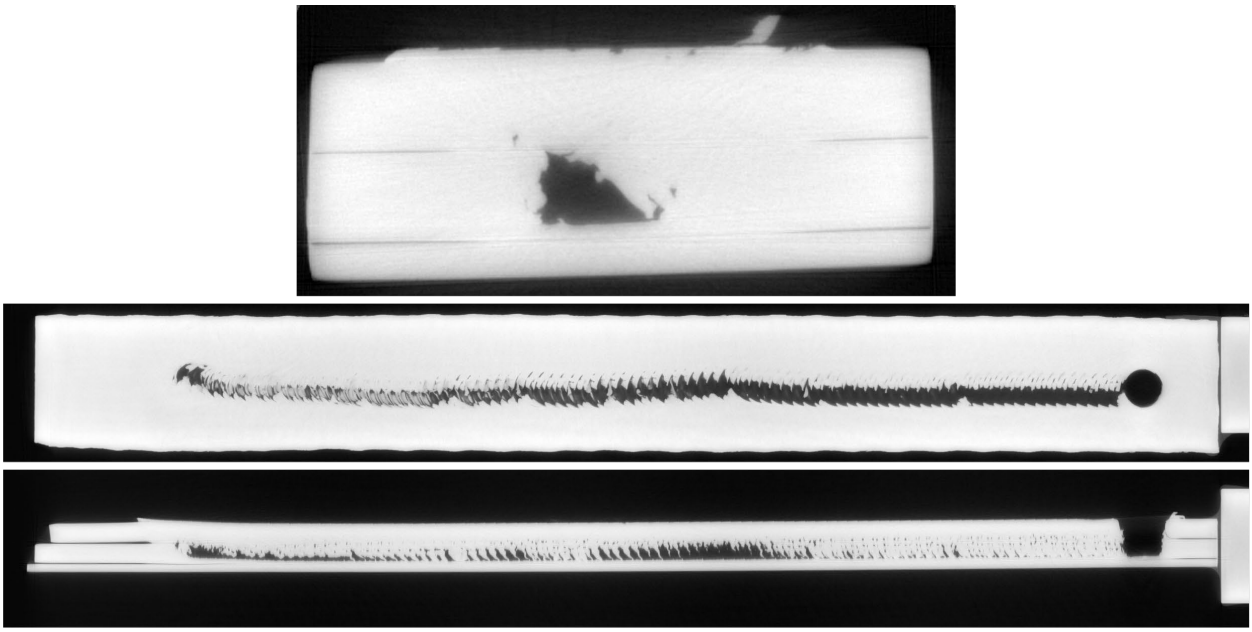

Figure 6.23. Three orthogonal cross sections from a CT scan of three aluminum plates. The top image is an xy plane, the middle is a zx plane, and the bottom is a zy plane. The object is about 17 mm wide (x dimension), 7 mm thick (y), and 200 mm long (z). Welding proceeded from left to right, and the tool removal location can be seen on the right side of the bottom two images.

6.11 Additional Radiography and CT Material Signatures

While the principal signatures available to x-ray NDE are the density and atomic number of the materials being interrogated, there are additional signatures that can be exploited in both radiography and CT experiments to provide additional discrimination. A first example, differential phase contrast (DPC) imaging, is a technique initially developed at beam lines that is sensitive to small-angle scattering and allows access to object texture that is below the resolution limit of the system (Miller et al. 2013). In the DPC method, the x-ray beam is spatially modulated, most often with a partially attenuating parallel-line grating. The patterned beam is incident on the object, and small deviations in the pattern attributable to small-angle scattering, are detected and subsequently processed. This allows sensitivity to features that are below the spatial resolution limit of the system. An example experimental setup is shown in Figure 6.24. The imaging geometry consists of the nominal x-ray source and detector, as well as patterned optics that spatially modulate the intensity of the beam. Imaging and analysis of deviations from these patterns as the x-rays propagate to the detector allow detection of features below the spatial resolution of the system.

The ability to detect grain-size differences below the resolution limit of a CT system has been demonstrated by Schaff et al. (2017) for FSP of Al-Cu and Al-Mg alloys. The changes in grain structure at the TMAZ are detectable, though not resolved, in the dark-field image, as shown in Figure 6.25. This is a bulk (3-D) measurement, so even though the grain structure is not resolved, other features such as voids or inclusions can be detected and often resolved.

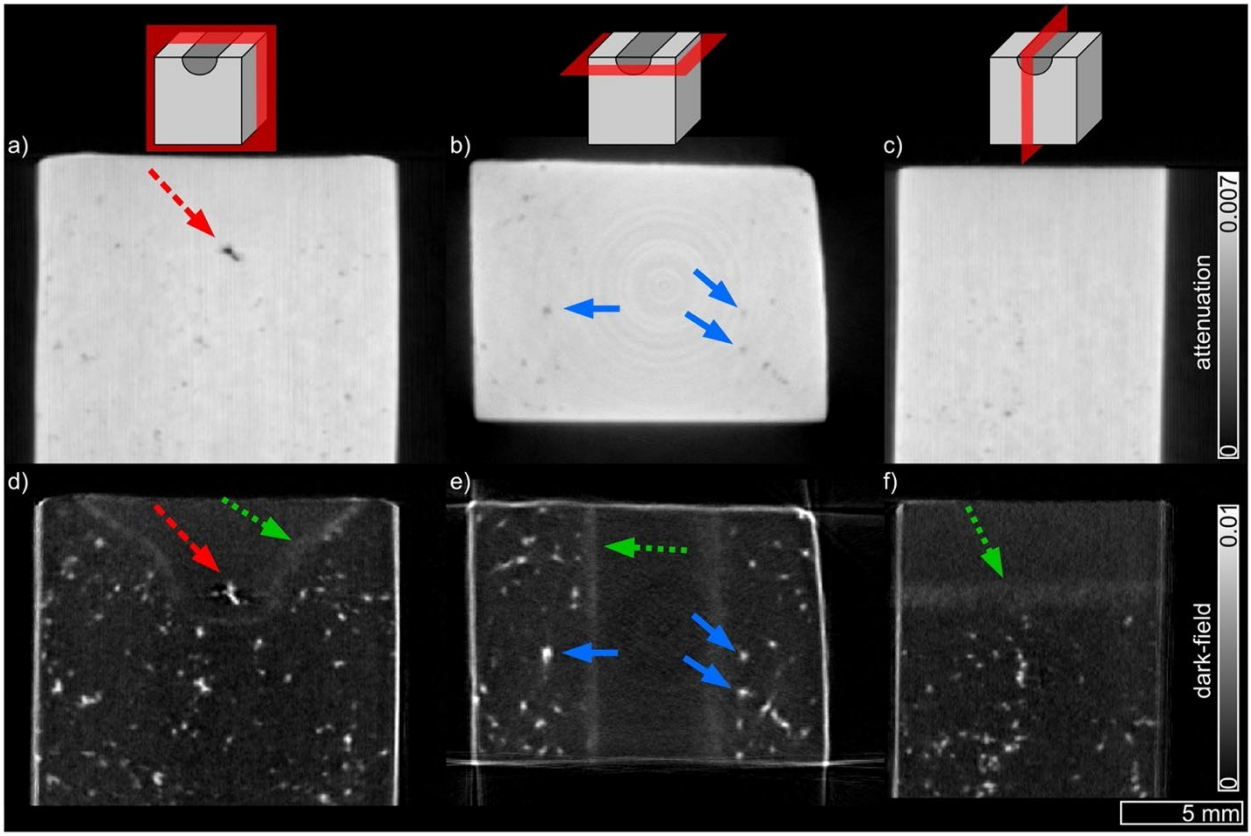

Figure 6.24. Orthogonal slices form a 3-D CT reconstruction of phase-contrast data of an FSP of a cast-aluminum block (AlSi7Mg0,3 alloy). The red line in the top row indicates the direction of the slice for each column. Voids (red arrows) and inclusions (blue arrows) are observed in both the attenuation images (middle row) and dark-field reconstruction (bottom row). The boundaries of the weld nugget, indicative of a grain-size change below the reconstructed resolution, are seen in the dark-field slices (green arrows). (Schaff et al. 2017).

Researchers at the Technical University of Munich (Schaff et al. 2017) have demonstrated the ability to detect grain phase contrast imaging on FSP samples, grainsize, TMAZ, different zones, and inclusions all in one shot.

Features of the x-ray interaction cross sections can be exploited in order to improve the ability to discriminate between materials. The dual-energy imaging technique (Alvarez and Macovski 1976) processes data from two x-ray endpoint energies and produces images that disambiguate density and atomic number effects. This approach is commonly used, for example, to discriminate explosive material in baggage-screening systems (Runkle, Chichester, and Thompson 2012). This technique can be extended, as shown in Figure 6.25, to exploit discontinuities in the attenuation coefficient. As shown in the plot on the left of the figure, uranium has a step-like increase in the attenuation coefficient above 100 keV, a region of the energy spectrum where lower-Z materials have more slowly varying changes in attenuation. Collecting two sets of image data—one just below the discontinuity and one just above—allows discrimination between uranium in a sample and other materials. Conversely, using a broad energy spectrum and processing data from a spectrally sensitive detector can allow for discrimination as well, as shown in the two images in Figure 6.25 in which the distribution of uranium and oxygen in a UO_2 sample is mapped (Gillis et al. 2020). The work by Kar et al. (Kar,

Suwas, and Kailas 2018) relied on gray-level differences in the reconstructed data to discriminate materials. Extending the CT measurement to include spectral analysis allows for finer discrimination between materials. This type of analysis can be extended to a tomography measurement, allowing the discrimination of materials in a 3-D sample.

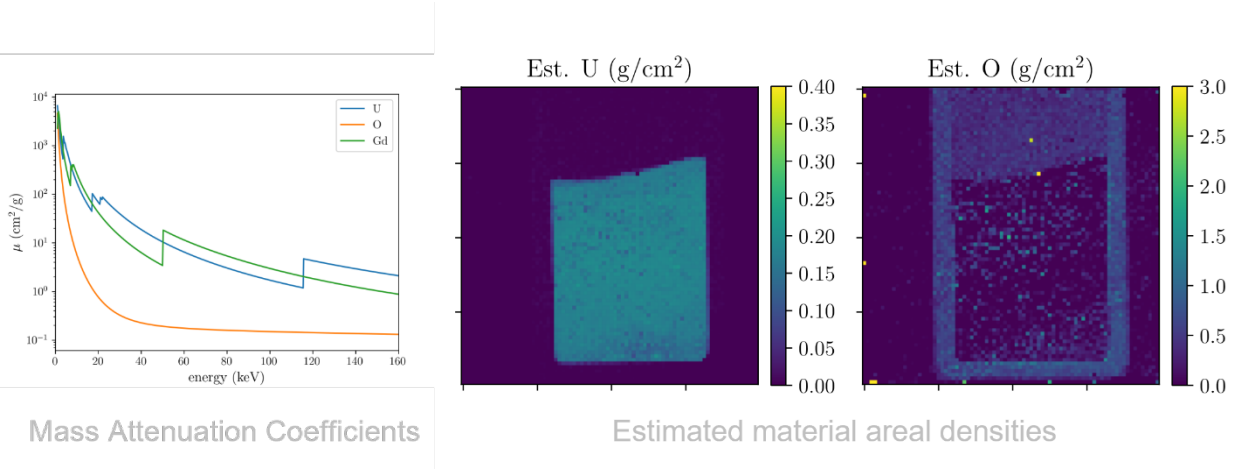

Figure 6.25. Spectral-imaging example: The attenuation coefficient of uranium has a discontinuity at the k edge just below 120 keV. An imaging system with a spectral capability and a tunable x-ray source can be used to identify material composition, in this case to map the spatial distribution of uranium and oxygen in a radiograph.

Researchers are actively investigating experimental methods, data preprocessing, reconstruction, and image analysis to improve the capabilities of turnkey radiography and CT systems in order to better meet mission needs. We are investing in new methods of radiography and tomography for enhanced materials analysis and discovery in order to characterize material properties across centimeter to sub-nanometer length scales, provide unambiguous detection and discrimination of contraband material, and develop modern nuclear-material verification capabilities for the next decade and beyond.

7.0 Observations and Conclusion

Both destructive and nondestructive evaluation testing methods have been reviewed in the context of performing material characterization of FSP and ShAPE derived materials. An emphasis of this review was towards characterization methods related to mechanical strength that can only be directly measured by destructive sample tests. Related indirect destructive and nondestructive methods, however, can be used to infer and predict mechanical strength and related material characteristics.

Some methods, like optical and electron beam microscopy, hardness tests, and, in many cases, CT scans, require samples to be prepared such that they cannot be used in service. Although the test may be nondestructive, the preparation makes the test effectively destructive. Micrographs and CT scans, however, can detect and characterize cracks, voids, grain size and distribution, contaminate inclusions, and other issues that can relate back to mechanical strength. Hardness tests are directly related to elastic and plastic material strength and, if performed on representative samples, can predict the performance of in-service material. Nondestructive methods like electrical conductivity, eddy current, ultrasound, x-ray and CT, and monitoring/controlling tool and process parameters of the FSP or SHAPE material can provide information on material to be used in service.

Additionally:

- Optical and electron microscope images of FSP materials show grain structure that can generally be correlated with mechanical strength.
- Ultrasound techniques can characterize grain size and be correlated to Young's modulus.
- The temperature of the SSP is important for the material's quality. Temperature is commonly measured within FSP and ShAPE mandrils and spindles. Ultrasound is also identified as a candidate method to measure the instantaneous sample average temperature along the ultrasound path, which could include the region just behind the SSP.
- Ultrasound methods generally require fluid coupling between the sample and the transducer. Certain less common ultrasound methods, like EMAT and laser UT, can relate to traditional ultrasound measurements without the fluid coupling burden.
- AE methods have been used to monitor samples subjected to substantially different spindles for Al FSP. The AE signals were successfully correlated with tensile strength, although it is noted that different spindles constitute a significant change to the FSP.
- Electromagnetic methods (conductivity or eddy current) measure conductivity and can be sensitive to cracks or flaws in the material. Electromagnetic methods, however, are substantially restricted to the near-surface (<1 mm).

8.0 References

Alvarez, R.E. and A. Macovski. 1976. "Energy-selective reconstructions in X-ray computerized tomography." *Phys Med Biol* 21(5):733-44. doi: 10.1088/0031-9155/21/5/002.

ASTM. 2017. ASTM E92-17 Standard Test Methods for Vickers Hardness and Knoop Hardness of Metallic Materials.

ASTM E8 / E8M-16a. 2016. Standard Test Methods for Tension Testing of Metallic Materials. In *ASTM E8 / E8M-16a*. ASTM International, West Conshohocken, PA: ASTM International.

Badidi Bouda, A., A. Benchaala, and K. Alem. 2000. "Ultrasonic characterization of materials hardness." *Ultrasonics* 38(1):224-227. doi: https://doi.org/10.1016/S0041-624X(99)00081-5.

Badidi Bouda, A., S. Lebaili, and A. Benchaala. 2003. "Grain size influence on ultrasonic velocities and attenuation." *NDT & E International* 36(1):1-5. doi: https://doi.org/10.1016/S0963-8695(02)00043-9.

Biswas, K., M.S. Good, K.C. Roberts, M.A. Subramanian, and T.J. Hendricks. 2011. "Thermoelectric and structural properties of high-performance In-based skutterudites for high-temperature energy recovery." *Journal of Material Research* 26(15):1827 - 1835. doi: 10.1557/jmr.2011.163.

Biswas, K., M.A. Subramanian, M.S. Good, K.C. Roberts, and T.J. Hendricks. 2012. "Thermal Cycling Effects on the Thermoelectric Propertiesof n-Type In,Ce-Based Skutterudite Compounds." *Journal of Electronic Materials* 41(6):1615-1621. doi: 10.1007/s11664-012-1975-z.

Brauns, M., F. Lucking, B. Fischer, C. Thomson, and I. Ivakhnenko. 2021. "Laser-Excited Acoustics for Contact-Free Inspection of Aerospace COmposites." *Materials Evaluation* (1).

Bruker. 2022. "SEM vs. TEM." https://www.technologynetworks.com/analysis/articles/sem-vs-tem-331262.

Bussu, G. and P.E. Irving. 2003a. "The role of residual stress and heat affected zone properties on fatigue crack propagation in friction stir welded 2024-T351 aluminium joints." *International Journal of Fatigue* 25(1):77-88. doi: https://doi.org/10.1016/S0142-1123(02)00038-5.

Bussu, G. and P.E. Irving. 2003b. "The role of residual stress and heat affected zone properties on fatigue crack propagation in friction stir welded 2024-T351 aluminium joints." *International Journal of Fatigue* 25:77-88.

Cannell, G., G. Grant, and T. Adams. 2015. "Demonstration of Friction Stir Welding (FSW) Technology for Packaging of Used Nuclear Fuel." Waste Management Symposium, Phoenix, AZ, March 15-19, 2015.

Carreon, M., G. Barrera Cardiel, C. Natividad, M. Salazar, and A. Contreras. 2015. "Relation between hardness and ultrasonic velocity on pipeline steel welded joints." *Nondestructive Testing and Evaluation* 31:1-12. doi: 10.1080/10589759.2015.1074231.

Choi, S., J. Ryu, J.-S. Kim, and J. Kyung-Young. 2019. "Comparison of Linear and Nonlinear Ultrasonic Parameters in Characterizing Grain Size and Mechanical Properties of 304L Stainless Steel." *Metals* 9(12):1279. doi: https://doi.org/10.3390/met9121279.

Costa, J.D., J.A.M. Ferreira, and L.P. Borrego. 2011. "Influence of spectrum loading on fatigue resistance of AA6082 friction stir welds." *International Journal of Structural Integrity* 2(2):122-134. doi: 10.1108/17579861111135888.

Delrue, S., M. Tabatabaeipour, J. Hettler, and K. Van Den Abeele. 2016. "Applying a nonlinear, pitch-catch, ultrasonic technique for the detection of kissing bonds in friction stir welds." *Ultrasonics* 68:71-79. doi: https://doi.org/10.1016/j.ultras.2016.02.012.

Elatharasan, G., and V.S. Kumar Senthil. 2012. "Modelling and Optimization of Friction Stir Welding Parameters for Dissimilar Aluminium Alloys Using RSM." *Procedia Engineering* 38:3477-3481. doi: https://doi.org/10.1016/j.proeng.2012.06.401.

Geelhood, K.J., C.E. Beyer, and W.G. Luscher. 2008. PNNL Stress/Strain Correlation for Zircaloy.

Ghorbanzade, T., A.R. Soltanipour, K. Dehghani, and A. Chabok. 2014. "Microstructural evolutions and mechanical properties of friction stir welded AA2024-3." *Proceedings of the Institution of Mechanical Engineers, Part L: Journal of Materials: Design and Applications* 230(1):75-87. doi: 10.1177/1464420714545369.

Gillis, W.C., A.J. Gilbert, K. Pazdernik, and A. Erickson. 2020. "A Partial-Volume Correction for Quantitative Spectral X-Ray Radiography." *IEEE Transactions on Nuclear Science* 67(11):2321-2328. doi: 10.1109/TNS.2020.3028009.

Glass, S.W., M.R. Larche, M.S. Prowant, J.D. Suter, J.P. Lareau, X. Jiang, and K.A. Ross. 2018. "Cold spray NDE for porosity and other process anomalies." *AIP Conference Proceedings* 1949(1):020010. doi: 10.1063/1.5031507.

Goebbels, K. 1980. "Structure analysis by scattered ultrasonic radiation." *Research Technology in NDT* 4:87-157.

Good, M.S, E. Forsi, and G.J. Grant. 2020. *Sound Speed as a Candidate for Internal Temperature Monitoring During Solid Phase Processing of Materials*. PNNL SA-156914, Pacific Northwest National Laboratory, Richland, WA.

Good, M.S. and J.L. Rose. 1984. "Measurement of Thin Case Depth in Hardened Steel by Ultrasonic Pulse-Echo Angulation Techniques." In *Nondestructive Methods for Material Property Determination*, edited by Clay Olaf Ruud and Robert E. Green, 189-203. Boston, MA: Springer US.

Guo, Y. and D.R. Todd. 2022. A*gile MCPC Specimens Characterization with NDE Method*. PNNL-SA-179036, Pacific Northwest National Laboratory. Richland, WA.

Gupta, R.K. and N. Birbilis. 2015. "The influence of nanocrystalline structure and processing route on corrosion of stainless steel: A review." *Corrosion Science* 92:1-15. doi: https://doi.org/10.1016/j.corsci.2014.11.041.

Harrison, R.P. 2007. "Neutron-based techniques for application to advanced energy systems materials research and development." Characterization and Testing of Materials for Nuclear Reactors, Proceedings of a technical meeting, IAEA, Vienna.

Hefferan, C.M. 2020. "The Characterization Advantage of Electron Backscatter Diffraction (EBSD) Microscopy." R.J. Lee Group.

Honsberg, C. and S. Bowden. 2022. "Four Point Probe Resistivity Calculator." https://www.pveducation.org/calculators/four_point_probe_resistance.

Kadlec, M., R. Růžek, and L. Nováková. 2015. "Mechanical behaviour of AA 7475 friction stir welds with the kissing bond defect." *International Journal of Fatigue* 74:7-19. doi: https://doi.org/10.1016/j.ijfatigue.2014.12.011.

Kah, P., R. Rajan, J. Martikainen, and R. Suoranta. 2015. "Investigation of weld defects in friction-stir welding and fusion welding of aluminium alloys." *International Journal of Mechanical and Materials Engineering* 10:1-10. doi:10.1186/s40712-015-0053-8.

Kahl, S. and W. Osikowicz. 2013. "Composite Aluminum-Copper Sheet Material by Friction Stir Welding and Cold Rolling." *Journal of Materials Engineering and Performance* 22. doi: 10.1007/s11665-013-0497-z.

Kar, A., S. Suwas, and S.V. Kailas. 2018. "Two-pass friction stir welding of aluminum alloy to titanium alloy: A simultaneous improvement in mechanical properties." *Materials Science and Engineering: A* 733:199-210. doi: https://doi.org/10.1016/j.msea.2018.07.057.

Khodir, S.A., T. Shibayanagi, and M. Naka. 2006. "Control of Hardness Distribution in Friction Stir Welded AA2024-T3 Aluminum Alloy." *Materials Transactions* 47:1560-1567. doi: 10.2320/matertrans.47.1560.

Kim, Y.G., H. Fujii, T. Tsumura, T. Komazaki, and K. Nakata. 2006. "Three defect types in friction stir welding of aluminum die casting alloy." *Materials Science and Engineering: A* 415(1):250-254. doi: https://doi.org/10.1016/j.msea.2005.09.072.

Korde, N. and T. Kundu. 2013. "Material hardness and ageing measurement using guided ultrasonic waves." *Ultrasonics* 53(2):506-510. doi: https://doi.org/10.1016/j.ultras.2012.09.003.

Kupperman, D.S. and K.J. Reimann. 1980. "Ultrasonic Wave Propagation and Anisotropy in Austenitic Stainless Steel Weld Metal." *IEEE Transactions on Sonics and Ultrasounics* 27(1):7-14. doi: 10.1109/T-SU.1980.31137.

Lavender, C.A., S-T Hong, M.T. Smith, R.T. Johnson, and D. Lahrman. 2008. "The effect of laser shock peening on the life and failure mode of a cold pilger die." *Journal of Materials Processing Technology* 204(1):486-491. doi: https://doi.org/10.1016/j.jmatprotec.2008.02.002.

Lemmen, H.J.K., R.C. Alderliesten, R.R.G.M. Pieters, R. Benedictus, and J.A. Pineault. 2010. "Yield Strength and Residual Stress Measurements on Friction-Stir-Welded Aluminum Alloys." *Journal of Aircraft* 47(5):1570-1583. doi: 10.2514/1.C000212.

Liu, L., H. Nakayama, S. Fukumoto, A. Yamamoto, and H. Tsubakino. 2004. "Microscopic Observations of Friction Stir Welded 6061 Aluminum Alloy." *Materials Transactions* 45:288-291.

Liu, X., S. Zhao, and J. Ni. 2018. "Material Flow Visualization of Dissimilar Friction Stir Welding Process Using Nano-CT." ASME 2018 13th International Manufacturing Science and Engineering Conference.

Long, T., W. Tang, and A.P. Reynolds. 2007. "Process Response Parameter Relationships in Aluminium Alloy Friction Stir Welds." *Science and Technology of Welding and Joining* 12(4):311-317. doi: 10.1179/174329307X197566.

Lukomski, T. and T. Stepinski. 2010. "Steel hardness evaluation based on ultrasound velocity measurements." *Insight (Northampton)* 52 (11):592-596. doi: 10.1784/insi.2010.52.11.592.

Lynnworth, L.C. 1989. *Ultrasonic Measurements for Process Control Theory, Techniques, Applications*. Waltham Mass: Panametrics Inc.

Mahoney, M., S. Sanderson, Z. Feng, R. Steel, S. Packer, and D. Fleck. 2016. "Friction Stir Welding of Pipeline Steels." In *Friction Stir Welding and Processing VII*, edited by Rajiv Mishra, Murray W. Mahoney, Yutaka Sato, Yuri Hovanski and Ravi Verma, 59-69. Cham: Springer International Publishing.

Mahoney, M.W., C.G. Rhodes, J.G. Flintoff, W.H. Bingel, and R.A. Spurling. 1998. "Properties of friction-stir-welded 7075 T651 aluminum." *Metallurgical and Materials Transactions A* 29(7):1955-1964. doi: 10.1007/s11661-998-0021-5.

Mandache, C., D. Levesque, L. Dubourg, and P. Gougeon. 2012. "Non-destructive detection of lack of penetration defects in friction stir welds." *Science and Technology of Welding and Joining* 17 (4).

McCloy, J.S., R.O. Montgomery, P. Ramuhalli, R. Meyer, S. Hu, Y. Li, C.H. Henager, and B. Jonson. 2013. *Materials Degradation and Detection (MD2): Deep Dive Final Report*. edited by Pacific Northwest National Laboratory. Richland WA.

Mężyk, J. and S. Kowieski. 2013. "The Application of Thermal Imaging Methods for Monitoring the FSW Process." 11th International Symposium on Measurement and Quality Control 2013, Cracow Poland.

Migliori, A. and J.L. Sauuro. 1997. *Resonant Ultrasound Spectroscopy: Applications to Physics, Materials Measurements, and Nondestructive Evaluation 1st Edition*. Edited by Wiley-VCH.

Miller, E.A., T.A. White, B.S. McDonald, and Seifert.A. 2013. "Phase Contrast X-Ray Imaging Signatures for Security Applications." *IEEE Transactions on Nuclear Science* 60(1):416-422.

Mishra, R.S., and Z.Y. Ma. 2005. "Friction stir welding and processing." *Materials Science and Engineering: R: Reports* 50(1):1-78. doi: https://doi.org/10.1016/j.mser.2005.07.001.

Moreira, P.M.G.P., A.M.P. de Jesus, A.S. Ribeiro, and P.M.S.T. de Castro. 2008. "Fatigue crack growth in friction stir welds of 6082-T6 and 6061-T6 aluminium alloys: A comparison." *Theoretical and Applied Fracture Mechanics* 50(2):81-91. doi: https://doi.org/10.1016/j.tafmec.2008.07.007.

Nazaeri Tiji, S., A. Asgharzadeh, T. Park, S.A. Whalen, R.E. Rabby, M. Eller, and F. Pourboghrat. 2021. "Microstructure and Mechanical Properties of the AA7075 Tube Fabricated

using Shear Assisted Processing and Extrusion (ShAPE)." *Archives of Civil and Mechanical Engineering* 21 (PNNL-SA-155953):Medium: X; Size: 44. doi: 10.1007/s43452-021-00179-6.

Oosterkamp, A., L.D. Oosterkamp, and A. Nordeide. 2004. "'Kissing Bond' Phenomena in Solid-State Welds of Aluminum Alloys." *Welding Journal* 83(8):225-231.

PNNL. n.d. Solid Phase Processing Demonstration Facility." Pacific Northwest National Laboratory, Richland, Washington. https://www.pnnl.gov/solid-phase-processing-demonstration-facility. Accessed 17 June 2024.

Pandya, S., R.S. Mishra, and A. Arora. 2019. "Channel formation during friction stir channeling process — A material flow study using X-Ray micro-computed tomography and optical microscopy." *Journal of Manufacturing Processes* 41:48-55. doi: https://doi.org/10.1016/j.jmapro.2019.03.021.

Pao, P.S., S.J. Gill, C.R. Feng, and K.K. Sankaran. 2001. "Corrosion–fatigue crack growth in friction stir welded Al 7050." *Scripta Materialia* 45(5):605-612. doi: https://doi.org/10.1016/S1359-6462(01)01070-3.

Piezoelectric_Technologies. 2022. "Advanced Piezoceramics\, Ultrasonic Transducers & Devices Materials Chart." https://piezotechnologies.com/materials-chart/.

Podržaj, P., B. Jerman, and D. Klobčar. 2015. "Welding defects at friction stir welding." *Metalurgija* 54:387-389.

Richards, D.G., P.B. Prangnell, P.J. Withers, S.W. Williams, T. Nagy, and S. Morgan. 2010. "Efficacy of active cooling for controlling residual stresses in friction stir welds." *Science and Technology of Welding and Joining* 15(2):156-165. doi: 10.1179/136217109X12590746472490.

Rosen, M., L. Ives, S. Ridder, F. Biancaniello, and R. Mehrabian. 1985. "Correlation between ultrasonic and hardness measurements in aged aluminum alloy 2024." *Materials Science and Engineering* 74(1):1-10. doi: https://doi.org/10.1016/0025-5416(85)90104-1.

Ross, K.A. 2012. *Investigation and implementation of a robust temperature control algorithm for friction stir welding*: Brigham Young University.

Ross, K.A. and M. Alabi. 2019. *Update on Investigations of Viability of Cold Spray and FSW as a Spent Nuclear Fuel Dry Storage Canister Mitigation Tool*. Pacific Northwest National Laboratory, Richland, WA.

Ross, K.A., G. Grant, J. Darsell, and D. Catalini. 2017. "Simultaneous Independent Control of Tool Axial Force and Temperature in Friction Stir Processing." In *Friction Stir Welding and Processing IX*, edited by Yuri Hovanski, Rajiv Mishra, Yutaka Sato, Piyush Upadhyay and David Yan, 269-275. Cham: Springer International Publishing.

Ross, K.A. and C. Sorensen. 2013. "Advances in Temperature Control for FSP." In *Friction Stir Welding and Processing VII*, edited by Rajiv Mishra, Murray W. Mahoney, Yutaka Sato, Yuri Hovanski and Ravi Verma, 301-310. Cham: Springer International Publishing.

Ross, K.A., B. Sutton, G. Grant, G. Cannell, G. Frederick, and R. Couch. 2017a. "Development of Friction Stir Processing for Repair of Nuclear Dry Cask Storage System Canisters." In *Friction*

Stir Welding and Processing IX, edited by Yuri Hovanski, Rajiv Mishra, Yutaka Sato, Piyush Upadhyay and David Yan, 39-46. Cham: Springer International Publishing.

Ross, K., B. Sutton, G. Grant, G. Cannell, G. Frederick, and R. Couch. 2017b. "Development of Friction Stir Processing for Repair of Nuclear Dry Cask Storage System Canisters." In *Friction Stir Welding and Processing IX*, edited by Y Hovanski, et al. 39-46. Cham:Springer International Publishing. PNNL-SA-121980. doi:10.1007/978-3-319-52383-5_5.

Runkle, Robert C., David L. Chichester, and Scott J. Thompson. 2012. "Rattling nucleons: New developments in active interrogation of special nuclear material." *Nuclear Instruments and Methods in Physics Research Section A: Accelerators, Spectrometers, Detectors and Associated Equipment* 663 (1):75-95. doi: https://doi.org/10.1016/j.nima.2011.09.052.

Ruzek, R. and M. Kadlec. 2014. "Friction Stir Welded Structures: Kissing Bond Defects." *International Journal of Terraspace Science and Engineering* 6 (2).

Senthilkumar, S., S. Narayanan, and S. Ashok. 2013. *Acoustic emission–based monitoring approach for friction stir welding of aluminum alloy AA6063-T6 with different tool pin profiles*. Proceedings of the Institution of Mechanical Engineers Part B Journal of Engineering Manufacture, 2013. 227: p. 407-416. doi: 10.1177/0954405412472673.

Sagar, S., C. Miyasaka, M. Ghosh, and B. Tittmann. 2012. "NDE of friction stir welds of Al alloys using high-frequency acoustic microscopy." *Nondestructive Testing and Evaluation - NONDESTRUCT TEST EVAL* 27:1-15. doi: 10.1080/10589759.2012.656638.

Santos, T.G. 2014. "5 - Characterization of FSP by electrical conductivity." In *Surface Modification by Solid State Processing*, edited by Rosa Miranda, 153-176. Woodhead Publishing.

Sato, Y.S., M. Urata, and H. Kokawa. 2002. "Parameters controlling microstructure and hardness during friction-stir welding of precipitation-hardenable aluminum alloy 6063." *Metallurgical and Materials Transactions A* 33(3):625-635. doi: 10.1007/s11661-002-0124-3.

Schaff, F., A. Bachmann, A. Zens, M.F. Zaeh, F. Pfeiffer, and J. Herzen. 2017. "Grating-based X-ray dark-field computed tomography for the characterization of friction stir welds: A feasibility study." *Materials Characterization* 129:143-148. doi: https://doi.org/10.1016/j.matchar.2017.04.023.

Senthilkumar, S., S. Narayanan, and S. Ashok. 2013. "Acoustic emission–based monitoring approach for friction stir welding of aluminum alloy AA6063-T6 with different tool pin profiles." *Proceedings of the Institution of Mechanical Engineers Part B Journal of Engineering Manufacture* 227:407-416. doi: 10.1177/0954405412472673.

Sillapasa, K., Y. Mutoh, Y. Miyashita, and N. Seo. 2017. "Fatigue Strength Estimation Based on Local Mechanical Properties for Aluminum Alloy FSW Joints." *Materials* 10(2):186.

Sillapasa, K., S. Surapunt, Y. Miyashita, Y. Mutoh, and N. Seo. 2014. "Tensile and fatigue behavior of SZ, HAZ and BM in friction stir welded joint of rolled 6N01 aluminum alloy plate." *International Journal of Fatigue* 63:162-170. doi: https://doi.org/10.1016/j.ijfatigue.2014.01.021.

Silva-Magalhães, A., J. De Backer, J. Martin, and G. Bolmsjö. 2019. "In-situ temperature measurement in friction stir welding of thick section aluminium alloys." *Journal of Manufacturing Processes* 39:12-17. doi: https://doi.org/10.1016/j.jmapro.2019.02.001.

Smith, E.L. 2021. LDRD Project 79593 (AGILE) Project Management Plan Lite.

Struers. 2021. "Metallic Grain Structures and Microscopic Analysis." https://www.struers.com/en/Knowledge/Materials/Metallic-grain-structures.

Suenger, S., M. Kreissle, M. Kahnert, and M. Zaeh. 2014. "Influence of Process Temperature on Hardness of Friction Stir Welded High Strength Aluminum Alloys for Aerospace Applications." *Procedia CIRP* 24:120-124. doi: 10.1016/j.procir.2014.07.141.

Taheri, H., M. Kilpatrick, M. Norvalls, W.J. Harper, L.W. Koester, T. Bigelow, and L.J. Bond. 2019. "Investigation of Nondestructive Testing Methods for Friction Stir Welding." *Metals* 9(6):624.

Threadgill, P.L., A.J. Leonard, H.R. Shercliff, and P.J. Withers. 2009. Friction Stir Welding of Aluminum Aloys edited by TWI Global: TWI Global.

Tiamiyu, A.A., U. Eduok, J.A. Szpunar, and A.G. Odeshi. 2019. "Corrosion behavior of metastable AISI 321 austenitic stainless steel: Investigating the effect of grain size and prior plastic deformation on its degradation pattern in saline media." *Scientific Reports* 9(1):12116. doi: 10.1038/s41598-019-48594-3.

Toumpis, A., A. Galloway, H. Polezhayeva, and L. Molter. 2016. "Fatigue Assessment of Friction Stir Welded DH36 Steel." In *Friction Stir Welding and Processing VIII*, edited by Rajiv S. Mishra, Murray W. Mahoney, Yutaka Sato and Yuri Hovanski, 11-19. Cham: Springer International Publishing.

Uzun, F. and A. Nezihi Bilge. 2015. "Application of ultrasonic waves in measurement of hardness of welded carbon steels." *Defence Technology* 11(3):255-261. doi: https://doi.org/10.1016/j.dt.2015.05.002.

Uzun, F. and A. Nezihi Bilge. 2017. "A Comprehensive Model for Hardness Evaluation of Low-Alloy Steels Based on Carbon Content and Ultrasonic Wave Velocity." *Materials Evaluation* 75(12).

Whalen, S.A., K.S. Kappagantula, T. Rosendaal, M. Reeza-E-Rabby, X. Li, N.R. Overman, M.J. Olszta, T. Wang, D.R. Herling, S. Suffield, B.S. Taysom, J.E. Atehortua, J. Silverstein, N. Canfield, and D. Graff. 2021. *Shear Assisted Processing and Extrusion (ShAPE) of Aluminum Alloy 7075, 2024, and Al-12.4TM Final Technical Report*. PNNL-32387. Pacific Northwest National Laboratory, Richland, WA.

Whalen, S., V. Joshi, N. Overman, D. Caldwell, C. Lavender, and T. Skszek. 2017. "Scaled-Up Fabrication of Thin-Walled ZK60 Tubing Using Shear Assisted Processing and Extrusion (ShAPE)." In, *Magnesium technology 2017, pp.* 315-321. Springer International Publishing.

Wulff, A. 2013. "Friction Stir Welding Defects, Analysis and Correction: History and Defects of Solid-state Welding." South Dakota School of Mines and Technology.

Yamamoto, M., A. Gerlich, T.H. North, and K. Shinozaki. 2007. "Mechanism of cracking in AZ91 friction stir spot welds." *Science and Technology of Welding and Joining* 12:208-216.

Yuan, X., L. Chen, Y. Zhao, H. Di, and Z. Fuxian. 2014. "Dependence of grain size on mechanical properties and microstructures of high manganese austenitic steel." 11th International Conference on Technology of Plasticity, ICTP 2, Nagoya, Japan.

Pacific Northwest National Laboratory

902 Battelle Boulevard
P.O. Box 999
Richland, WA 99354
1-888-375-PNNL (7665)

www.pnnl.gov